UNIVERSITY OF SOUTHAMPTON

FACULTY OF PHYSICAL AND APPLIED SCIENCES

Optoelectronics Research Centre

Free-electron-driven nanoscale light sources: from Hertzian antennas to metamaterials

by

Giorgio Adamo

Thesis for the degree of Doctor of Philosophy

October 2011

UNIVERSITY OF SOUTHAMPTON

ABSTRACT

FACULTY OF PHYSICAL AND APPLIED SCIENCE

OPTOELECTRONICS RESEARCH CENTRE

Doctor of Philosophy

FREE-ELECTRON-DRIVEN NANOSCALE LIGHT SOURCES: FROM HERTZIAN ANTENNAS TO METAMATERIALS

by Giorgio Adamo

This thesis reports on the development of new types of nanoscale optical light sources driven by free-electrons and on the investigation of the underpinning physical phenomena. It is focused on three types of nanoscale light sources with increasing degree of complexity: a nanoscale antenna, an undulator-based tuneable nanoscale light source and a metamaterial-based spatially coherent light source.

I have demonstrated for the first time that a nanoscale Hertzian antenna can be driven by free-electrons. The studied nano-antennas consisting of pair of gold nano-rods spaced by a gap resemble conventional radio dipole antennas. Nanoantennas, driven by electron beam produce emission in the visible part of the spectrum. I show that these nanoantennas are most efficiently fed in the region of closest proximity between their two elements, in particular, where the light density of states reaches a maximum.

I have developed for the first time a tuneable nanoscale light source driven by free-electrons, the light-well. Alike a free-electron laser that exploits magnet-based undulators, the light-well is based on a nanoscale undulator, a cylindrical channel through alternating metal-dielectric nano-layers. A fast electron propagating through the channel emit light at the wavelength linked to the electron energy and the period of the undulator, thus allowing for a continuous tuning of the output radiation. It has been achieved a 200 nm tunability range in the vis-NIR range at wavelengths between 750 and 950 nm with light at the level of 200W/cm2. Furthermore, I have performed a comprehensive numerical analysis of the light-well by modeling a free electron propagating in the undulator which has lead to a deeper understanding of its physical mechanisms.

I demonstrate for the first time an electron-beam driven metamaterial light source that converts the kinetic energy of tree-electrons into spatially coherent optical radiation. It is based on a fundamentally new radiation phenomenon: the injection of free electrons into the metamaterial leads to a directed light emission that comes from synchronized plasmonic oscillations of the ensemble of metamolecules, the individual building blocks of the nanostructure. The effect results from the synchronizing interactions between the metamolecules leading to the spectrum narrowing with the increasing number of metamolecules involved. Depending on the type of metamaterial used I observed emission of narrow-divergent radiation in the visible range from 640 to 760 nm. These results - in principle - demonstrate an alternative to the laser, a threshold-free way of generating spatially coherent and spectrally narrow electromagnetic radiation.

Contents

List of Figures

DECLARATION OF AUTHORSHIP

I, Giorgio Adamo, declare that the thesis entitled "Free-electron-driven nanoscale light sources: from Hertzian antennas to metamaterials" and the work presented in the thesis are both my own, and have been generated by me as the result of my own original research. I confirm that:

- this work was done wholly or mainly while in candidature for a research degree at this University;
- where any part of this thesis has previously been submitted for a degree or any other qualification at this University or any other institution, this has been clearly stated;
- where I have consulted the published work of others, this is always clearly attributed;
- where I have quoted from the work of others, the source is always given. With the exception of such quotations, this thesis is entirely my own work;
- I have acknowledged all main sources of help;
- where the thesis is based on work done by myself jointly with others, I have made clear exactly what was done by others and what I have contributed myself;
- parts of this work have been published as the journal papers and conference contributions listed in Appendix C.

Signed: _____

Date: _____

Acknowledgements

I am very grateful to Prof. Nikolay Zheludev and Dr. Kevin MacDonald, my supervisors, for providing inspiration and guidance for successful research, while allowing me enough freedom to pursue my own ideas. I would like to thank Prof. Javier Garcia de Abajo for the tight collaboration, inputs and help with BEM software. I would like also to thank all the people that have helped with the experiments, Dr. Y. H. Fu, J. Y. Ou, Dr. J.K. So and particularly Dr. A. I. Denisyuk, who has coached me with the experimental setup during my first year, and Dr. N. Papasimakis, for the great help with Comsol software and simulations. I would also like to thank all my collaborators, Dr. F. De Angelis, Dr. S. D. Jenkins, Dr. J. Ruostekoski, Prof. E. Di Fabrizio, Dr. C.-M. Wang and Prof. D. P. Tsai. A thanks goes also to the other members of the group for the helpful discussion and the great time together. Finally I'm indebted to my family and Chiara for their continuous support and patience.

1 Introduction

1.1 Motivation

Photonics technologies are at the core of the broadband internet and modern mobile technologies. Over the years, optical systems have progressively replaced inefficient and bandwidth-limited electronic (i.e. copper wire) infrastructure but, to keep up with the ever-increasing demand for capacity, this trend will have to continue to the inter- and ultimately intra-chip level. Chip-scale light/plasmon sources will be fundamental to this nano-photonic revolution and have attracted considerable research interest around the world in recent years.

Various kinds of nanoscale light/plasmon sources have been demonstrated recently. For obvious reasons, the first structures to be 'transposed' to the nanoscale dimensions have been the simplest and most widely spread sources of electromagnetic radiation in the macro-world, antennas. Thanks to the recent advances in nano-fabrication capabilities, and the parallel explosions of the fields of Plasmonics and Metamaterials, a wide range of sources have been demonstrated or suggested, such as nano-cavity lasers, plasmon lasers, spaser and lasing spaser.

It is the aim of this work to demonstrate that the use of free electrons not only can be introduced to this rapidly evolving research-field but, most importantly, bring advantages that are peculiar to the nature of the free electrons thus opening the possibility of either accessing new regimes of operation for the nano devices or generating completely new phenomena.

This Chapter constitutes a short historical overview of aspects and technologies rel-

evant to the research presented in this thesis. Section 1.2 describes the rapidly evolving field of optical nano-antennas, the research fields where they might find applications, what has already been achieved and what is still left to do. In Section 1.3 the focus is moved towards other nanoscale types of light and plasmon sources, with special attention on nano lasers. Section 1.4 provides a glance on the recently born research field of metamaterials, how metamaterials have impacted on optics and photonics and what role they might play in the development of light sources. Section 1.5 looks instead at how electrons have been employed for the realization of light sources, what benefits they bring and how they have been used so far with the view of nanoscale light sources. Section 1.6 finally gives an overview of the structure of the thesis.

1.2 Nano-antennas

Antennas are the predominant mean for the manipulation of electromagnetic fields in radio- and microwave technology; the manipulation of optical signals happens instead through lenses, mirrors, fibres etc: the presence of antennas in optical modern technology is basically null. The main reason behind the lack of optical counterpart for antennas is to be found in the small scale they need to be fabricated. The situation has been changing in the last few years during which, the emerging of nanoscience and nanotechnology, together with the research interest in nano-optics and plasmonics, has suggested optical antennas as a potential opportunity for novel optoelectronic devices and many photonic applications [1].

The goal of the design of optical antennas is analogous to that of classical ones: to optimise the energy transfer between a localised source or receiver and free-space radiation. However, whereas the invention of classical (radio) antennas was driven by communication needs, that of optical antennas has its roots in microscopy. It was 1928 when Edward Singe suggested to use a gold particle to localise light on the surface of a sample in the attempt to overcome the diffraction limit. Then, in 1985, John Wessel introduced the idea that a gold particle could be used as an antenna [2] and in 1989 Fischer and Pohl provided the first experimental demonstration, using a polystyrene particle coated with gold [3].

After that of Fischer and Pohl, numerous studies, both experimental and theoretical,

have been carried out targeting the whole visible-infrared electromagnetic spectrum and employing various antenna geometries, some of which are illustrated in Fig. 1.1. The surface plasmon resonances associated with the optical antennas make them particularly efficient at specific wavelengths, a promising aspect for biological and chemical sensing and detection. The suggested applications for optical antennas span however a much broader range: photodetection [4] due to the fact that an optical antenna increases the absorption cross section and hence the light flux that impinges onto the detector; photovoltaics [5] where the main emphasis is on reducing layer thickness while keeping the optical absorption constant; nanoimaging [6] where the strong field localization can help reducing the imaging resolution, and nonlinear signal conversion [7] where the strong field enhancement provided by the antennas can be a route to use the strong metal third-order nonlinearities, just to cite some.

Despite the large number of studies performed on optical antennas and the important achievements obtained, still many challenges lay ahead before this can become a viable and widely spread technology and can fully match its radiofrequency counterpart. Two of the most significant steps undertaken along this direction have definitely been the achievement of directional emission of antennas driven by emitting molecules [8] and, more recently, the demonstration of conversion of free space light into surface plasmons onto the antenna and, in turn into 'hot-electrons', meaning electrical current [9]. What these demonstration lack so far is the local excitation of the antenna feeding point (the antenna is fully illuminated with laser light); this thesis's contribution to this field of research (see Chapter 3) is the demonstration of enhanced emission from an optical Hertzian-antenna when *locally* fed with a beam of free electrons [10].

1.3 Nanoscale light and plasmon sources

In the previous section it was mentioned that optical fields are manipulated using devices that are peculiar to this wavelength regime. This, obviously, applies also to the sources of electromagnetic radiation. The most widespread optical sources are lasers and light emitting diodes. Since its first demonstration in 1960, many kinds of lasers have been introduced, using various geometries, configurations and materials and a trend has been clear all along: scientists have been looking for ways of making lasers

smaller and more convenient to use. Indeed the range of lasers available today goes from table-top lasers to small semiconductor laser diodes present in many of current electronic devices.

One question hence follows from what just said and is indeed of paramount interest for the future development of photonic technologies and small scale, fully integrated photonic circuits in particular: how small can a laser be? For many years the size of a laser has been thought to be limited by the need of fitting an optical mode inside a cavity. This implies that diffraction enters into play therefore limiting the size of the laser cavity to about half of the wavelength of the emitted light. Indeed, many interesting micro-lasers have been demonstrated in the past few years (see Fig. 1.2) using numerous approaches such as nanowires [11] which can be optically and electrically pumped and, thanks to their cylindrical geometry, offer strong two-dimensional confinement of electrons, holes and photons; metal/semiconductor nanocavities [12, 13] which allow high modal compression, and photonic crystals [14], in whose nanocavities a dramatic increase of the modulation speed can be achieved through enhancement of the Purcell effect. All of them emit at wavelengths very close to the diffraction limit but do not surpass it.

This has been the case until 2009, when two realizations of lasers with mode size far beyond the diffraction limit have been demonstrated [15,16]. While the two approaches were very different from each other, a plasmonic waveguide in one case and core-shell nanoparticles in the other, they both made use of surface plasmons and their ability to achieve very high modal compression, to reach their goal.

Due to their properties (shorter wavelength than corresponding free space waves, high mode compressibility, etc,) and promises (e.g. bridging the gap between electronics and photonics), surface plasmons in nanoscale devices have been subject of large research effort in the last ten years. A number of investigations ranging from surface plasmon polaritons (SPPs) propagation in waveguides [18, 19], plasmon localization on extremely subwavelength spots [20] and surface plasmon modulation by external fields [21, 22] to, more recently, concurrence of SPPs high mode compression and long range propagation [23, 24] have been reported. More relevant to this thesis have been the demonstrations/proposals of micro/nanoscale sources of surface plasmon polaritons [25, 26] and the *spaser* [16, 27], a device that combines metals and gain material

and does for the surface plasmons what the laser does for the photons: it provides amplification of surface plasmons by stimulated emission in a coherent fashion.

It is straightforward to see that all these devices, nanoscale lasers, plasmon sources and spasers are of paramount importance for the field of nanophotonics for it to become a viable alternative/support to electronics to boost the current technology. Many steps are, however, still left as, e.g electrical pumping of lasers, coverage of a broad range of wavelengths etc; the work reported here (see Chapter 4) shows that free electrons can bring unique functionalities to these nanoscale devices, as e.g. broadband pumping (Section 2.2), tunability (Section 4.2) and highly localised excitation.

1.4 Metamaterials

The word metamaterial, which indicates artificial media with properties not found in the natural materials they are made of, was introduced not many years ago and indicates nowadays a rapidly evolving research field that embraces a vast range of artificial structures and electromagnetic properties. As a consequence, it is difficult to agree on a rigorous definition of metamaterials that is universally accepted. A definition that suits well many metamaterial structures, as the ones used in this thesis, is the following: metamaterials are periodic arrays of artificial structures arranged with a period smaller than the wavelength of excitation

The sub-wavelength periodicity makes metamaterials non diffracting media, hence they can be described in therms of effective parameters (dielectric permittivity ϵ and magnetic permeability μ) controlled by the geometry of the unit cell (usually referred to as meta-molecule) and the parameters of the constituent materials. The first structures that can be considered metamaterials, according to the definition given above, were arrays of metallic rods (two- and three-dimensional) behaving like dielectrics with an index of refraction less than unity [28] or plasmas [29] and, later, frequency selective surfaces, which can be regarded as planar metamaterials.

The field of metamaterials as known today however had its birth and explosion only in 1999, when John Pendry and co-workers suggested to use split ring resonators (already introduced by Hardy and Whitehead [30]) to realise artificial media with a - even negative - magnetic response from nonmagnetic conductors [31]. Only half a year

later David Smith and co-workers demonstrated a metamaterial made of a combination of split rings and wires having simultaneously negative permittivity (due to the wires) and negative permeability (due to the split rings) [32].

These works had a profound impact onto the research community because they implied that it was perhaps possible to engineer a medium with negative index of refraction, as predicted in 1968 in a theoretical paper by Veselago, where he argued that media with simultaneously negative permittivity and permeability would have a negative index of refraction [33]. A material exhibiting a frequency band where the effective index of refraction was negative was experimentally manufactured in 2001 [34] using concentric split ring resonators and wires (see Fig 1.4a). Another paper from Pendry in 2000 [35], where he concluded that a layer of material with refractive index of -1 would act as a perfect lens, not limited by diffraction and therefore able to focus to an arbitrarily small spot, increased the interest in metamaterials even further.

The main drive of metamaterial research has been for a while the possibility of realising a superlens, due to the huge potential it bears for imaging, lithography, data storage etc. After the experiments on negative refraction and superlensing in the microwave regime, the next step was to move towards the optical frequencies. In the optical spectral range the losses of metals, however, start playing a significant role so that a big effort has been spent in investigating different geometries (e.g. fishnet structures) and materials (e.g. dielectrics). An optical 'superlens' (see Fig 1.4b) was demonstrated, following the requirements (with the obvious experimental limitations), in 2005 [36].

While the initial effort was completely dedicated to demonstration of negative refractive index and superlensing, it was soon realised that metamaterials have much wider potential and applications. For example, the capability of controlling material parameters with high accuracy induced the emerging of transformation optics [37, 38], whose most known achievement is certainly the invisibility cloak (see Fig. 1.4c) [39, 40].

More recently it has also been realised that metamaterials, and in particular planar geometries, are ideal candidates for hybridization with conventional materials to enhance and extend the functionalities of the latter: good examples are the enhancement of nonlinearities of carbon nanotubes [41] or contrast enhancement in phase change materials [42, 43], just to cite some. Moreover, a large research effort has been spent

into combining gain media with metamaterials to either combat the inherent losses (from the metals) [44] or, with a view towards light sources based on metamaterials, enhance the luminescence of a medium [45, 46].

A very interesting meta-molecule geometry for planar metamaterials is the asymmetrically split ring (ASR), shown in Fig. 1.4d, which has high quality factor resonances [47]. Due to its ability of trapping the electromagnetic radiation on the metamaterial plane, the ASR has been the meta-molecule of choice in the work introducing the idea of a lasing spaser [48], a device which, by combining the spasing action with a slight symmetry breaking in the meta-molecule geometry, generates coherent laser radiation. Furthermore, it was shown that the ASR falls within a metamaterial family indicated as 'coherent', due to the nature of its narrowband resonances which come from a collective response of the meta-molecules rather than from the single meta-molecule [49]. The experiment demonstrated that this class of metamaterial show a spectral line collapse of their resonance when an increasing number of unit cell resonators is irradiated by a plane wave. The effect just described is crucial for achieving a lasing spaser.

It is by making use of the 'coherent' nature of the ASR that it was possible to demonstrate an intriguing new phenomenon, described in detail in Chapter 5: 'coherent' visible light has been generated, fuelled by coherent plasmonic oscillations in a large number of metamolecules, by exciting a planar metamaterial array in a single point through a beam of electrons

1.5 Free-electron light sources

The fact that free electrons can induce emission of radiation is known since many years: some of the phenomena leading to it and the reasons behind them are treated in Chapter 2, while here it is given only a very rapid outlook to some free-electron radiation sources available nowadays.

The most known free-electron radiation source today is, probably, the free-electron laser (FEL). The FEL is a light source where electromagnetic energy is extracted from the kinetic energy of a relativistic electron beam. The beam of electrons is propagated along the axis of an *undulator*, a 'tunnel' with a periodic lattice of alternating dipolar

magnetic fields. The beam is forced to undulate on the transverse plane, which causes the electrons to emit radiation.

The solely undulation of the electrons under the action of the magnetic field is however not enough to induce what is called the 'high-gain' regime of a FEL. In order to enter this regime, a density modulation of the electrons, called *bunching*, along the direction of propagation must take place. This phenomenon happens in a positive feedback fashion: the electrons emit radiation, which affects their position (phase) and thus causes them to emit with greater coherence. This effect is a collective (also called cooperative) process. In the high-gain regime, there is an exponential increase in the radiated power as the beam of electrons and radiation co-propagate along the FEL undulator, and an initially small signal, which may originally be simply noise, can be amplified by many orders of magnitude before the process saturates [50].

Since a FEL functions, following what said above, as a single-pass amplifier (no need for mirrors to form an oscillator cavity), the dimensions of a typical FEL are usually in the order of tens or hundreds of meters. In order to achieve more compact FEL, approaches making use of other radiation mechanisms (not magnetic fields) have been suggested. The most popular ones are probably Cherenkov [51–53] and Smith-Purcell FELs [54–56], which respectively engage the Cherenkov and Smith-Purcell emission: the former takes place when electrons travel in a medium with a velocity higher than the one of light in the same medium, while the latter happens when an beam of electrons travels parallel to a metal grating (a more detailed description of these two processes is given in Sections 2.3.3 and 2.3.4 respectively). Although significantly smaller in size than undulator based FELs, Cherenkov and Smith-Purcell FELs suggested or realised so far, are still (very) macroscopic devices and operate in mm-waves and THz regime.

Meanwhile, in the last ten years, an extremely precise spatial control on excitation of nanoscale structures by electron beams has been achieved; this allowed to perform investigations of the properties of nanoscale objects using the light they emit when free electrons interact with them [57, 58] (see Section 2.4.2 for some example). In all these studies however, the emission of light stimulated by free electrons was seen as a tool for the investigation of nano-object rather than the main goal. The work carried out for this thesis bears this shift in perspective: the precise control over the electron beam has been used to investigate the possibility of either feeding nanoscale light sources (as

in Chapter 3) or bringing new functionalities into them (Chapter 4) or investigating phenomena which could lead to new kind of light sources (Chapter 5).

1.6 Thesis Overview

Free electrons bring unique potential to the field of nanophotonics and this potential can be summarised in the following characteristics: true nanoscale localization and positioning, broadband transfer of energy (i.e. pumping), easy access to tunability. This thesis represents a first study of the potential exploitation of these characteristics for the pumping of various kind of nanoscale light sources by electron beams. The research carried out has led to intriguing results, as the **demonstration of nanoscale Hertzian optical antenna fed by free electrons** and the **demonstration of a tunable nanoscale light source driven by free electrons**, but also to the discovery of new phenomenon as the **emission of spatially coherent light from a metamaterial array locally excited by a beam of free electrons**.

Chapter 2 provides a theoretical analysis of the interactions between free electrons and matter and the most significant (for this thesis) mechanisms leading to emission of radiation. A description of free electrons as broadband source of radiation is given first and then it is shown, for each mechanism, how the energy transfer from the free electrons gives rise to light emission and the characteristic of the emitted light are discussed.

In Chapter 3 the emission of an antenna fed by free electrons is investigated experimentally. In particular it is carried out a comparison between the emission from a single branch (a nanorod) of an antenna and that of a coupled system (when two nanorods are placed in close proximity). It is experimentally shown how a coupled system, probed in the area of close proximity provides an enhanced emission at specific wavelengths; furthermore experimental results are supported by numerical simulations.

In Chapter 4 it is reported the demonstration of a tunable nanoscale light source driven by free electrons, built using materials compatible with current chip technologies (SiO_2 and Au). First, experimental evidence of light emission and tunability is pro-

vided, then the observed phenomenon is investigated using both analytical description and numerical simulations. The numerical investigation is also used to show that the same approach can be used to build light sources able to span the UV-IR spectral range.

Chapter 5 reports on the experimental investigation of planar photonic metamaterials as a template for novel light sources pumped by free electrons. Experimental results suggest that a new phenomenon takes place: local excitation of an array of meta-molecules leads to emission of spatially coherent light coming from collective response mediated by intra-meta-molecular interactions. The experimental results are supported by numerical analysis investigating the response of a metamaterial array when probed with localised excitation.

Finally, the work covered in this thesis is summarized in Chapter 6, together with an outlook of the potential routes of investigations for each of the three experimental demonstrations reported here.

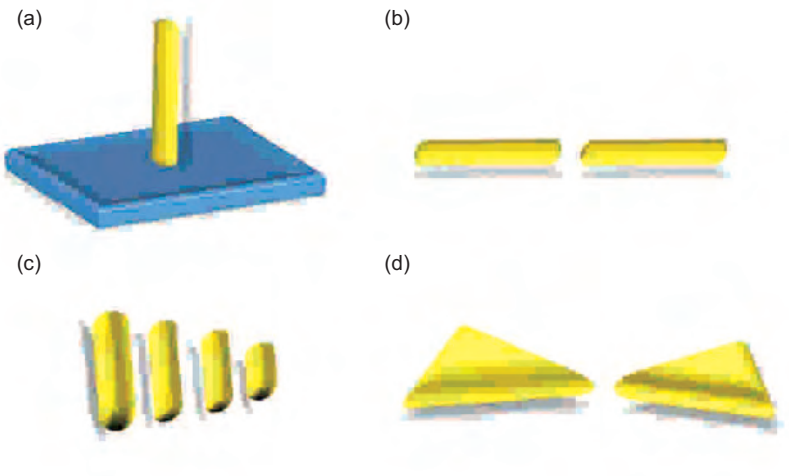

Figure 1.1: ***Most common types of nano-antennas.*** *(a) The ground dipole nano-antenna is extensively used as a probe, typically at the end of an optical fibre tip; (b) the dipole antenna is one of the most common structures used as optical antennas and, due to the field enhancement in the gap, a good choice for biology/sensing and plasmonic tweezers applications; (c) the Yagi-Uda configuration is the antenna of choice for the directivity it provides to the emitted light; (d) the bow-tie antenna is another example of dimer antennas and provides very high field enhancement within its gap.*

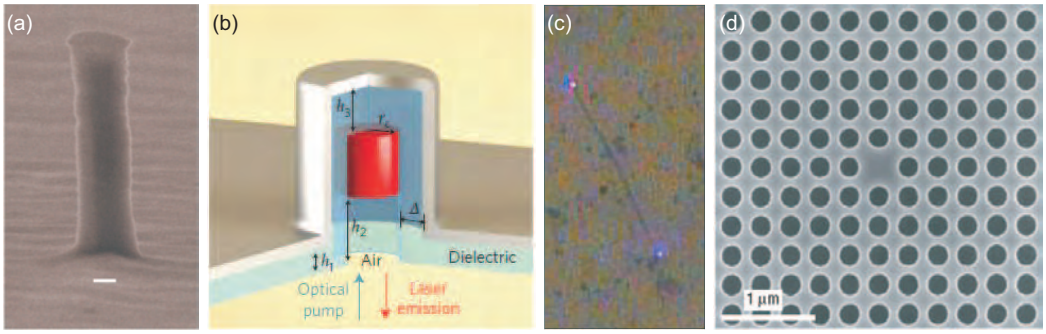

Figure 1.2: ***Examples of diffraction limited micro- and nano-lasers.*** *(a) First demonstration of a metallic-coated nanocavity laser with subwavelength cavity diameter and operation at cryogenic temperature [12]; (b) room temperature metallo-dielectric laser with subwavelength size in all three dimensions [13]; (c) gallium nitride nanowire laser [11]; (d) high speed photonic crystal laser [14].*

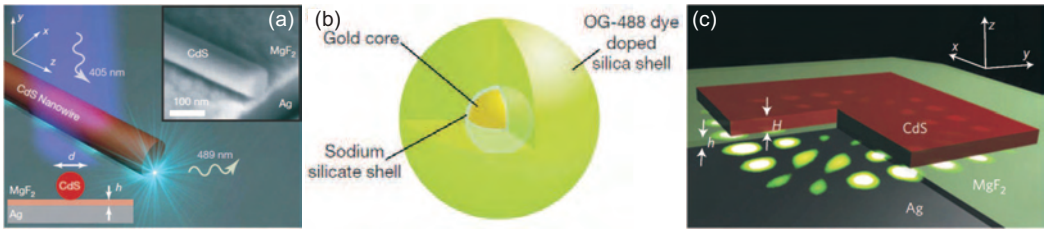

Figure 1.3: ***Lasers beyond the diffraction limit.*** *(a) First demonstration of plasmon laser [15] based on CdSe nanowire placed on top of a metal surface and separated by a few nm thick insulator layer; (b) first demonstration of a laser based on a core-shell nanoparticle cavity of 44 nm diameter [16]; (c) plasmon laser with lateral dimensions of 500 nm making use of total internal reflection to create a resonant cavity [17] .*

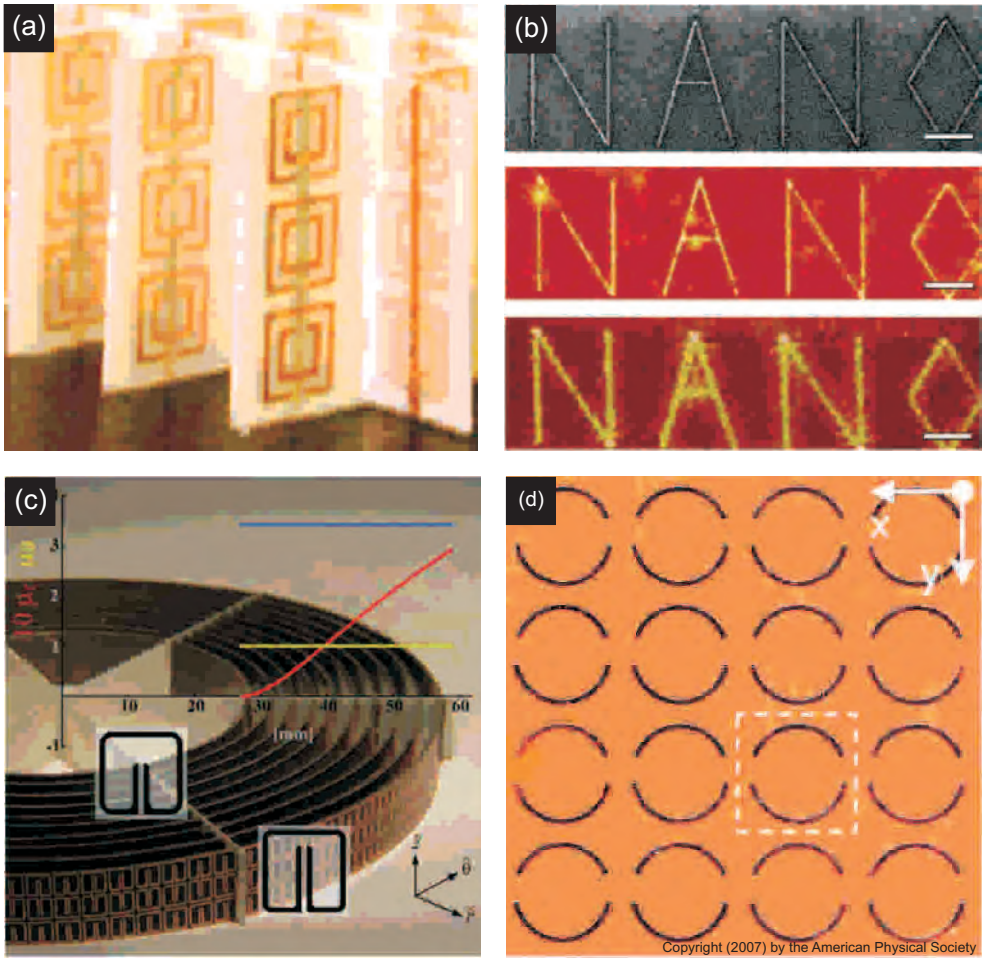

Figure 1.4: ***Metamaterials, some examples.*** *(a) First demonstration of negative index material made of concentric split rings resonators and wires; (b) experimental demonstration of superlensing; (c) first demonstration of a cloak in the microwave part of the spectrum; (d) asymmetric split ring geometry.*

2

Optical emission induced by free-electrons/matter interaction

In this chapter it is given an overview of the various mechanisms of light generation caused by the interaction between free electrons and matter. The mechanisms and effects that are of interest and relevance for the experimental results reported within this thesis are presented along with brief theoretical formulations of the interaction processes. Furthermore, a description of the experimental setup is provided. The last part of the chapter introduces the boundary elements method, a numerical method that has been chosen to model most of the experiments described in the next chapters.

2.1 Introduction

A swift electron can interact with a specimen either elastically or inelastically. Inelastic interactions (the only ones of interest here) involve exchange of energy between the two sides, free electron and specimen, and therefore produce effects on both of them. Except special cases, like Electron Energy Gain Spectroscopy, where a nanoparticle is optically pumped and transfers energy to an electron passing nearby [59], the energy transfer happens from the fast electron towards the specimen.

Free electrons have generally been used as nanoscale probes to investigates various properties of the specimens: topological structure, material composition, atomic structure etc. Lately the use of free electrons has been extended to the investigation of photonic properties of materials and micro/nano objects. These study have mainly retrieved photonic information about the samples through the investigation of either the energy lost by the fast electrons or the energy released by the process in the form of light.

The loss experienced by the electron can be quantified and used to retrieve information about the sample and the kind of interaction process that has taken place: the technique used to study this phenomenon is called Electron Energy Loss Spectroscopy (EELS).

The energy transferred to the specimen is released via various mechanisms, among which the most interesting are those giving rise to, electron emission (*Auger* and *secondary* electrons), cathodoluminescence (CL) light emission and, in the case of metals, bulk or surface plasmons (SP). Figure 2.1 shows a simple (and incomplete) schematic summarising the outcomes of the interaction between a beam of free electrons and a specimen.

With the view of nanoscale light sources driven by free electrons, surface plasmons generation and light emission are the processes of most interest in here and the mechanisms responsible for them the ones therefore treated in this chapter.

Cathodoluminescence Discovery of cathodoluminescence dates back to the mid-19th century as light emitted when electrons (cathode rays) hit the glass of evacuated discharge tubes; it has found wide application in the 20th century CRT television sets with

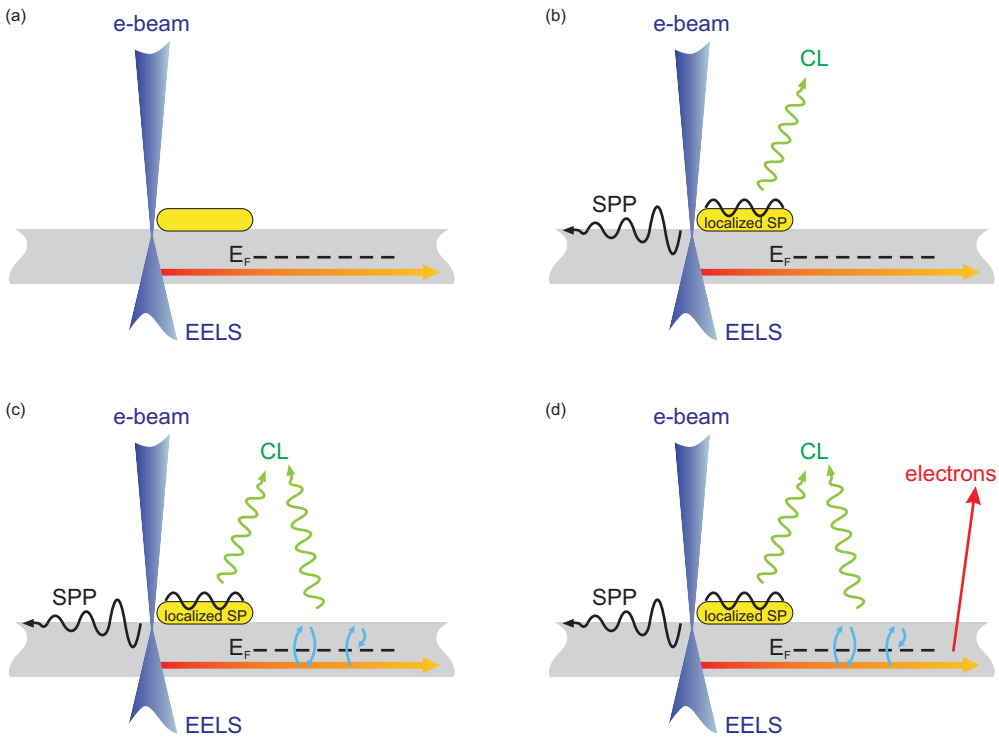

Figure 2.1: ***Some of the processes initiated by free-electron/matter interaction.*** *A beam of swift free electrons hits a thin sample triggering the following processes: (a) some of the electrons of the beam are diverted from the original path, as function of the energy they have lost in favour of the sample (orange arrow), and can be detected and analysed (EELS); (b) if the sample is a flat metal, the electrons can directly launch surface plasmon polaritons (SPPs) while, if the sample is a metal nanoparticle, localized plasmon will be generated on its surface; surface plasmons can be decoupled from the sample thus contributing to CL light emission; (c) the free electrons can also transfer energy to the bound electrons of the sample, which can radiatively decay either to the original energy level (coherent CL) or to an intermediate one (incoherent CL); (d) the energy transferred to the electrons of the sample can result in emission of electrons (Auger or secondary) from the sample. All these effects take place a the same time, as represented in (d)*

a recent renewed interest with the flat field emission and surface-conduction electron-emitter display technologies (FED and SED). Due to its material specific nature, CL is routinely used as a material characterization technique in diverse fields, as e.g. mineralogy and semiconductor physics.

The processes involved in CL emission can be divided into two classes: the processes for which the emission is *coherent* with respect to the evanescent field of the incoming electrons and those for which the emitted light is *incoherent* with respect to the field of the electrons. The main processes contributing to coherent radiation are transition radiation and Cherenkov radiation. The former arises when a moving charge

crosses the interface between two media with different dielectric constant, whereas the latter is emitted by charges that move through a medium with a higher speed than the one of the light in the same medium. Another process producing coherent radiation is the radiative recombination of electronic excited states (e.g. *e-h* pairs) that decay to the initial state and dominates CL in semiconductors. Carriers recombination is also a source of incoherent emission, when the decay does not happen towards the initial state but towards a different excited state. In metals, however, radiative carrier recombinations are slower channels than secondary electronic excitations, which are, consequently, the dominant decay channels (Auger electrons).

Plasmons The electromagnetic field associated to a free electron in motion is evanescent. This opens the possibility to access and excite electromagnetic oscillations with wave-vector components lying outside the light cone. For example, when an electron beam bombards a metal, the electrons of the beam couple to the free electrons of the metal inducing the latter to oscillate collectively. These oscillations are called plasmons because they are quasiparticles associated with oscillations of the electron gas *plasma* of the metal and they can involve both the bulk and the surface electrons of the metal and hence are known respectively as *bulk* and *surface* plasmons.

Surface plasmons can be found in two different configurations: they can be localised on the surfaces of subwavelength metal particles and they can as well exist and propagate on extended metal surfaces or 1D waveguides; in this last case they take the name of surface plasmons polaritons (SPPs). Localised surface plasmon, differently from SPPs, can undergo radiative decay and their contribution to light emission adds up to the the other mechanisms of light emission that undergo the name of cathodoluminescence; they constitute an indirect emission process but, nonetheless, coherent with the field of the swift electrons.

The first work suggesting the existence of both surface and bulk electron oscillations was carried out by Ritchie and dates back to 1957 [60]. Their existence was later confirmed by Powell and Swan in 1959 [61]. The first observations of light emission from SPPs produced by electron beams were instead made by Teng and Stern [62], while their propagation and scattering from metal has been recently reported with nanometer resolution [63, 64]. Yamamoto and collaborators first reported light emission due

to localised surface plasmon excitation by energetic electron beams in silver nanoparticles, along with spatially-resolved distribution of the plasmons on the surface of the particle [65].

Metals, thanks to their ability of supporting plasmons and currents, were the materials of choice in the experiments reported in this thesis. Therefore in this chapter the focus will be on those mechanism and processes that are most relevant in the light emission generated by interaction of free electrons with metals, in particular transition radiation, surface plasmons, Cherenkov radiation and the Smith-Purcell effect, with the latter that can be regarded as a special case of the Cherenkov. The description of these mechanisms will follow the ones reported in textbooks [66] and reviews on the topic [67].

The rest of the Chapter is hence structured as follows: Section 2.2 sets the mathematical platform that allows to describe free electrons as evanescent sources of light; Section 2.3 dwells into some mechanisms of electron induced emission of radiation, specifically Transition Radiation, Surface Plasmons and Cherenkov Smith-Purcell Radiations; Section 2.4 then considers the experimental set-up used to perform the experiments reported in this thesis and provides two examples to asses its capabilities; in Section 2.5 the Boundary Element Method, used to numerically describe many of the experimental results, is introduced and its mathematical description is provided; finally, since the thesis deals with experimental realisation of light sources, Section 2.6 deals with the definition of coherence of a light source.

2.2 Free electrons as evanescent source of light in matter

A point charge traveling at constant speed along a straight line in vacuum does not emit radiation. It however bears an electromagnetic field that can be considered as an evanescent source of radiation allowing to access regions of the frequency-momentum space that lie outside the light cone.

Consider an electron, of charge $-e$, travelling on a straight trajectory with constant velocity vector $\mathbf{v}$ along the z axis and crossing the origin at time $t = 0$. The electromagnetic fields $\mathbf{E}(\mathbf{r}, t)$ and $\mathbf{H}(\mathbf{r}, t)$ set by the electron in motion in the surrounding

space must satisfy Maxwell's equations:

$$\begin{aligned}\nabla \cdot \mathbf{B} &= 0,\\ \nabla \cdot \mathbf{D} &= \rho,\\ \nabla \times \mathbf{E} &= -\frac{\partial \mathbf{B}}{\partial t},\\ \nabla \times \mathbf{H} &= \mathbf{J} + \frac{\partial \mathbf{D}}{\partial t},\end{aligned}$$

where ρ and $\mathbf{J}$ are respectively the charge and the current density associated with the moving electron, that are expressed by:

$$\rho(\mathbf{r},t) = -e\delta(\mathbf{r} - \mathbf{v}t), \tag{2.1}$$

$$\mathbf{J}(\mathbf{r},t) = \mathbf{v}\rho(\mathbf{r},t). \tag{2.2}$$

A convenient way to find solutions to the fields distributions is to operate in frequency-momentum space. The Fourier transform connecting the two domains, $[\mathbf{r},t] \leftrightarrow [\mathbf{q},\omega]$, is given by:

$$\mathbf{F}(\mathbf{r},t) = \frac{1}{(2\pi)^2}\int d^3\mathbf{q}\int d\omega \mathbf{F}(\mathbf{q},\omega)e^{i\mathbf{q}\cdot\mathbf{r}-i\omega t}, \tag{2.3}$$

and when applied to the source distributions it returns:

$$\rho(\mathbf{q},\omega) = -\frac{e}{2\pi}\delta(\omega - \mathbf{q}\cdot\mathbf{v}), \tag{2.4}$$

$$\mathbf{J}(\mathbf{q},\omega) = \mathbf{v}\rho(\omega - \mathbf{q}\cdot\mathbf{v}). \tag{2.5}$$

The above conditions applied to Maxwell's equations, give the following solution for the fields in the real space:

$$\mathbf{E}(\mathbf{r},\omega) = \frac{2ie}{(2\pi)^{3/2}} \int d^3\mathbf{q} \frac{\mathbf{q}/\epsilon - k\mathbf{v}c}{q^2 - k^2\epsilon} e^{i\mathbf{q}\cdot\mathbf{r}} \delta(\omega - \mathbf{q}\cdot\mathbf{v}). \tag{2.6}$$

The dependence of the fields on the distance from electron trajectory and on electron velocity can be more easily understood if, of the above equation, it is given the explicit solution, showing the contribution of the individual components of the field. An electron travelling along the z axis, as the one considered here, is described by electric field both on axis (along the direction of propagation) and radial direction, and an azimuthal magnetic field. They can be analytically expressed as:

$$\mathbf{E}(\mathbf{r},\omega) = -\frac{e\omega}{v^2\gamma_\epsilon\epsilon} \left(\frac{2}{\pi}\right)^{1/2} e^{i\omega z/v} \left[\frac{i}{\gamma_\epsilon} K_0\left(\frac{\omega R}{v\gamma_\epsilon}\right)\hat{\mathbf{z}} - K_1\left(\frac{\omega R}{v\gamma_\epsilon}\right)\hat{\mathbf{R}}\right], \tag{2.7}$$

$$\mathbf{H}(\mathbf{r},\omega) = -\frac{e\omega}{v^2\gamma_\epsilon\epsilon} \left(\frac{2}{\pi}\right)^{1/2} e^{i\omega z/v} K_1\left(\frac{\omega R}{v\gamma_\epsilon}\right)\hat{\boldsymbol{\varphi}}, \tag{2.8}$$

where, R is the distance from the electron's trajectory, $\hat{z}, \hat{R}$ and $\hat{\varphi}$ are respectively the axial, radial and azimuthal unit vector components, $\gamma_\epsilon = 1/\sqrt{1 - \epsilon v^2/c^2}$ is the Lorentz contraction factor and K_0 and K_1 are the modified Bessel functions of the second kind. Two interesting features stem out from the expressions of the fields reported in 2.7 and 2.8: first, they refer to each monochromatic component of the electromagnetic field, and second, the fields decay away from the electron trajectory, inversely proportionally with respect to the electron velocity v (see Fig. 2.2).

The just highlighted features suggest that an electron moving with a constant velocity on a straight path can be regarded as *a broadband, evanescent source of light moving with velocity v along the electron trajectory.* An interesting fact is that the external field of the electron diverges at the position of the trajectory, resulting in a theoretically infinite resolution. The actual resolution of the experiments is however not such: it is limited by the finite size of the beam spot and the delocalized character of the material response [68]. An upper limit to the resolution is set by the exponential decay (K_1) of the fields with the distance.

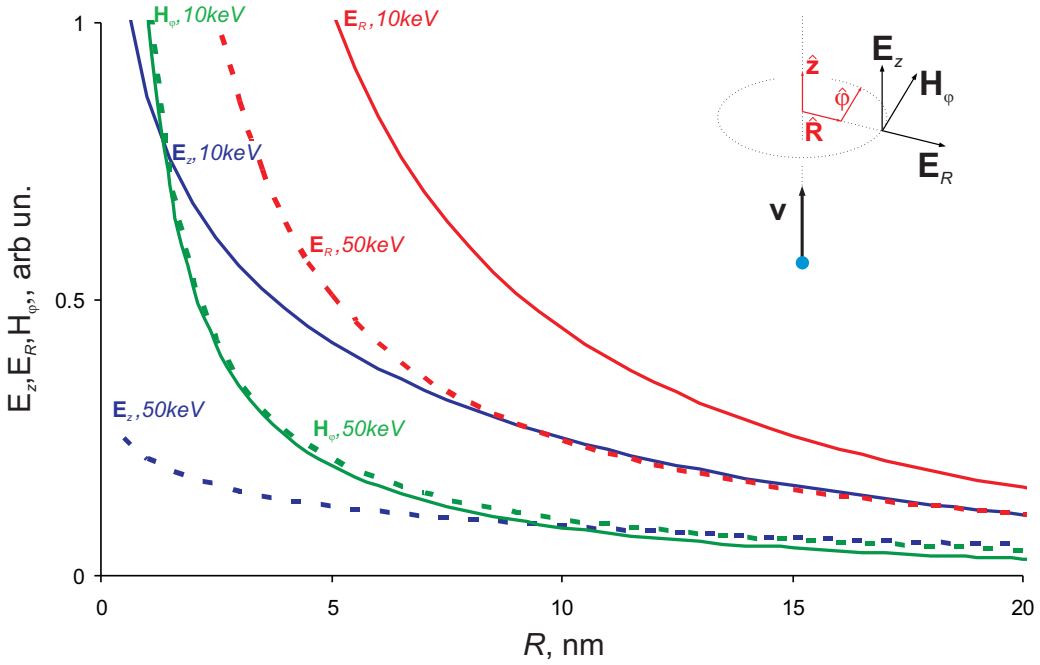

Figure 2.2: ***Evanescent nature of the fields of swift free electrons.*** *Behaviour of each component of the field associated to a free electron travelling at constant velocity, as function of the distance from the electron trajectory, R for a wavelength of* 600 *nm. The inverse proportionality dependence on the electron velocity v is exemplified showing the behaviour of the field components for two different energies,* 10 *and* 50 *keV, of the free electron.*

2.3 Mechanisms of light emission

As introduced in Section 2.1, various mechanisms are responsible for the emission of radiation following the interaction of free electrons with a specimen. In this Section the most relevant ones for the work reported in this thesis are analyzed using the same mathematical formalism adopted for the description of the fields associated with an electron moving with constant velocity (Sec. 2.2)

2.3.1 Transition radiation

Transition radiation (TR) was first predicted by Ginzburg and Frank in 1946 [69] and observed experimentally only in 1959 in the visible range by Goldsmith and Jelley [70]. The physical mechanism behind it is fairly simple (see Fig. 2.3): when an electron, moving inside a first medium, is incident on the surface of a second medium, it creates a perturbation in the electrons of the latter thus inducing a polarization charge. The incoming electron and the induced charge act as an induced dipole. When the electron

physically crosses the interface, the sudden cancellation of the dipole produces radiation that can decay into two channels: direct emission in the far field (TR) and, in the case of a metal, generation of surface plasmons (which will be discussed in the next section).

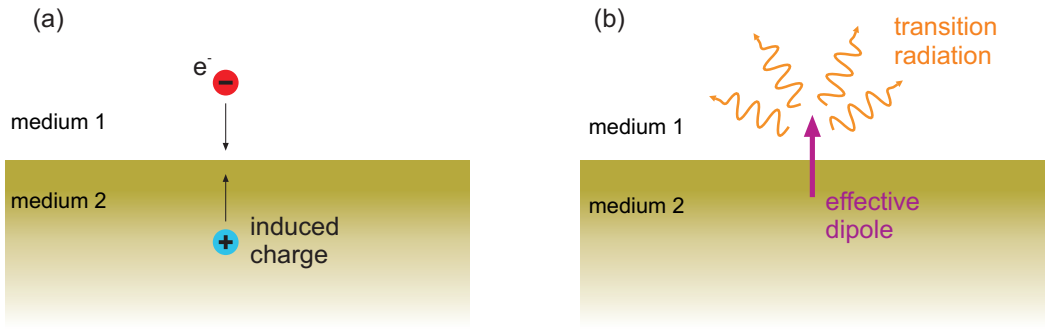

Figure 2.3: ***Mechanism responsible for the transition radiation.*** *(a) A free electron travelling from medium 1 towards the interface between the two media creates an induced charge in the electrons of medium 2; (b) once the free electron crosses the interface, the annihilation of the effective dipole made by the two charges generates emission in the far field, which goes under the name of transition radiation (TR) .*

Let's consider, again, a free electron traveling with constant velocity $\mathbf{v}$ along the z axis towards an interface between two media (at $z = 0$). The electric field set by the swift electron in each medium j (with $j = 1, 2$ indicating the medium above and below the interface respectively) in the proximity of the interface is given by the sum of two components, the field induced by the electron in an infinite bulk medium plus the field reflected at the interface:

$$\mathbf{E} = \mathbf{E}_j^{bulk} + \mathbf{E}_j^{ref},$$

the latter being the field generated by the induced surface charges and currents.

The *bulk* component of the field is obtained directly from Eq. 2.6 through integration of the z component of $\mathbf{q}$=$(\mathbf{q}_{||}, \omega/v)$. These fields evanescently decay away from the electron trajectory, hence they do not contribute to TR emission (they however are responsible for Cherenkov radiation under the appropriate conditions, as discussed in 2.3.3).

The *reflected* (or *induced*) component of the fields can be solved for the induced polarization charges by applying the boundary conditions at the interface $z = 0$ (con-

tinuity of the parallel components of the electric and magnetic fields). The expression of the reflected magnetic field, after some algebraic manipulation, reduces to:

$$\mathbf{H}_j^{ref}(\mathbf{q}_{||}, z, \omega) = -2\pi e^{iq_{zj}|z|} D\mu_j \,\mathrm{sgn}(z)\hat{\varphi}_{\mathbf{q}}, \tag{2.9}$$

where $q_{zj} = \sqrt{k^2\epsilon_j - q_{||}^2}$, $\hat{\varphi}_{\mathbf{q}} = \hat{\mathbf{z}} \times \hat{\mathbf{q}}_{||}$, the coefficients μ_j are determined by applying the boundary conditions and can be written as:

$$\mu_1 = \frac{1}{|v|}\left(\frac{\omega\epsilon_2 + vq_{z2}\epsilon_1}{q^2 - k^2\epsilon_1} - \frac{\omega\epsilon_1 + vq_{z2}\epsilon_1}{q^2 - k^2\epsilon_2}\right), \tag{2.10}$$

$$\mu_2 = \frac{-1}{|v|}\left(\frac{\omega\epsilon_2 - vq_{z1}\epsilon_2}{q^2 - k^2\epsilon_1} - \frac{\omega\epsilon_1 + vq_{z1}\epsilon_2}{q^2 - k^2\epsilon_2}\right), \tag{2.11}$$

and D is given by:

$$D = \frac{2ieq_{||}/c}{q_{z1}\epsilon_2 + q_{z2}\epsilon_1}. \tag{2.12}$$

Given the geometry of the problem treated here, the fields are obviously azimuthally symmetric; the induced field can then be obtained by inserting Eq. 2.9 into Eq. 2.6 (for the corresponding magnetic field) and solving the integral over the azimuthal angle of $\mathbf{q}_{||}$, which gives:

$$\mathbf{H}_j^{ref}(\mathbf{r}, \omega) = -i \;\mathrm{sgn}\, z\hat{\boldsymbol{\varphi}} \int_0^\infty q_{||} dq_{||} D\mu_j e^{iq_{zj}|z|} J_1(q_{||}R), \tag{2.13}$$

where R and $\hat{\boldsymbol{\varphi}}$ are, respectively, the distance from the electron trajectory and the azimuthal unit vector (as previously indicated for Eq. 2.8), and J_1 is the first order Bessel function of the first kind.

In all the experiments reported in the following, the CL signal is detected in the far field. This allows two considerations: *i)* since the fields directly produced by the moving electrons (indicated in this section as *bulk*) are evanescently decaying, the only TR signal of interest is the one associated with the *induced* field, *ii)* as $kr \to \infty$ in

medium 1, H^{ref} behaves as $\mathbf{H}_j^{ref}(\mathbf{r},\omega) \to \mathbf{f}_H(\theta,\omega)e^{ikr}/r$. Performing this asymptotic analysis on Eq. 2.13, one gets

$$\mathbf{f}(\mathbf{r},\omega) = ik\cos(\theta)D\mu_j\hat{\varphi},$$

where θ is the emission angle with respect to the surface normal (zenith angle). This expression must be evaluated at $q_{||} = k\sin\theta$, where θ is the emission angle with respect the surface normal. The intensity of the emitted light is linked to the emission probability as function of the frequency, $\Gamma(\omega)$, through $I = \int_0^\infty d\omega\Gamma(\omega)$ and is proportional to the integral of the Poynting vector over the emission directions (in this case the upper hemisphere in the vacuum). This leads to the following expression for the probability of emission for the transition radiation

$$\Gamma_{TR}(\omega) = \frac{1}{2\pi\hbar k}\int_0^{\pi/2}\sin\theta d\theta|\mathbf{f}(\theta,\omega)|^2, \tag{2.14}$$

where the probability is expressed per incident electron and per unit of photon frequency range. Eq. 2.14 will be used in the analytical and numerical modelling of the experiments, when evaluating the contribution of TR in the CL signal, and its behaviour, in the case of a 30keV free electron impinging onto a flat gold surface, is reported in Fig. 2.4.

2.3.2 Surface plasmons

When a swift electron hits the surface of a flat metal sample it generates, along with TR, surface plasmons polaritons (SPPs), as illustrated in Fig. 2.5a. The condition on the wave vector that describes the generation of plasmons can be identified as the pole of D in Eq. 2.9, which corresponds to the surface plasmon dispersion relation:

$$q_{z1}\epsilon_2 + q_{z2}\epsilon_1 = 0, \tag{2.15}$$

which is equivalent to the more known form for the SPPs dispersion

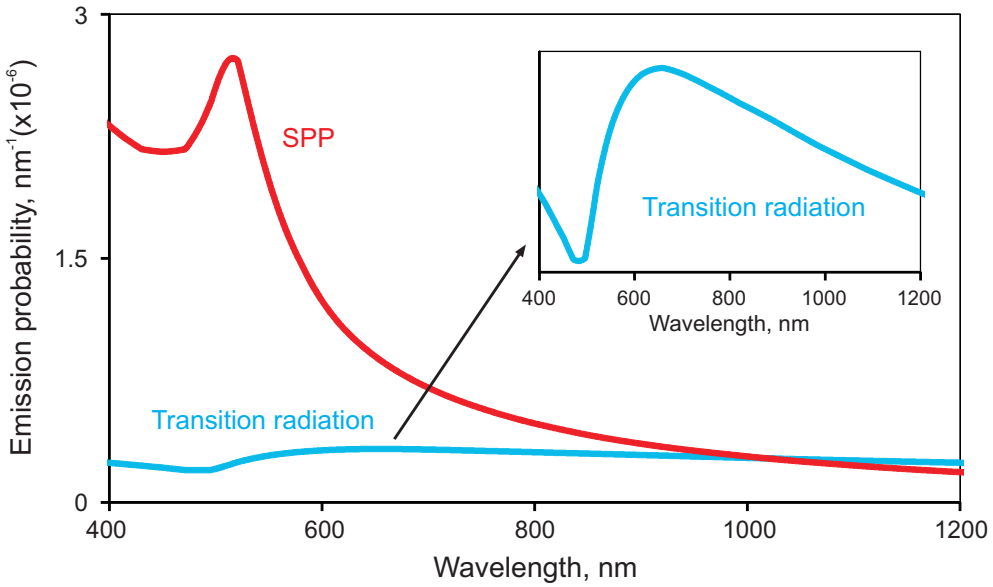

Figure 2.4: ***Probability of generating TR and SP by electron impact on metal.*** *Emission probabilities of transition radiation (blue) and surface plasmons (red) by a 30keV free electron of a gold surface, calculated according to Eq. 2.14 and Eq 2.19 respectively. [inset: zoom onto the transition radiation spectra to better highlight its behaviour] .*

$$q_{||}^{SP} = k\sqrt{\frac{\epsilon_1\epsilon_2}{\epsilon_1+\epsilon_2}}, \tag{2.16}$$

graphically illustrated in Fig 2.5b, where $k = \omega/c$.

By performing a Taylor expansion of $q_{z1}\epsilon_2 + q_{z2}\epsilon_1$ around the pole $q_{||} = q_{||}^{SP}$ [71], it is possible to express

$$D \approx \frac{C}{\mathbf{q}_{||} - \mathbf{q}_{||}^{SP}}, \tag{2.17}$$

where

$$C = \frac{2ieq_{z1}^{SP}}{c}\frac{\epsilon_2}{\epsilon_1^2 - \epsilon_2^2}$$

which allows, after inserting these expression into Eq. 2.9 and integrating over $q_{||}$ (using the $q_{||} = q_{||}^{SP}$ pole), to get the following expression for the field

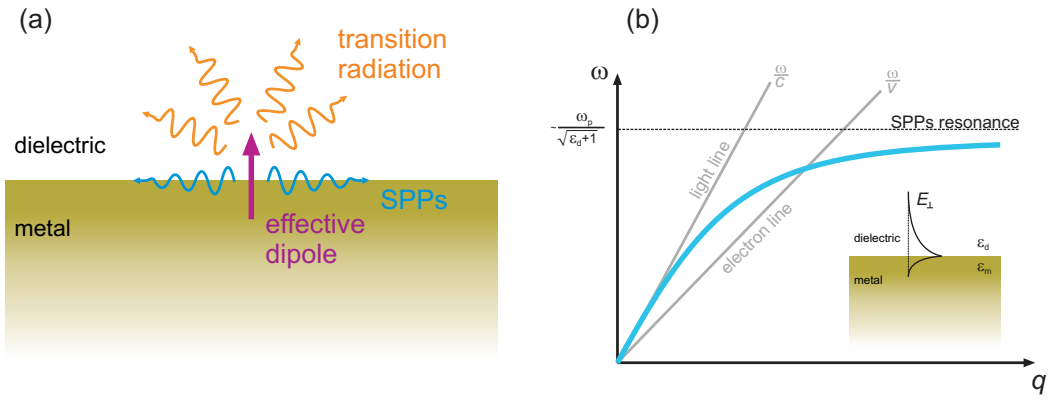

Figure 2.5: ***SPPs generation from electron impact on metal.*** *(a) A fast free electron crossing a boundary, where the medium 2 is a metal, generates surface plasmon polaritons (SPPs) along with transition radiation; (b) SPPs dispersion line lies on the right of the light cone thus not allowing direct plasmon generation by light without a matching mechanism (e.g. a grating); with a free electron, on the contrary, the area on the right of the light line can be easily accessed [inset: schematic illustration of the evanescent nature of the surface plasmons, showing the exponential decay of their electric field away from the interface where they exist and are bound] .*

$$\mathbf{H}^{ref}(\mathbf{r},\omega) \approx \pi q_{||}^{SP}\,\mathrm{sgn}(z) C \mu_j e^{iq_{zj}^{SP}|z|} H_1^{(1)}(q_{||}^{SP}R)\hat{\varphi}, \tag{2.18}$$

where μ_j is the parameter defined in equations. 2.10 and 2.11, $q_{zj}^{SP} = \sqrt{k^2\epsilon_j - (q_{||}^{SP})^2}$ and $H_1^{(1)}$ is a Hankel function decaying as $\sim (R)^{1/2}$ at large distance from the electron trajectory. As in the previous case (TR) what is interesting here is to know what is the probability of emission for SPs. This can be obtained by performing the integral of the Poynting vector for the fields described by Eq. 2.18 over a cylindrical surface centered around the electron trajectory, and gives

$$\Gamma_{SP}(\omega) = \frac{1}{2\pi^2\hbar k^2}\sum_{j=1,2}\frac{|\pi q_{||}^{SP}\,\mathrm{sgn}(z) C\mu_j|^2}{Im\{q_{zj}^{SP}\}} Re\left\{\frac{q_{||}^{SP}}{|q_{||}^{SP}|\epsilon_j}\right\}, \tag{2.19}$$

where the probability is expressed per incident electron and per unit of plasmon frequency range. The generation rate of SPs as function of free-space wavelength of emission, calculated according to Eq. 2.19, is shown in Fig. 2.4.

Localized surface plasmons On metal-dielectric interfaces of arbitrary geometry oscillations of the charge density, similarly to the SPPs case, can also be supported. In

this case they take the name of *localized* surface plasmons and some difference arises with respect to the case of propagating plasmons. In the case of simple geometries as, for example, spheres and disregarding retardation effects (good approximation in the case of particles of small size with respect the wavelength of interest) an analytical description of the localised plasmons is possible and can help to highlight the differences.

In the case of a sphere, the *nonretarded* ($q_{z1} = q_{z2} = q$ with $q \gg \omega/c$) planar surface-plasmon condition, $\epsilon_1 + \epsilon_2 = 0$ is replaced by

$$l\epsilon_1 + (l+1)\epsilon_2 = 0, \qquad l = 1, 2, ..., \tag{2.20}$$

where l is the orbital momentum number and accounts for multipolar plasmons resonances. If a Drude model for the metal is applied to both case, the following surface plasmon wavelengths are obtained

$$\omega_s = \frac{\omega_p}{\sqrt{2}} \tag{2.21}$$

$$\omega_l = \omega_p \sqrt{\frac{l}{l+1}} \tag{2.22}$$

for propagating (ω_s) and localized (ω_l) surface plasmons, respectively. When excited by an electron beam, the plasmons generated on the surface of a metal nanoparticle will contribute to the CL emission through their di- or multi-polar oscillations at the wavelengths dictated by Eq. 2.22. In the case of arbitrarily complex geometries numerical methods, such as the boundary element method (BEM) described in Section 2.5, have to be used to evaluate the localized surface plasmon wavelength and distribution.

2.3.3 Cherenkov radiation

In section 2.2 it was stated that, except in special cases, an electron travelling on a straight trajectory at constant velocity, sets an electromagnetic field in the surrounding space, but does not emit radiation. Cherenkov radiation (CR) is, probably, the most known case in which the field generated by the free electron becomes oscillatory in the far field, thus producing electromagnetic radiation. This kind of light emission was first

observed by Cherenkov in 1934 [72] and found a successful explanation by Frank and Tamm in 1937 [73, 74]. The conditions under which such phenomenon occurs can be retrieved by reconsidering Eq. 2.7.

If a charged particle travels in a medium with constant velocity v greater than the one of light in the same medium, expressed by the condition

$$v > c/\sqrt{\epsilon}, \tag{2.23}$$

the argument of the Bessel functions in Eq. 2.7 becomes imaginary, thus inducing an oscillatory behaviour of the fields in the far field region. This indicates that energy is dragged away from the electron, hence inducing light emission.

The probability of CR emission per frequency of radiation is given by the following expression:

$$\Gamma_{CR}(\omega) = \frac{e^2 L}{\hbar}\left(\frac{1}{c^2} - \frac{1}{v^2\epsilon}\right), \tag{2.24}$$

where L is the length of the trajectory and ϵ is the frequency dependent permittivity of the homogeneous medium.

A characteristic feature of Cherenkov radiation is its non-uniform distribution in frequency, being rather characterised by emission in frequency bands nearby regions of anomalous dispersion, as schematically illustrated in Fig. 2.6a, and where $\epsilon > 1/\beta^2$, with $\beta = v/c$ (condition coming from $\Gamma_{CR} > 0$ and equivalent to the one set in Eq. 2.23). Another typical feature of CR is its angle of emission, which can be expressed as

$$\cos\theta_{CR} = \frac{1}{v/c\sqrt{\epsilon}} \tag{2.25}$$

thus being dependent on both the velocity of the electron v and the frequency ω, through ϵ. For this reasons Cherenkov radiation detector are widely employed in high energy physics, for example as mass analyzers and for velocity measurements. The angle θ can be retrieved from considerations on the electron field components

($\tan\theta_{CR} = -E_z/E_R$) but can also interpreted qualitatively using the analogy with shock wavefronts (see Fig. 2.6b).

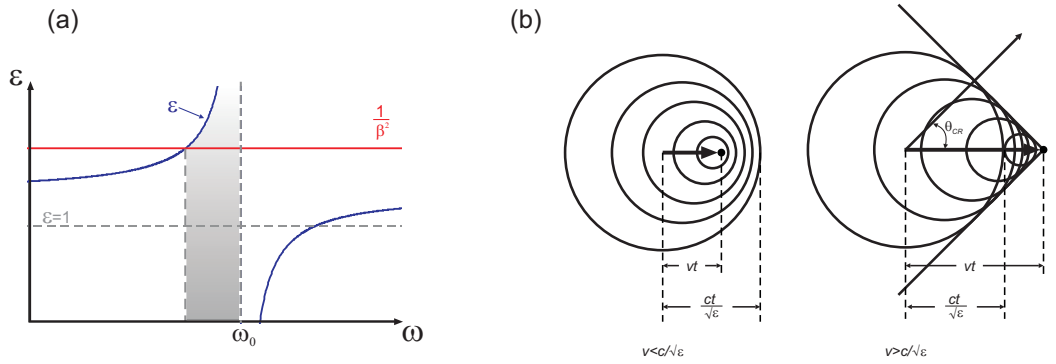

Figure 2.6: ***Cherenkov radiation emission condition.*** *(a) Graphical representation of the condition to have CR, $\epsilon > 1/\beta^2$; the shaded area indicates the frequency band, below the region of anomalous dispersion, where CR takes place; (b) CR analog of shock waves: when the electrons travel with velocity $v < c/\sqrt{\epsilon}$ no emission takes place, when instead the velocity increases to the level $v > c/\sqrt{\epsilon}$, CR is emitted with a wavefront given by the envelope of the wavefronts at specific positions. The angle θ_{CR} is equal to the angle formed by the direction of motion of the electron with the direction of propagation of the generated wave.*

The classical Cherenkov radiation is not of particular interest for the experiments reported in this thesis since the electrons employed in the experiment have energies not sufficient to trigger the conditions stated above. Another kind of light emission mechanism, connected to the Cherenkov one, is however relevant to some of the experimental observations reported here: the Smith-Purcell emission.

2.3.4 Smith-Purcell effect

The Smith-Purcell effect was discovered by Smith and Purcell in 1953 [75], when they recorded light emission from a beam of free electrons travelling with constant velocity, v, above a metal grating (parallel to it, without contact). The Smith-Purcell radiation is continuously emitted in a wide wavelength range, over a wide angular section covering the half hemisphere above the grating. Wavelength and direction of emission are determined by various parameters and follow a very simple relation,

$$\lambda = L(c/v - \cos\theta) \tag{2.26}$$

where λ is the wavelength of emission, L is the period of the grating and θ the angle of emission. Eq. 2.26 comes from the condition of constructive interference of aligned emitting sources, as schematically illustrated in Fig. 2.7

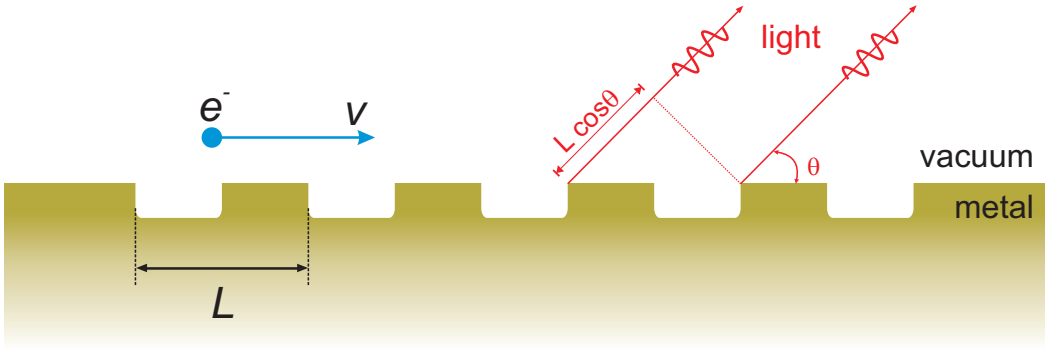

Figure 2.7: ***Smith-Purcell emission spectrum.*** *The grating/electron system can be interpreted as an array of emitters periodically spaced at distance L from each other and successively excited by the travelling electron. In this case, they will constructively emit when the path difference between the period L (distance travelled by the electron at a speed v in a time Δt) and the space ($L\cos\theta$) covered by the light during the same time interval, $c\Delta t$ is a multiple of the wavelength λ. The emitted light will then be a continuous of wavelengths each corresponding to a specific direction, θ.*

Theoretical analyses of the effect have been produced that either describe it as arising from the diffraction on the grating of the evanescent waves associated with the moving electron [76, 77], or considering the currents induced on the surface of the grating by the electron [78]. The Smith-Purcell emission, along with other effects, can be regarded as a *cherenkovian* effect, since it can be obtained as a generalization of the Cherenkov effect. An analytical proof can be found in [76], while here it is given an intuitive picture of the reason. In Fig. 2.8a and b are shown the dispersion diagrams for, respectively, the 'classical' Cherenkov radiation and Smith-Purcell emission.

The case of CR is illustrated by Fig. 2.8a, where it is shown the dispersion relation of light moving in medium of dielectric constant ϵ along with the line indicating the dispersion of a wave associated with an electron moving with velocity v, ω/v. Just below the region of anomalous dispersion of the medium, at $\omega = \omega_0$ the velocity of the electron exceeds the one of the light in the medium, $v > c/\sqrt{\epsilon}$ (corresponding exactly to the condition, derived from Eq. 2.24, $\epsilon > 1/\beta^2$), as highlighted in the inset of the figure. The shaded region corresponds to CR emission, matching the one previously illustrated in Fig. 2.6a. The Smith-Purcell emission condition is instead schematically

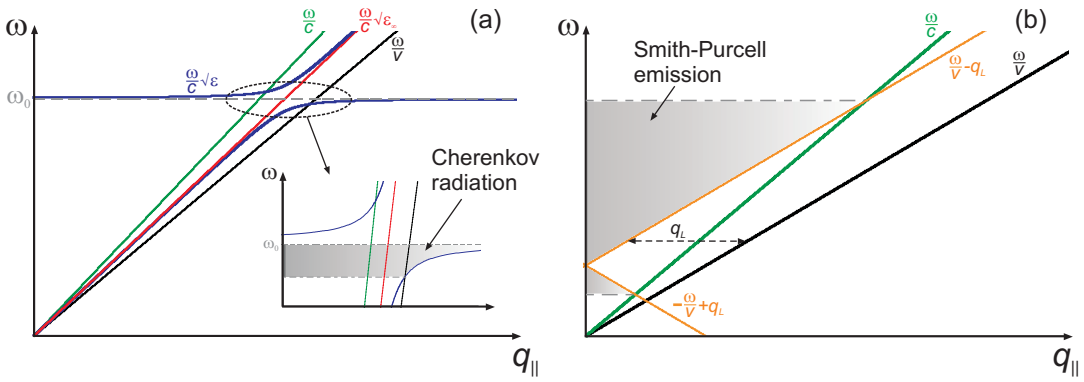

Figure 2.8: ***Dispersion relations and emission conditions for Cherenkov and Smith-Purcell radiation.*** *(a) Dispersion relation diagram illustrating the condition leading to CR emission. The straight lines represent the dispersion curves for a lightwave moving in the vacuum (green line), a lightwave moving in a medium of constant permittivity ϵ_∞ (red line) and the electron fields (black line). The blue curve describes the dispersion relation for a medium with permittivity ϵ, frequency dependent. The region where the blue and black lines cross is highlighted in the inset of the figure, where the CR emission range is indicated by the shaded region, whose upper bound corresponds to the condition of anomalous dispersion $\omega = \omega_0$; (b) Dispersion relation diagram illustrating the condition leading to Smith-Purcell emission. The electron moves in vacuum, thus the only dispersion lines present are the electron line (black) and the light-in-vacuum line (green). The presence of the grating provides a momentum q_L, which is reflected by the shift in the electron line (orange line). The shaded region indicates the range of emitted wavelengths depending on the emission angle θ*

sketched in Fig. 2.8b. In this case the velocity of the electron does not exceed the speed of the light in the medium (chosen to be in vacuum or air, for simplicity), $v < c/\sqrt{\epsilon}$, and therefore, no crossing between the dispersion curves takes place. The picture is modified by the presence of the metal grating which provides the additional momentum, q_L, to the 'electron wave', thus fulfilling the emission condition described in Eq. 2.26. The shaded region in this case covers the wavelength range dictated by the angle θ, once all the other parameters (period of the grating L and velocity of the electron, v) are fixed.

2.4 Experimental detection of electron induced radiation emission

All the processes just described in Section 2.3 require an experimental setup capable of collecting and analysing the emitted light in order to be assessed. In this section the experimental setup used for all the experiments is sketched and two examples of

its capabilities are reported.

2.4.1 Experimental setup

The setup used to perform the experiments of the thesis is divided into two main parts: a scanning electron microscope (SEM), to produce the electrons responsible for the excitation of the samples, and an optical system for the collection and analysis of the electron induced radiation emission (EIRE). The electron beam is focused onto the sample via a small hole in a parabolic mirror mounted directly above the sample. The mirror collects the light emitted from the sample over approximately half of the available hemispherical solid angle and directs it out of the SEM chamber to a spectrum analyzer with a liquid nitrogen-cooled CCD detector (Fig. 2.9). It is also possible to build up an 'hyperspectral' image of the sample by scanning it point by point with the focused electron beam and synchronously recording the light emission spectra at every pixel as described in [79]. From the data hypercube it is possible to extract spectral (e.g. emission peaks at specific wavelengths) and spatial information about the sample)

In order to asses the spectral and spatial capabilities of the system, two examples are reported in Section 2.4.2. In both cases the samples are metal nano-particles and the reason behind this choice is the ability of these object to support localised surface plasmons.

2.4.2 Investigation of light emission from metal nanoparticles

Localised plasmon resonances are important features of metallic nanoparticles of sub-wavelength dimension. They represent a way to localise light to dimension much smaller than the wavelength of the light itself, while inducing an enhancement of the intensity of the electromagnetic field in the same region. Many applications benefit from such features, for example Surface Enhanced Raman Scattering, cancer therapy, nano-antenna emitters, to cite some. For each and all of these applications the knowledge, with the highest accuracy, of the plasmonic properties (spatial intensity and energy distribution, lifetime, etc.) of the specific nanoparticle is a necessary requirement. A number of techniques are available to serve this purpose, some of them use optical fields while other employ free electrons (see [67]). All of them have both advantages and disadvantages, nonetheless, in general, techniques using free electrons such as Electron Energy Loss

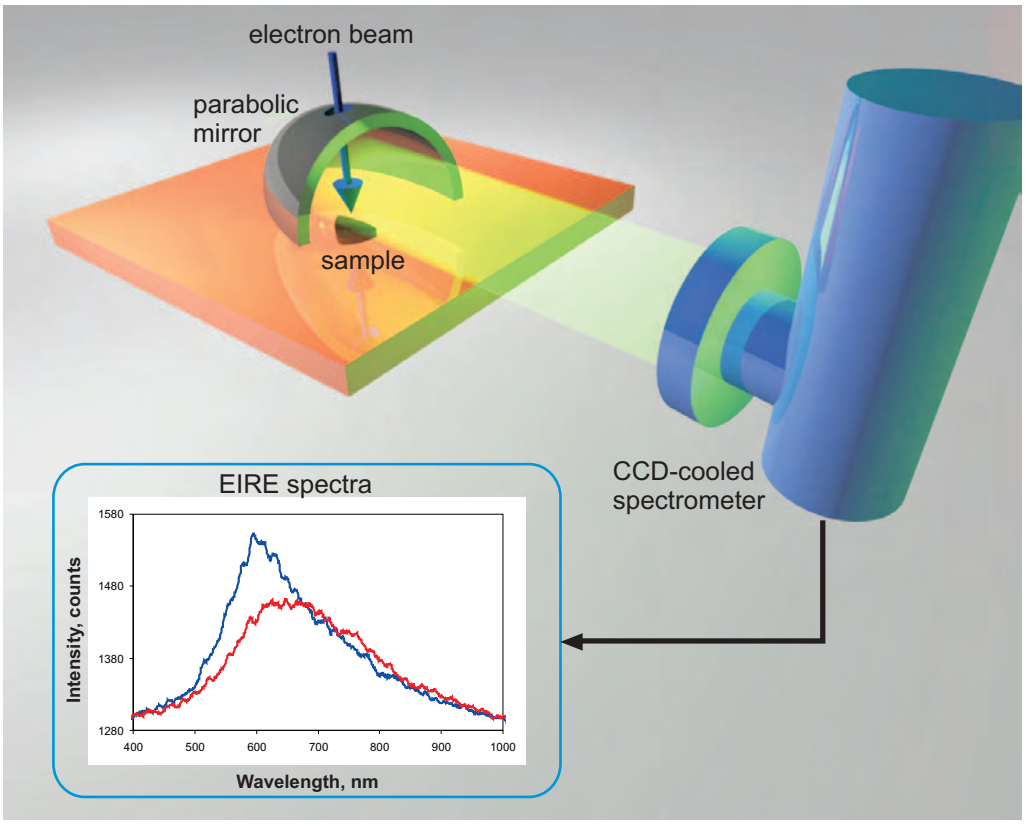

Figure 2.9: ***Schematic of the set-up for EIRE detection.*** *A beam of electron is focused onto the sample: this will induce emission of radiation that is collected by a parabolic mirror and diverted onto a liquid nitrogen-cooled CCD spectrometer.*

Spectroscopy (EELS) and Cathodoluminescence (CL), give almost unrivalled spatial and energy resolutions.

This section aims at showing how CL spectroscopy is not limited to specific nanoparticles geometries but can rather help to retrieve information about plasmonic resonances and distributions for arbitrary geometries within a wide wavelengths range and with a spatial accuracy of about 20 nm. The particles used in the experiments were gold pentagonal bipyramidal (decahedra) and triangular nanoprisms (obtained as fractions of the nanodecahedra) prepared by the group of Prof. L. Marzán at Vigo University. The particles were synthesised following the method reported in [80], using N-dimethylformamide (DMF) as both solvent and reducing agent. The optical properties of the gold nanoparticles were probed at two scales: i) single particle level (nanodecahedra) and ii) within a single particle (nanotriangles)

Gold nanodecahedra

Gold pentagonal bipyramidal nanoprisms, or nano-decahedra, belong to a class of nanoparticles, synthesized by colloidal chemistry techniques, whose importance and attractive characteristic is represnted by their anisotropy and the presence of tips in their shape. The tips, especially if sharp, are important, as said above, for applications as, e.g. SERS, because of the field enhancement they create. The current best example of such kind of metal nanoparticles are the so-called nanostars, that give a 10 orders of magnitude enhanced SERS signal [81, 82].

The nanodecahedra used in the experiments are shown in Fig. 2.10a and b. They have a lateral size of about 50 nm. The size of the particles allowed to record spectra from each single particle without, however, spatial information: the beam of free electrons was directed roughly at the centre of each single nanodecaherdon and recorded. Due to the decahedra minute dimensions, limited imaging resolution and, perhaps, small drifts induced by charging, it was not possible to precisely define the impact position, so that the particles were probably probed on slightly offset positions with respect to the centre. From statistics over numerous nanoparticles, curves peaking around 2.2 eV have been detected (Fig. 2.10c). From analogous studies performed using a transmission electron microscope (TEM) with the capability of perform electron energy spectroscopy (EELS) and produce spatial maps with very high accuracy (sub-nm), the three resonances could be assigned to specific surface modes associated to the nanodecahedra. In particular, the resonance at 2.25 eV is associated to the particle azimuthal mode, whereas the resonances at 2.05 eV and 2.15 3V are associated to polar modes located at the corners of the decahedra. The peak spectral shift is probably due to variations in the particle size.

The spectra reported in Fig. 2.10c are helpful to highlight the great energy resolutions Cathodoluminesce, like other spectrography techniques using free electrons, can achieve: in the case reported here, modes for nanoparticles with very small size variations and separated by only about 0.1 eV, have been clearly detected and associated to geometric resonance of the structure.

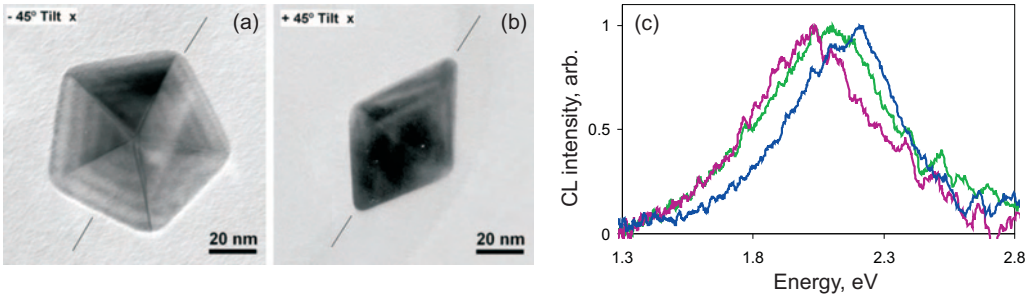

Figure 2.10: ***Cathodoluminescence emission of a single 50 nm gold nanodecahedron*** *TEM images of a single gold nanodecahedron from a top (a) and side (b) view (images from [80]); (c) CL emission spectra of a single decahedron excited by a beam of free electrons directed on its centre: resonances, centred around 2.2 eV (green) occur when collecting spectra from many nanoparticles and they are associated to geometric resonances of the decahedra.*

Gold nanotriangles

Gold nanotriangles, obtained as fractions of the nanodecahedra during the fabrication process, have the same positive characteristics of the decahedra (anisotropy, corners) and hence the same advantages (e.g. field enhancement at the corners). The triangular prisms analysed here have a slightly bigger size, 100 nm side length, than the decahedra studied in the previous section, thus are a perfect candidate to test the mapping capability of CL spectroscopy.

As shown in Fig. 2.11a the scanning electron microscope obviously has the capability of resolving the features of an individual nanotriangle therefore opening the possibility to scan the beam (point by point) over the particle surface, collect the full spectrum at each point and then build a full intensity map for the CL signal. Since each xy point contains the full spectral information, it is possible to build CL intensity maps at each wavelength as the one shown in Fig. 2.11b, where the surface plasmon resonance associated with the corner of the nanotriangle is clearly visible.

The advantage of mapping the emission on the nanoparticle, beside a direct visualisation of the plasmon modes, is that a point in the map can be probed and the spectral information carried by that point visualised, as shown in Fig. 2.11c, where two spectra, one from a corner (blue line) and one from a side (red) are compared: it is easy two see that they show resonances at different wavelengths.

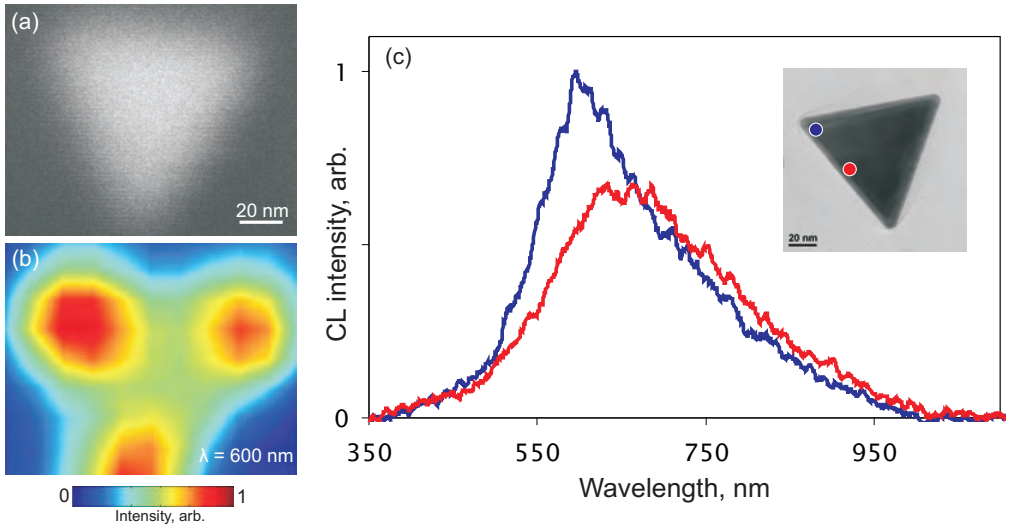

Figure 2.11: ***CL emission mapping of a 100 nm gold nanotriangle*** *(a) Secondary electron image of a gold triangle and (b) corresponding CL emission map at a wavelength of 600 nm where emission maxima can be seen on the triangle corners; (c) CL spectra generated by an electron beam hitting the triangle surface onto two different points.*

2.5 Numerical description: the boundary element method

Analytical calculation of the fields generated by the processes described above is possible only in a limited number of cases (e.g. infinite planar metal surfaces); when the structures under investigation have complex geometries, then numerical solutions to equations and integrals are required. In this thesis, the method of choice to calculate the fields induced by an electron and its interaction with the experimental structures has been the retarded boundary element method (BEM). In short, the BEM handles the fields inside each homogeneous region by expressing them in terms of charges and currents at the boundaries with other regions, calculated by imposing the boundary conditions on the interfaces.

The retarded BEM has proved to be an accurate and powerful simulation method for the analysis of the interaction of free electrons with photonic/plasmonic nanostructures [83–85]. The specific BEM code used within this thesis to model some experiments has been developed by Prof. F. J. García de Abajo. In this section it will be shown the derivation of BEM starting from Maxwell's equations , following the one carried out in [86, 87].

The BEM operates in the frequency space, thus let us start by expressing Maxwell's equations in frequency domain, ω as:

$$\begin{aligned}
\nabla \cdot \mathbf{B} &= 0, \\
\nabla \times \mathbf{E} - ik\mathbf{B} &= 0, \\
\nabla \cdot \mathbf{D} &= 4\pi\rho, \\
\nabla \times \mathbf{H} + ik\mathbf{D} &= \frac{4\pi}{c}\mathbf{J},
\end{aligned}$$

where $k = \omega/c$ and the media are described by dielectric permittivity and magnetic permeability both dependent upon space $\mathbf{r}$ and frequency ω, $\epsilon = \epsilon(\mathbf{r}, \omega)$ and $\mu = \mu(\mathbf{r}, \omega)$. The first two equations can be rewritten by expressing electric and magnetic fields in terms of scalar and vector potential ϕ and $\mathbf{A}$

$$\mathbf{E} = ik\mathbf{A} - \nabla\phi, \tag{2.27}$$

$$\mathbf{H} = \frac{1}{\mu}\nabla \times \mathbf{A}. \tag{2.28}$$

Then, using the gauge (Lorentz)

$$\nabla \cdot \mathbf{A} = ik\epsilon\mu\phi \tag{2.29}$$

Maxwell's equations can be rewritten as

$$(\nabla^2 + k^2\epsilon\mu)\phi = -4\pi\left(\frac{\rho}{\epsilon} + \sigma_s\right), \tag{2.30}$$

$$(\nabla^2 + k^2\epsilon\mu)\mathbf{A} = -\frac{4\pi}{c}(\mu\mathbf{J} + \mathbf{m}) \tag{2.31}$$

where σ_s and $\mathbf{m}$ are proportional to the gradient of spatially-dependent ϵ and μ. In the case of homogeneous media separated by abrupt interfaces, then σ_s and $\mathbf{m}$ will take nonzero values only at the interfaces, so that they can be interpreted as additional charges and currents having their origin in the discontinuity of ϵ and μ. They, however, do no represent physical quantities but are only related to real boundary charges and

currents, so that, rather than using them, it is more convenient to introduce surface charges σ_j and currents $\mathbf{h}_j$ determined by the appropriate boundary conditions for the electromagnetic fields at the interfaces.

The general solutions to equations 2.30 and 2.31 for the scalar and vector potentials, vanishing at infinity in each medium j can be expressed as:

$$\phi(\mathbf{r}) = \frac{1}{\epsilon_j}\int d\mathbf{r'} G_j(|\mathbf{r}-\mathbf{r'}|)\rho(\mathbf{r'}) + \int_{S_j} d\mathbf{s} G_j(|\mathbf{r}-\mathbf{s}|)\sigma_j(\mathbf{s}), \tag{2.32}$$

$$\mathbf{A}(\mathbf{r}) = \frac{\mu_j}{c}\int d\mathbf{r'} G_j(|\mathbf{r}-\mathbf{r'}|)\mathbf{J}(\mathbf{r'}) + \int_{S_j} d\mathbf{s} G_j(|\mathbf{r}-\mathbf{s}|)\mathbf{h}_j(\mathbf{s}), \tag{2.33}$$

where S_j indicates the boundary of each medium and

$$G_j(r) = \frac{e^{ik_j r}}{r} \tag{2.34}$$

is the Green function which solves the scalar wave equation

$$[\nabla^2 + k_j^2]G_j(r) = -4\pi\delta(\mathbf{r}), \tag{2.35}$$

in each medium j and $k_j = k\sqrt{(}\epsilon_j\mu_j)$.

The solutions found for the potentials (expressed in equations 2.32 and 2.33) can be broken in two parts; the integrals over $\mathbf{r'}$ (first integrals on the right side) are solutions to equations 2.30 and 2.31 when $\sigma_s = \mathbf{m} = 0$, which means outside the interfaces; the surface integrals are part of the solutions in order to include the effects of σ_s and $\mathbf{m}$ on the boundaries and to account for the discontinuity of the Green function G_j at the boundaries. Equations 2.32 and 2.33 are therefore solutions to, respectively, Eq. 2.30 and Eq. 2.31 if boundary charges σ_j and currents $\mathbf{h}_j$ can be chosen so that the resulting electromagnetic fields satisfy the boundary conditions.

The continuity of the tangential component of $\mathbf{E}$ and the normal component of $\mathbf{B}$ at the boundary, together with the Lorentz gauge (Eq. 2.29), leads to the continuity of the potentials ϕ and $\mathbf{A}$, meaning that they must have the same value on both sides of

the boundary, $\phi_1 = \phi_2$ and $\mathbf{A}_1 = \mathbf{A}_2$, so that from Eq. 2.32 and Eq. 2.33 one gets

$$G_1\sigma_1 - G_2\sigma_2 = \phi_2^e - \phi_1^e, \tag{2.36}$$

$$G_1\mathbf{h}_1 - G_2\mathbf{h}_2 = \mathbf{A}_2^e - \mathbf{A}_1^e, \tag{2.37}$$

where ϕ_j^e and $\mathbf{A}_j^e$ are derived from the first integrals of, respectively, Eq. 2.32 and Eq. 2.33, evaluated at $\mathbf{r} = \mathbf{s}$. They are equivalent boundary sources, representing the scalar and vector potentials corresponding to those created at the interface points by external charges and currents in the case of the entire space being homogeneously filled with medium j, and scale linearly with these external perturbations.

In the case of nonmagnetic materials, the continuity of the tangental magnetic field and the vector potential implies that both the tangential derivatives of all components of the vector potential and the normal component of the tangential vector potential must be continuous. This, together with the Lorentz gauge, leads to the following equation

$$H_1\mathbf{h}_1 - H_2\mathbf{h}_2 - ik\mathbf{n}_S(G1\epsilon_1\mu_1\sigma_1 - G2\epsilon_2\mu_2\sigma_2) = \alpha \tag{2.38}$$

where $\alpha = (\mathbf{n}_S \cdot \nabla_\mathbf{S})(\mathbf{A}_2^e - \mathbf{A}_1^e) + ik\mathbf{n}_S(\epsilon_1\mu_1\phi_1^e - \epsilon_2\mu_2\phi_2^e)$, $\mathbf{n}_S$ the surface normal and H_j the normal derivative of the Green function G_j.

When the continuity of the normal component of the electric displacement $\mathbf{D}$ is taken into account then the following equation holds

$$H_1\epsilon_1\sigma_1 - H_2\epsilon_2\sigma_2 - ik\mathbf{n}_S \cdot (G1\epsilon_1\mathbf{h}_1 - G2\epsilon_2\mathbf{h}_2) = D^e, \tag{2.39}$$

where $D^e = \mathbf{n}_S \cdot [\epsilon_1(ik\mathbf{A}_1^e - \nabla_\mathbf{S}\phi_1^e) - \epsilon_2(ik\mathbf{A}_2^e - \nabla_\mathbf{S}\phi_2^e)]$ is the difference of the normal displacements created at the interface points by external sources in the case of the entire space being filled with a single homogeneous medium, either 1 or 2.

Equations 2.36 to 2.39 allow to self-consistently calculate the boundary charges and currents σ_j and $\mathbf{h}_j$ thus making Eqs. 2.32 and 2.33 solutions to the Maxwell's equations,

that vanish at infinity and satisfy the boundary conditions at the interfaces. The travelling free electron can be introduced as an external charge through the inhomogeneous terms.

2.6 Coherence of a light source

When discussing about light sources, it is straightforward to refer to lasers as term of comparison. There are differences between the "incoherent" light emitted by a thermal source and the "coherent" light emitted by a laser. In particular laser emission is usually distinguished by ordinary light sources by its *spatial coherence* and its *temporal (or spectral) coherence*. In this section a definition of both kinds of coherence is provided, while a mathematical formulation of first-order coherence is given in Appendix A. The description of coherence will follow that presented in textbooks [88, 89].

It is worth pointing out that the coherence properties are primarily connected to the classical-resonant-cavity properties rather than to the quantum transition properties of the atoms in the gain medium.

Temporal coherence

A signal is said to be *temporally coherent* if its amplitude and/or phase at one moment in time are strongly correlated to the amplitude and/or phase at any earlier or later time. The coherence time is inversely proportional to the bandwidth of the signal (see Appendix A). In general, thermal light sources, as for example, flashlamps or filament sources emit over a very broad spectrum, resembling that of a blackbody radiator; there are light sources, as e.g. discharge lamps, that emit over much narrower wavelength bands, but their spectral width is still limited by atomic transitions' linewidths. Typical values for the linewidths of these light sources are in the order of few THz. Most lasers, on the contrary, have a highly monochromatic emission whose bandwidth can range from few tens of MHz to only a few Hz (in a very highly stabilised system). As said just above, this spectral property of the laser mainly comes from the cavity and not from the atomic transition.

Spatial coherence

Spatial coherence of a light source is defined by the phase relation between two points on the wavefront of an electromagnetic wave at a time $t > 0$. The difference between the phases at time $t = 0$ is, by definition, zero; if the difference remains the same at any $t > 0$, for any two points of the wavefront, then the the wave is said to have emphperfect spatial coherence. In practical situations, the requirement of good phase correlation between two points is extended only to a limited area, in which case the wave is said to have *partial spatial coherence*.

It is important here to stress two points: i) the spatial and temporal coherence are independent concepts (it is possible to have a wave with very high spatial coherence but very poor temporal coherence, and viceversa); ii) spatial and temporal coherence give just a first-order description of the coherence of a light source. Despite the fact that through the investigation of spatial and temporal coherence of a practical light source it is, generally, possible to say whether it is or not a laser, are indeed the differences in higher-order coherence that make a laser source fundamentally different from an ordinary light source. A slightly deeper explanation of this aspect can be found in Appendix A.

2.7 Conclusions

The theoretical analysis of the interaction process between free electrons and specimens presented in this chapter covers all the main mechanisms of light emission involved in the experiments reported in this thesis.

The description of these effects in a sequential way, however, does not have to induce to think that they are mutually exclusive, but on the contrary the resulting light emission comes rather from their mutual interplay in the structure under investigation.

As already anticipated, the aim of this thesis is to show that electron beam pumping is a viable route to the realisation of nanoscale light sources, which sometimes also have characteristics that arise from the unique features typical of the free-electrons/matter interaction. In the next three chapters, three experiments are reported where light emission comes from nanoscale metallic structures excited by beams of free electrons.

For each of them, the process leading to emission of optical radiation is different, and always depends on the particular geometry of the sample, which has been designed to take advantage of some of the mechanisms of light emission previously described. A very interesting aspect is the fact that in some cases the emission of light cannot be directly related to a single process, but rather comes both from a modification of one or more of the effects just described due to the geometry of the structure and the interplay between few of them (e.g . Chapter 4). Even more interestingly, the excitation by free electrons, mediated by generation of surface plasmons, has shown capable of triggering spatially coherent emission from metal nanostructured materials (Chapter 5).

3

Nanoscale Hertzian antenna driven by free electrons

Dipole antennas are the simplest devices to transmit and receive an electromagnetic signal. Such antennas are made of two arms; the gap between the arms is used to feed the signal to the antenna which decouples it to the free space. Here it is demonstrated a nanometer size equivalent of the dipole antenna where the feed is represented by a beam of free electrons impinging in the area of closest proximity between the two arms of the antenna.

3.1 Introduction

Several studies have so far reported emission of radiation from metal nanoparticles when excited by beams of energetic free electrons and mapping of the particles' plasmon modes [57, 58]. The beam of free electrons acts as a nanoscale, localised, broadband source of plasmons on a metal surface. In the case of a metal nanoparticle, the free electrons generate standing surface plasmons on its surface which in turn scatter into free-space propagating light and can thus be detected. Intensity maxima in the emitted light happen when the electrons hit positions on the particles corresponding to nodes of the plasmon modes. In general, the optical properties of metal nanoparticles depend on particle shape and size and on the dielectric environment [90] and likewise do the electron induced radiation emission (EIRE) intensity maxima.

In recent years a big research effort has been devoted to investigate the optical behaviour of two or more closely spaced nanoparticles: when the particles are properly arranged they show behaviours similar to their macroscopic counterparts, *antennas*, as described in Section 1.2. Like in the case of radio or microwave antenna, optical nanoantennae, when illuminated with an optical signal, show a manifold increase of the local field around the region where usual antennas are usually fed; furthermore, it has been suggested that their performance can be affected by acting on that area.

Taking advantage of this close analogy between nano- and macro-antennas and of the capability of energetic free electrons to excite surface plasmons on metal nanoparticles, it is reported in this chapter the first demonstration of an optical nanoantenna operating in the transmission regime, fed by free electrons. After the fabrication and characterization methods are described in Section 3.2.1 and the emission from single nanorods is analysed in Section 3.2.2, in Section 3.2.3 it is stressed how enhanced emission is obtained from the antenna when it is fed in the right position, meaning where it is highest the local density of states (LDOS) for the specific arrangement of the metal nanoelements. In the end of the chapter, Section 3.2.4, the reciprocal behaviour of the nanoantenna in transmission and reflection is discussed.

3.2 Transmitting nanoscale hertzian antennas

Structures akin to the dipole antenna introduced by Heinrich Rudolph Hertz around 1886, comprising an arrangement of two metallic rods with a center-fed driven element, have recently attracted considerable attention as potential nanoscale 'optical antennae'. Such antennae would be able to efficiently couple the energy of free-space radiation to a confined region of sub-wavelength size, or to modify the amount and direction of electromagnetic energy emitted into the far-field from nanoscale optical or plasmonic sources. [91, 92] These components are expected to find applications in field-enhanced single-molecule spectroscopy [6] and as elements of future nanophotonic circuits. [92,93] Thus far, experimental studies of nano-antenna structures have largely been conducted using a combination of optical far-field measurements and near-field scanning probe microscopies to investigate the interplay between plasmonic excitations and light [94, 95].

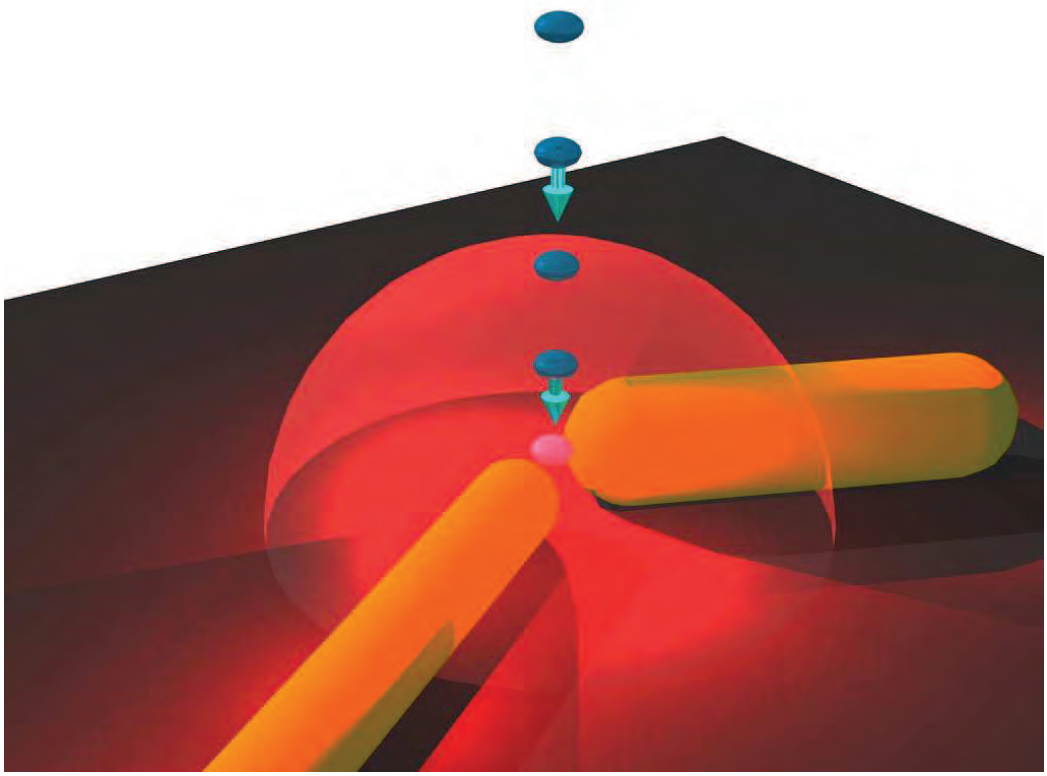

Figure 3.1: ***Artist's impression of a transmitting nanoscale optical antenna driven by an electron beam at the junction between rods.*** *A pair of coupled gold nanorods efficiently transfers the energy of electrons focused on the junction into far-field optical radiation.*

However, It has recently been shown that electron beams, which can of course be focused to nanoscale spots, provide alternative highly localized means of generating light [96] and surface plasmons on the nanoscale: indeed, spatially-resolved mapping of plasmon modes in metallic nanostructures [58, 79, 97–101] has been facilitated by the fact that an electron beam impacting on a metal surface acts as a mobile, broadband, nanoscale surface plasmon source [63, 64]. For example, in the case of single gold and silver nanorods such techniques reveal standing wave plasmonic modes resulting from interference between the excited SPPs and back-scattered SPPs reflected from the ends of the rod. [58,98,99]. Here it is reported on the experimental realization of *transmitting* optical antennae based on coupled gold nanorods and pumped by a *free-electron beam*. Strongly enhanced antenna efficiency is observed for electron injection points in the vicinity of the junction between rods (Fig. 3.1).

3.2.1 Fabrication and characterization of optical nano-antennae

The antennas were assembled from gold nanorods synthesized using the seed-mediated growth method [102, 103] where two solutions, the seed and the growth, are separately prepared with the former being then added to the latter, then mixed and let rest. The nanorods preparation was carried out by Dr. J. Edgar, Dr. M. D. Arnold and Prof. M. J. Ford at the University of Technology in Sidney. The antennas were then dispersed from colloidal suspension by drop-casting and desiccation on a silicon substrate. Among the randomly distributed nanoparticles, isolated single nanorods and coupled nanorod pairs (of arbitrary mutual orientation) were identified for study. Imaging and parallel analysis of electron-beam-induced radiation emission (EIRE) were performed in a scanning electron microscope (SEM) equipped with a hyperspectral light collection system [79], as described in section 2.4.1.

In the present study, data were recorded for wavelengths between 450 and 850 nm with an electron acceleration voltage of 40 kV and a beam current of 4.5 nA. Separate measurements of substrate (silicon) cathodoluminescent emission enabled background subtraction from the experimental data. This technique relies on the fact that energy is coupled from incident electrons to the plasmonic modes of the antenna structure and subsequently to propagating light modes, which constitute a decay channel for the plasmons. [67, 98] It should be emphasized that EIRE mapping reveals the efficiency

with which electron energy is coupled to far-field radiation as a function of electron injection position and *not* the distribution of light emission, i.e. while the electron-beam excitation is confined to a nanoscale spot, the associated optical emission may come from any part of the structure).

3.2.2 Emission from single nanorod

Hyperspectral EIRE mapping of a single, isolated gold nanorod (Fig 3.2) reveals the kind of plasmonic standing wave modes recently reported by Vesseur *et al.*, [58] with emission resonance wavelengths dictated by the dimensions of the rod. The wavelength of the emitted light can be easily related to the wavelength of the plasmon generated on the nanorod at that specific wavelength: the distance between two neighbouring maxima corresponds to $\lambda_p/2$, where λ_p is the surface plasmon polariton (SPP) wavelength.

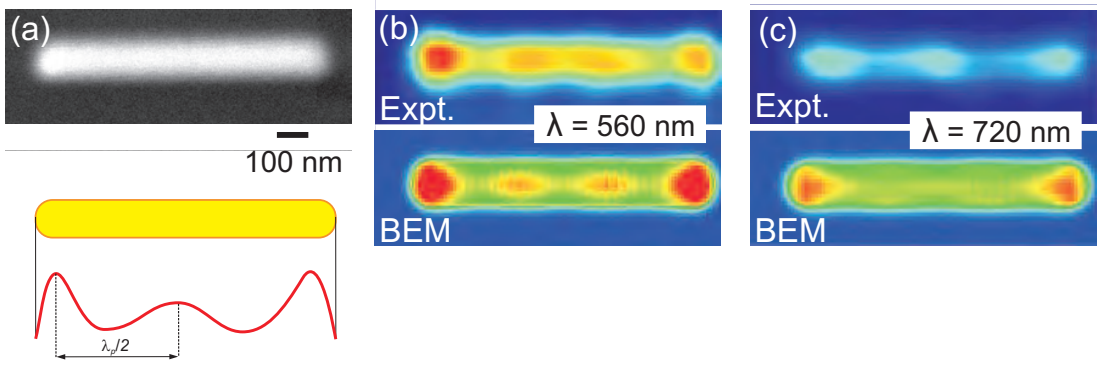

Figure 3.2: ***EIRE maps of a single gold nanorod*** *(a) Secondary electron image of an Au nanorod and schematic of a plasmon standing wave on the rod; (b) EIRE map of the rod in (a) at a wavelength of 560 nm; (c) EIRE map of the rod in (a) at a wavelength of 720 nm.*

For example, in the case of the rod of Fig 3.2, at the wavelength of 560 nm the EIRE map shows 4 peaks, meaning a $3/2\lambda_p$ standing plasmon wave. These emission characteristics are elegantly reproduced in numerical simulations employing a fully three-dimensional implementation of the boundary element method (BEM-3D) for rigorously solving Maxwell's equations (Fig 3.2 b and c). [67, 84]. BEM simulations for both single and coupled rods were performed by Dr. V. Myroshnychenko at the Insituto de Optica in Madrid.

3.2.3 Coupled nanorods

In coupled nanorod configurations light emission is found to be substantially stronger for electron beam injection points in the vicinity of the rods' junction than for any other point on the structure (Figs. 3.3b and 3.4a,b). Consider for example the coupled nanorod pair shown in Fig. 3.3b, where the horizontally aligned rod has dimensions very similar to those of the isolated rod in Fig. 3.3a. The EIRE spectrum for the junction region shows two maxima at 560 and 720 nm (Fig. 3.3c). EIRE intensity maps at these wavelengths illustrate that light emission at 720 nm is particularly strongly enhanced: The emission intensity is at least two times higher for electron beam injection points in this region than for any other point on the nanorods, or indeed any point on the corresponding isolated rod.

The behavior of coupled metallic nanorods as optical antennae can be related to the spatial distribution of the electromagnetic 'local density of states' (LDOS) [104] around the nanostructure. Indeed, while a direct reciprocal analogy cannot be drawn between the transmitting antennae presently under consideration and more familiar optically illuminated receiving antennae, the local field enhancements achieved at the junctions of the latter are a reflection of the elevated LDOS in that region [93, 105]. The photonic LDOS, similarly to its electronic counterpart, can be defined as the combined local intensity of all eigenmode of the system under consideration. It has been recently suggested that the photonic LDOS of a sample can be probed with an electron beam via electron energy loss (EELS) and cathodoluminescence spectroscopies [106, 107]. Indeed, a rigorous relation holds between EELS and LDOS for 2D systems; for arbitrary 3D systems a simple rigorous relation has not been reported so far, but some numerical results point out a qualitative relation between the two quantities in certain geometries [106]. For seek of completeness it needs to be pointed out that it has been recently argued that EELS and LDOS, although intimately related, provide complementary information and, in general, differ (in particular near particle gaps, where enhancement of electric field happens for directions roughly perpendicular to the electron trajectory) because the electron and its stopping via the induced field have a delocalized nature, compared to the fields of the point dipole in terms of which the 3D LDOS is defined [108].

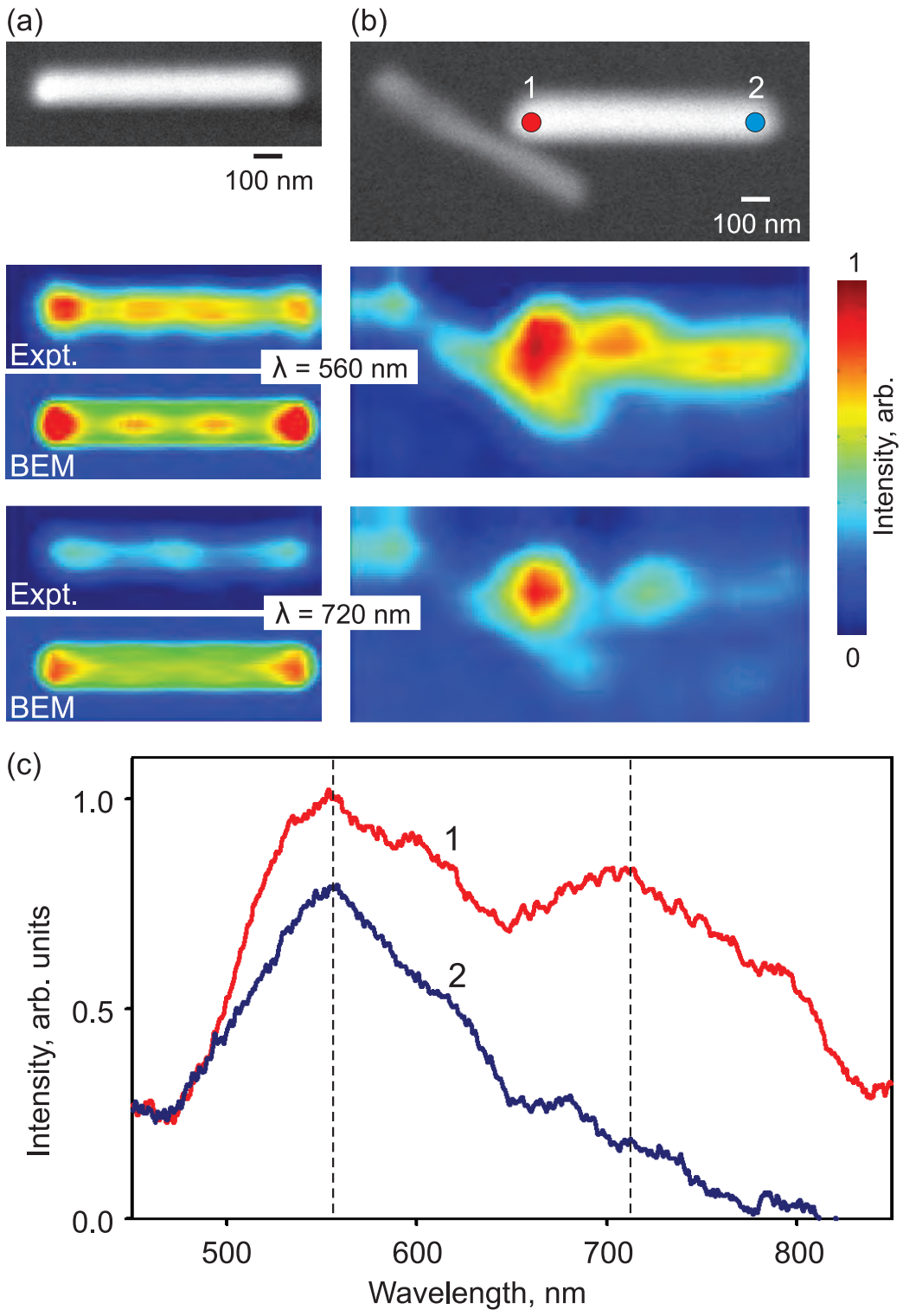

Figure 3.3: ***Single nanorod vs coupled rods EIRE emission*** *Scanning electron microscope (secondary electron) images and corresponding electron-beam-induced radiation emission (EIRE) excitation efficiency maps at 560 and 720 nm for (a) an isolated gold nanorod, alongside corresponding numerically simulated EIRE maps for a free-standing rod at these wavelengths; and (b) a pair of coupled gold nanorods including one rod with dimensions similar to those of the isolated rod in (a). (c) EIRE spectra for electron beam injection points* 1 *and* 2 *highlighted on the secondary electron image in (b).*

In the present case of coupled nanorods pair, enhanced light emission is observed for electron beam injection points in the proximity of the junction between the rods, i.e. the region of increased LDOS (such as point 1 in Fig. 3.3b). This increased LDOS gives rise to enhanced electron energy loss leading to increased surface plasmon generation and ultimately light emission. In contrast, when the electron beam targets the distal end of a coupled rod (e.g. point 2 in Fig. 3.3b), the LDOS it encounters is lower (essentially the same as that which it would find in an isolated rod), and light emission is correspondingly weaker.

In the terminology of electrical engineering, the junction between the rods provides an optimal feed point analogous to the ideal feed location at the center of the dipole for a microwave antenna. Here, one should consider the beam of electrons not as a continuous stream of current in free space, but rather as individual electrons electrons flying across the junction one after another. Through the Coulomb interaction, which disturbs the equilibrium of the electron distribution, the passing electrons induce oscillating currents (plasmons) in the poles of the Hertzian antenna. The free-electron feed is coupled most efficiently to the antenna when the current oscillations are resonant with the radiating modes of the antenna, in this case in the optical part of the spectrum.

Figs. 3.4a and 3.4b show respectively an SEM image and an experimentally measured 570 nm EIRE map for a pair gold nanorods in a different geometric configuration, illustrating once more the increased strength of emission for injection points in the vicinity of the rods' junction. (The EIRE spectrum for electron injection at the junction is shown in Fig. 3.4d) It is apparent from the experimental examples presented in Figs. 3.3 and 3.4, and confirmed in BEM simulations of touching and non-touching antenna configurations similar to the experimental ones (such as shown in Fig. 3.4c), that EIRE is maximized in these asymmetric antennae for electron injection points offset slightly from the centre point of the junction (SEM resolutions was not enough to locate the hot-spot with absolute certainty). This is to be expected in situations where junctions are formed between arbitrarily oriented rods of different length and diameter, and typically between the end of one rod and the side-wall of the other: Under such circumstances the plasmonic modes of the two rods will have differing interactions with the junction and the LDOS is unlikely to be distributed symmetrically about the junction.

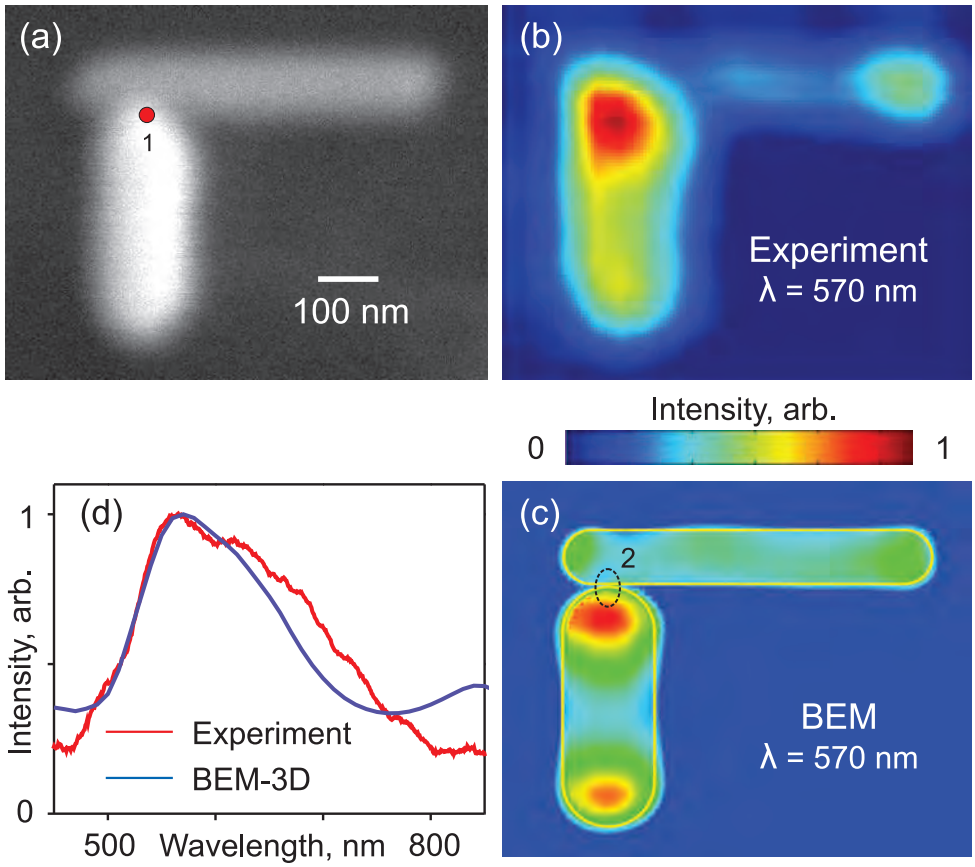

Figure 3.4: ***EIRE emission of an optical Hertzian nanoantenna*** *(a) Scanning electron microscope image and (b) corresponding EIRE excitation efficiency map at 570 nm for an L-shaped gold nanorod antenna; (c) Numerically simulated (BEM-3D) 570 nm EIRE map for such a configuration; (c) Normalized spectral dispersion of experimentally measured EIRE [red line] for an electron injection point at the junction between the rods [point* 1 *in part (a)] and numerically modelled EIRE [blue line] for the junction region [averaged over injection points at the centre of the junction and 10 nm either side - zone* 2 *in part (d) - to account for the real beam size in experiment].*

3.2.4 Receiving characteristics of the nanoantenna

It was clearly stated in the previous chapter that a direct reciprocal analogy cannot be drawn between the transmitting antennae presented so far and more familiar optically illuminated receiving antennae. However it is worth looking at the fields distribution of a receiving antenna of similar configuration and try to draw some analogy between the two cases.

Fig. 3.5a shows the numerically simulated intensity map of $|E_z|$ (the component of the electric field which describes the surface plasmons on the nanorods) on the surface of the $L-$shaped antenna at the wavelength of 570 nm (EIRE experimental maximum)

when this is illuminated by a plane wave incident perpendicularly to the plane of the antenna. The numerical simulation has been carried out using the commercial software Comsol Multiphysics, using experimental values (Johnson and Christy, 1972) for the permittivity of gold, retrieving nanorods dimensions from secondary electron images and assuming a 5 nm gap between them. The field intensity shown in the figure is obtained as average of the field distribution generated by a $x-$polarized incident wave (parallel to the long rod main axis) and a $y-$polarized incident wave (parallel to the short rod main axis); the choice of accounting for both polarizations is made to have a more fair comparison with electron excitation, which does not excite preferentially a specific polarization in the rods. The map shows an electric field enhancement in the gap of the nanoantenna that extends to the end caps of the two nanorods facing the gap, very much alike the experimental and simulation EIRE maps presented in 3.2.3.

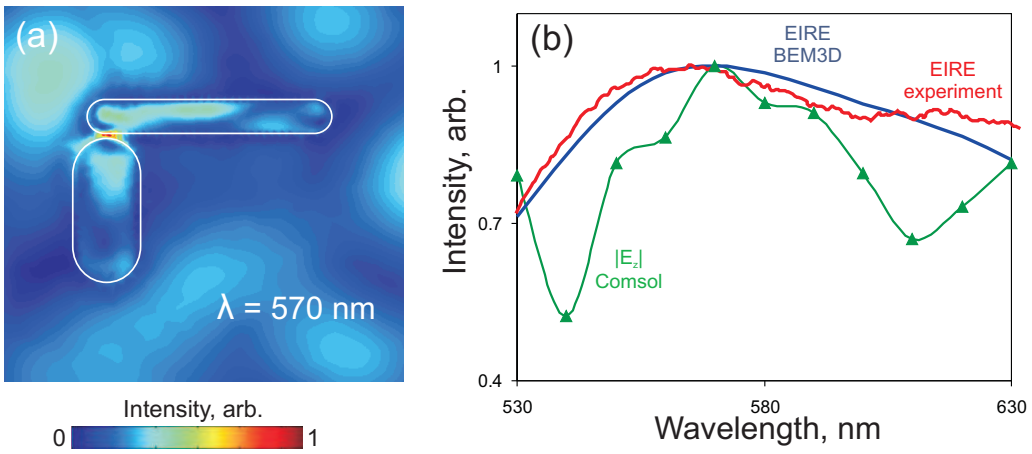

Figure 3.5: ***Optical nanoantennas in receiving mode*** *(a) Numerically simulated (Comsol) $|E_z|$ intensity map at 570 nm for an L-shaped gold nanorod antenna illuminated by plane wave (average of excitation by $x-$polarized and $y-$polarized waves); (b) Integrated intensity, over the region around the gap between the two rods, of the simulated $z-$component of the electric field (triangles and corresponding trend-line), compared with the experimental and simulated (BEM3D) EIRE integrated over a corresponding area [wavelengths range around maximum at 570 nm] .*

In order to extend further the comparison between reception and transmission mode of the nanoantenna under investigation, in Fig.3.5s are plotted the intensity distributions integrated over a region across the gap, for both $|E_z|$ (reception mode) and EIRE (transmission mode) on a wavelength range around the antenna experimental emission maximum, $\sim$ 570 nm. In *red* and *blue* continuous line are reported the EIRE emis-

sion intensity of a transmitting antenna for experimental and numerically simulated case respectively, while the *green* triangles and line indicate the numerically simulated intensities of $|E_z|$. The similarities between experimental, BEM3D and COMSOL simulations are not perfect, but there is indeed a correspondence between the increase in the local field of the receiving antenna and the increase in emitted light intensity around 570 nm.

3.3 Conclusions

In this chapter the first example of free-electron driven nanoscale optical Hertzian antenna has been discussed. Experiments have demonstrated that a pair of arbitrarily oriented coupled gold nanorods can act as a centre-fed resonant transmitting optical antenna, converting energy from a focused electron beam excitation into far-field light. Such free-electron pumped transmitting antennae are most efficiently fed in the vicinity of the junction between rods where the local density of electromagnetic states is elevated. Furthermore, at the end of the chapter an attempt to suggest a more complete picture has been done through a quick discussion of the receiving performances of one of the antenna configurations, and some hints on the possibility of reciprocal behaviour have been sketched.

4

The Light-well

Fundamental components for nanophotonic circuits to become a reality are the (nanoscale) light sources, ultimately lasers. A highly desirable characteristic for these sources is tunability, which has not been achieved so far in nanoscale light sources and remains a challenge for macroscopic devices. Taking inspiration from macroscale free-electron radiation sources such as synchrotrons and free-electron lasers, that are among the brightest and most widely tuneable light sources available today, it is here reported about the first tuneable nanoscale light source driven by free electrons, the Light-Well. In the first part of the chapter the experimental demonstration of the Light-Well is presented, while in the second its features are investigated through numerical simulations.

4.1 Introduction

It is widely recognized that the future advancement of technology will depend critically on whether the current trend for the miniaturization of sophisticated devices can be sustained. Indeed, multi-billion dollar initiatives around the world, such as the USA's National Nanotechnology Initiative [109], currently give the highest priority to research on fundamental nanoscale phenomena and nanomaterials. In particular, with a view towards future highly-integrated nanophotonic devices, there is growing interest in nanoscale light and surface plasmon-polariton sources [12, 25, 27, 110, 111]. With this in mind, and with ongoing rapid developments in the technology of chip-scale free-electron sources making highly-integrated chip-scale free-electron devices a realistic possibility [112], there is growing interest in the opportunities presented by new phenomena and functionalities found at the interface between nanophotonics (including plasmonics) and electron-beam optics in nanostructured media.

In such applications, the primary attraction of free electrons is the fact that they can be focused and positionally-controlled on the nanometer scale - far below the diffraction limit of light. An electron beam can, for example, act as a highly localized source of surface plasmon-polaritons on unstructured metal surfaces [63, 64] (enabling high-resolution mapping of plasmonic modes in nanostructures [58, 79, 83]), or as an excitation source for selective switching of phase-change memory elements (presenting the possibility of terabit-per-square-inch data storage densities [113]).

In this chapter it is reported on the first demonstration of *tuneable* light emission from a chip-scale free-electron-driven source - a 'light-well' - in which optical (visible to near-infrared) photons are generated as an electron beam travels through a nanohole in a layered metal-dielectric structure. With a lateral size of just a few hundred nanometres, and the notable advantage of wavelength tuneability, such structures may find varied application, for example in nanophotonic circuits as on-chip light sources, or in densely packed ensembles for optical memory and field emission or surface-conduction electron-emitter displays [112].

The chapter is substantially divided into two parts: Section 4.2 is dedicated to the description of the experiments demonstrating light emission from the investigated nanostructures and its tuneability, while Section 4.3 dwells, both analytically and with

the aid of numerical simulations based on the Boundary Element Method (BEM), into the mechanisms responsible for light emission and how this is affected by the features of the light-well.

4.2 Experimental realisation of tuneable emission of light

The light-well belongs to a broad family of free-electron-driven radiation sources wherein emission occurs as electrons interact with a periodically structured environment. These range from small Smith-Purcell sources [75], which emit a continuum of wavelengths over a broad angular range as electrons pass over the surface of a metal grating (with a period typically in the micro- to millimeter range), as described in Section 2.3.4, to macroscopic free electron lasers that generate high levels of directed coherent radiation as electron pulses traverse magnetic undulators [114]. In such sources the wavelength of emitted light can be tuned by adjusting the energy of the electron beam or the structure of the periodic surroundings. In the light-well a beam of free electrons experiences an alternating environment as it travels through a tunnel in a periodically layered metal-dielectric nanostructure and optical photons are emitted as a result. In keeping with other free-electron sources, the wavelength of radiation emitted by the light-well can be tuned by adjusting the energy of the incident electrons. It is reported here on incoherent near-infrared emission but it is anticipated that the light-well concept may be developed to achieve coherent operating modes and scaled to cover a very broad range of wavelengths extending to the terahertz and ultraviolet domains.

Experimental light-wells (see Fig. 4.1) were fabricated by Dr. C. M. Wang, Dr. Y.H. Fu and Prof. D. P. Tsai[1], at the National Taiwan University, in a stack of eleven alternating silica and gold layers (six silica and five gold), each with a thickness of 200 nm, sputtered onto a thick gold base layer on a silicon substrate. Wells with typical diameters of around 700 nm were milled through the stack into the base layer, perpendicular to the plane of the layers, using a focused ion beam.

Characterization of the light-well as an optical source was performed using the experimental setup described in Section 2.4.1. The electron beam of the scanning electron microscope (SEM), focused to a spot with a diameter of ∼30 nm, was used to drive

[1]Dr. Fu also helped with the experimental characterization of the light-well samples

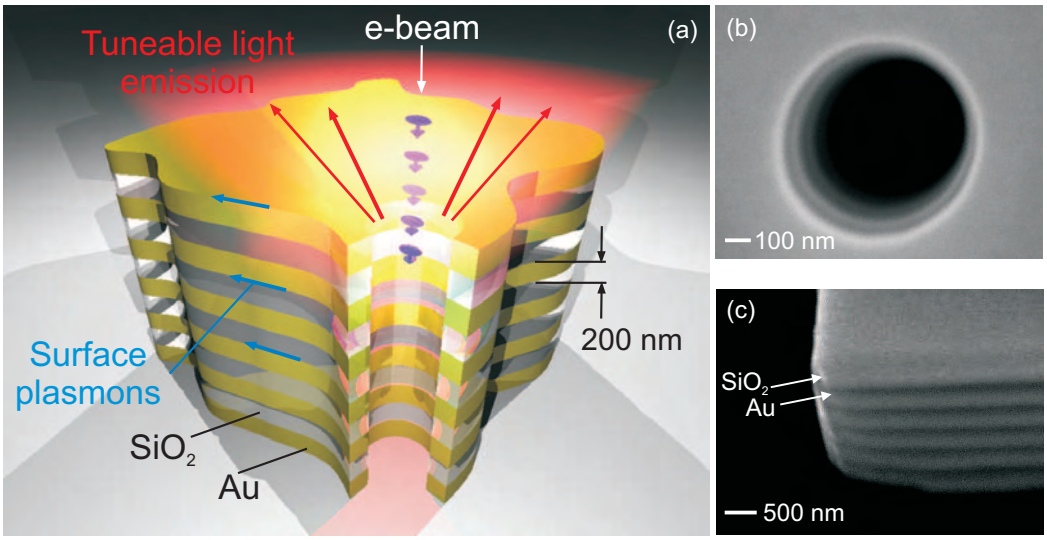

Figure 4.1: ***Artist impression of a Light-Well and Secondary Electron Images of its structure.*** *(a) Schematic cut-away section of a light-well, which comprises a nano-hole through a stack of alternating metal and dielectric layers, into which an electron beam is launched. Light is generated as electrons travel down the well and encounter a periodic material environment. (b) Scanning electron microscope image of a light-well fabricated in a gold-silica multilayer. (c) The alternating metal-dielectric layer structure as seen at an exposed corner of the sample.*

light-well optical emission. Emission spectra were recorded at different acceleration voltages and beam currents (measured using a Faraday cup in the SEM column) for a number of beam injection points along the diameter of the nano-hole, with reference measurements also taken for beams impacting the top (silica) surface of the multilayer outside the hole.

The following characteristic emission features have been observed:

1. When the electron beam hits the surface of the structure outside the hole, light emission is observed with a broad spectrum centered at 640 nm (Fig. 4.2). Within experimental accuracy this spectrum does not depend on the electron acceleration voltage and is attributed simply to cathodoluminescence and backward transition radiation from the silica-gold multilayer structure [65, 115, 116].

2. When the electron beam is injected into the nano-hole the emission spectrum contains two peaks (I and II) with spectral positions that depend on the electron acceleration voltage, as shown in Fig. 4.3 and its inset. The emission intensity is found to increase as the injection point approaches the wall of the light-well as illustrated for peak I in Fig. 4.7.

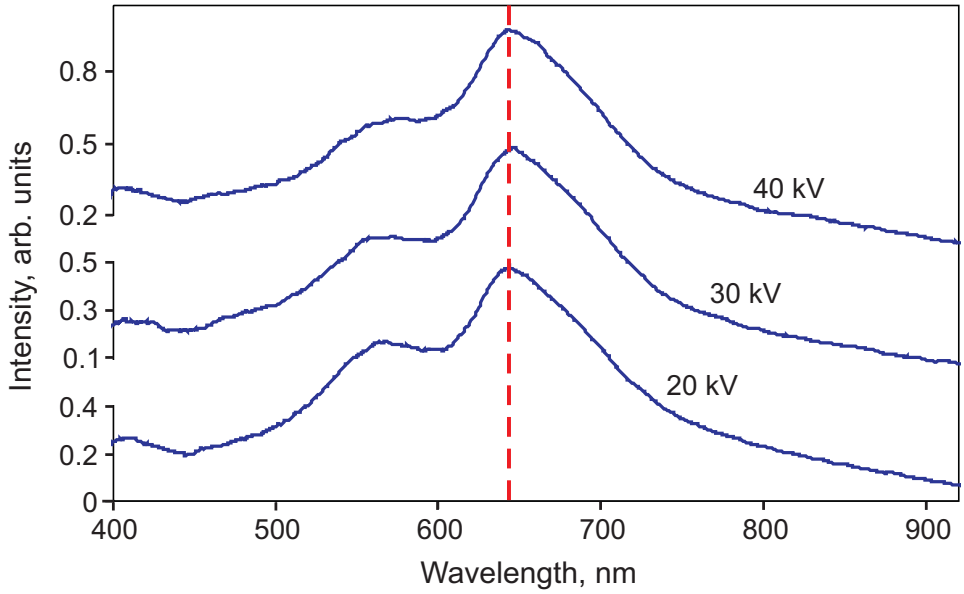

Figure 4.2: ***Electron induced emission from the materials of the light-well.*** *Emission spectra for an electron beam impact point outside the light-well, i.e. on the top surface of the gold-silica multilayer, for a range of electron acceleration voltages.*

3. For a fixed injection point and electron acceleration voltage, the emission intensity increases linearly with beam current (Fig. 4.4).

The efficiency of the emission process has been evaluated in terms of the number of photons at the peak wavelengths generated per incident electron. The number of photons are derived from a multiple gaussian fit to the recorded spectra (Fig. 4.5), taking into account the throughput efficiency of the light collection system; the corresponding number of electrons being given by the beam current and sampling time. It is found to reach 1.9×10^{-5} for peak I and 3.4×10^{-5} for peak II at 40 keV, giving a light source with an output power of the order of 0.1 nW in either case; an emission intensity of $\sim$200 W/m^2.

4.3 Modelling of the emission process and features

Here, it is considered the complex combination of material and geometry-dependent mechanisms contributing to the light-well emission process, and it is both given an approximate analytical description of the processes involved in the light generation and emission measured in the experiments and employed the boundary-element to model the emission characteristics.

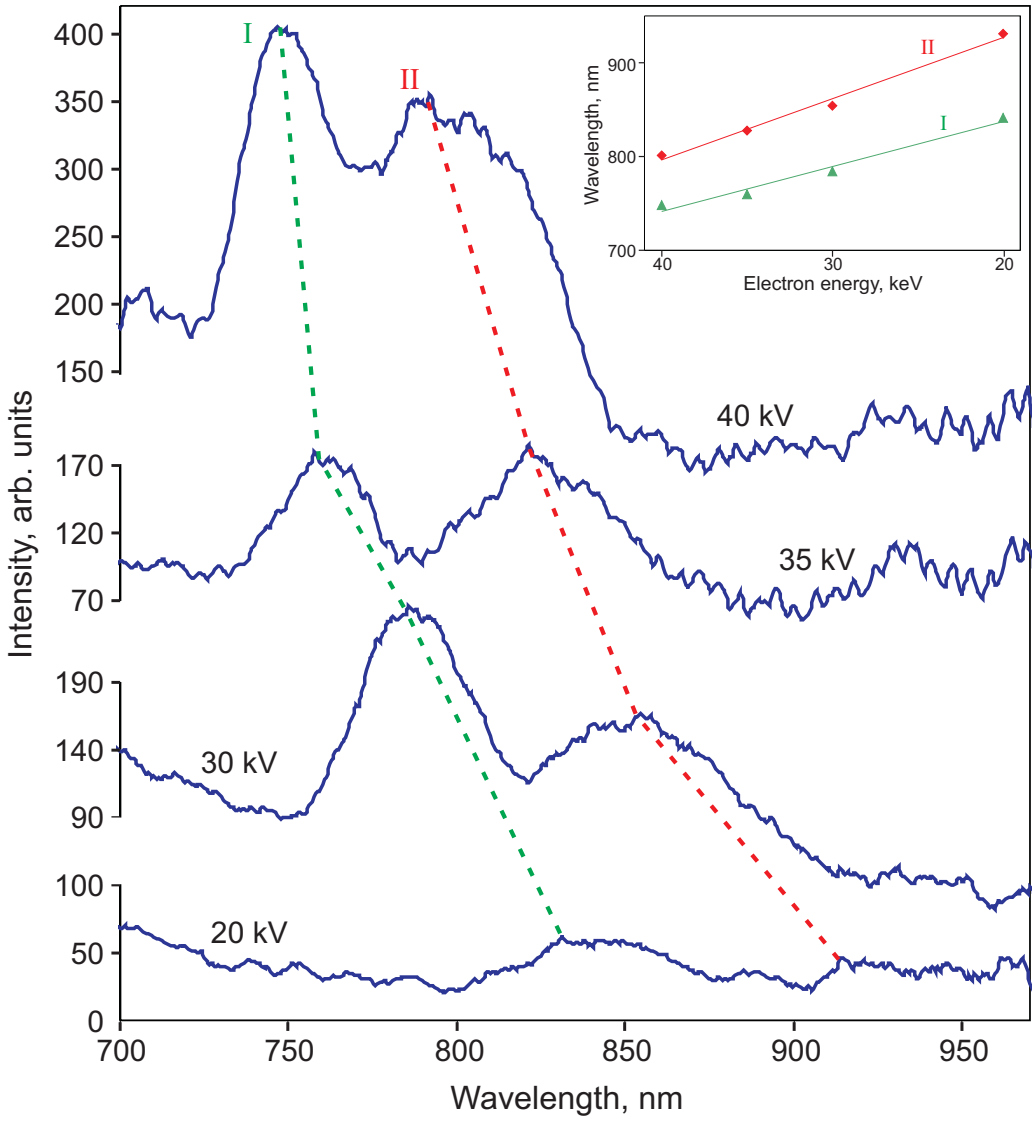

Figure 4.3: ***Experimental realisation of tuneable light emission.*** *Emission spectra for a 750 nm diameter well for acceleration voltages of 20, 30, 35 and 40 kV with a beam injection point ∼100 nm inside the wall of the well. Inset shows the position of the two emission peaks as function of the electrons energy.*

4.3.1 Analytical approximation

Though structurally simple, the light-well's emission characteristics are controlled by a complex combination of material- and geometry-dependent processes that cannot presently be described within a single analytical or numerical model. To a first approximation, one may consider that light emission originates from an oscillating dipole source created as electrons experience a periodically modulated potential within the well. In this simplified picture, an electron passing through a metal section of the

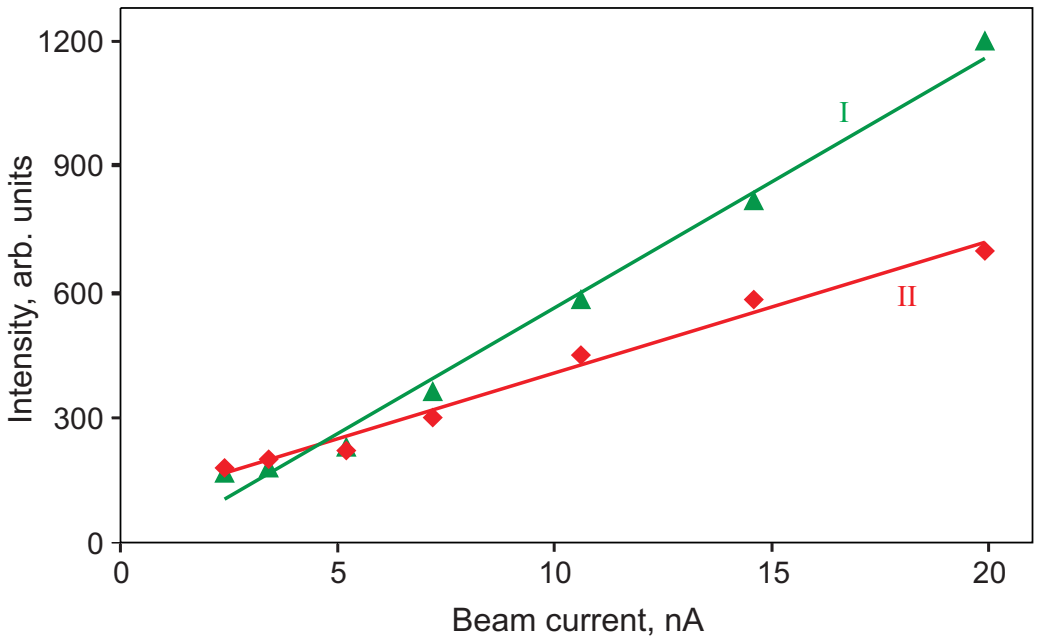

Figure 4.4: ***Intensity of emitted light as function of electron beam current.*** *Emission intensity for peaks I and II as a function of electron beam current for an acceleration voltage of 40 kV at an injection point ∼100 nm inside the wall of the well.*

well interacts with its 'mirror image', but this interaction is somewhat different in a dielectric section, as exemplified in Fig. 4.6. This creates a monochromatic dipole of frequency $\nu = v/a$, where v is the electron velocity and a is the period of the structure, moving at the electron velocity. The radiation efficiency depends on the strength of the mirror interaction and on the density of photonic states available in the well, and therefore on its geometry and material composition as well as the proximity of electrons to the wall. In a well of finite length L, the spectral width of the emission line $\Delta\nu$ is governed by the uncertainty relation $L \times \Delta\nu \simeq v$. So for example, with 30 keV electrons ($v \simeq c/3$) and a well length $L = 2.2\ \mu m$ (eleven 200 nm layers) one may expect an emission line with a width of ∼220 nm centered at ∼1200 nm, not far from what is observed in the experiment. In reality, this naïve picture is complicated by relativistic corrections, the excitation and scattering of surface plasmons on metal/dielectric interfaces within the structure, the light-guiding properties of the silica layers, and ultimately the guided-mode profile of the nano-tube (see Fig. 4.6). Nevertheless, the inverse proportionality it describes between emission wavelength and electron velocity is clearly seen in the blue-shifting of experimentally observed emission peaks with increasing electron energy (Fig. 4.3).

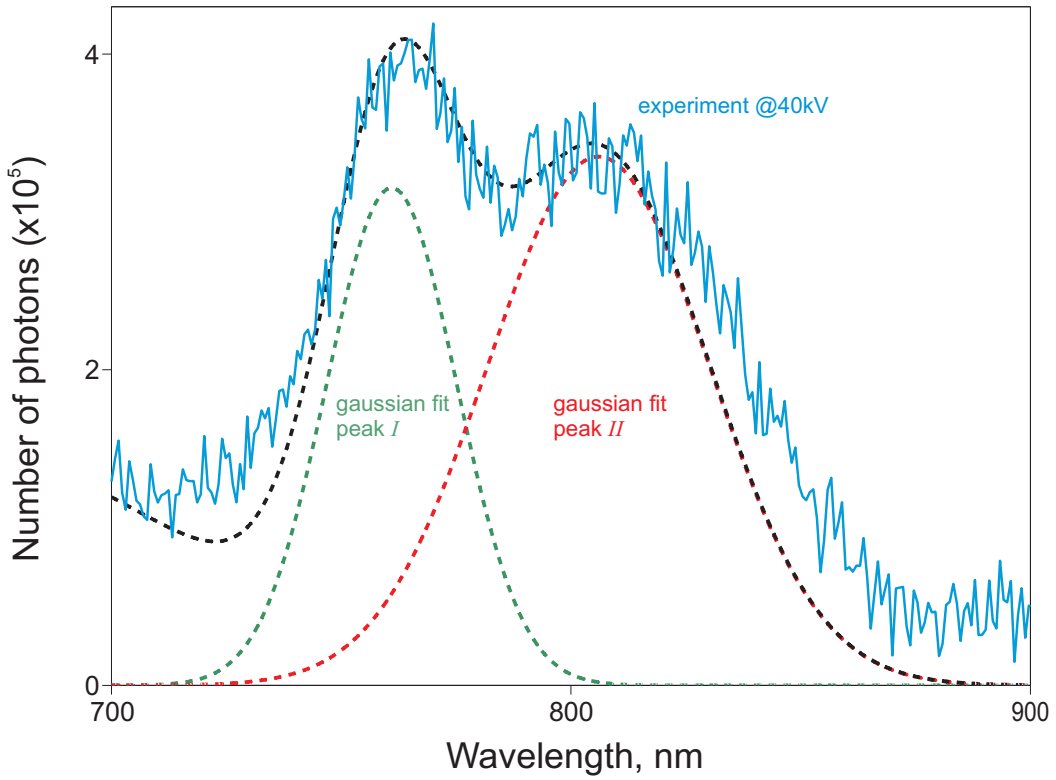

Figure 4.5: ***Gaussian fit of the light emission peaks.*** *Emitted light intensity at 40 keV, in number of photons per wavelength of emission (blue curve). The two emission peaks are fitted using gaussian functions (green and red dashed lines for peak I and peak II respectively). The total fit is shown as a black dashed line..*

For a well of ideal cylindrical symmetry the mirror interaction strength will be at a minimum for electrons traveling along the axis of the well and will increase with proximity to the wall, increasing the emission intensity as described above and illustrated (from experiment) in Fig. 4.7. Also plotted here is an analytical estimate of the corresponding relative emission probability [67], which is proportional to $(I_m(\nu R/v\gamma))^2$, where I_m is the modified Bessel function, γ is the Lorentz correction factor $(1-v^2/c^2)^{-1}$, and R is the radial distance of the beam injection point from the axis of the well [2]. The offset zero level seen in the experimental data can related to the imperfect cylindrical symmetry of the well: the real shape of the well will be slightly conical (typical of the FIB fabrication processes), thus introducing a constant contribution due to the impact of the free electrons with the well.

This basic emission process bears some similarity with the Smith-Purcell effect [75],

[2] The analytical expression can be derived following the formalism introduced in Chapter 2, applying it to cylindrical structures.

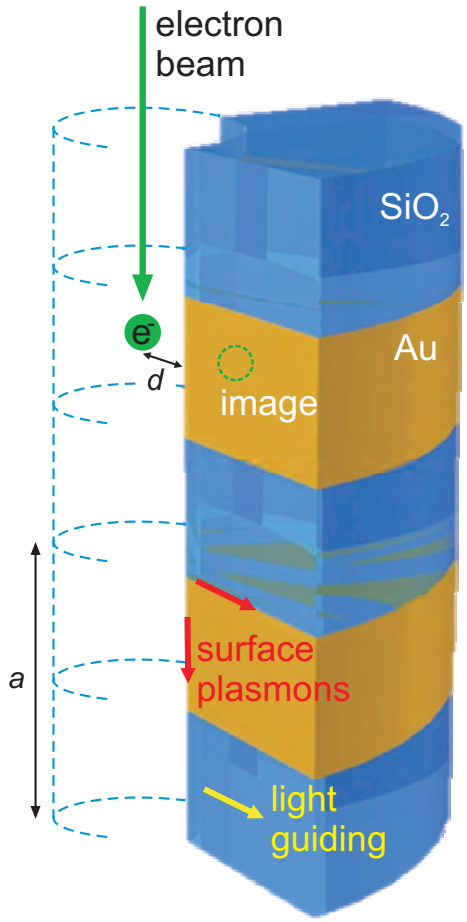

Figure 4.6: ***Dipole model of electrons inside the light well.*** *An electron passing through a metal section of the well interacts with its 'mirror image', but this interaction is different in a dielectric section. The layered structure of the well gives also rise to other phenomena such as surface plasmons launching at the metal/dielectric interface and light guiding within the SiO_2 layers.*

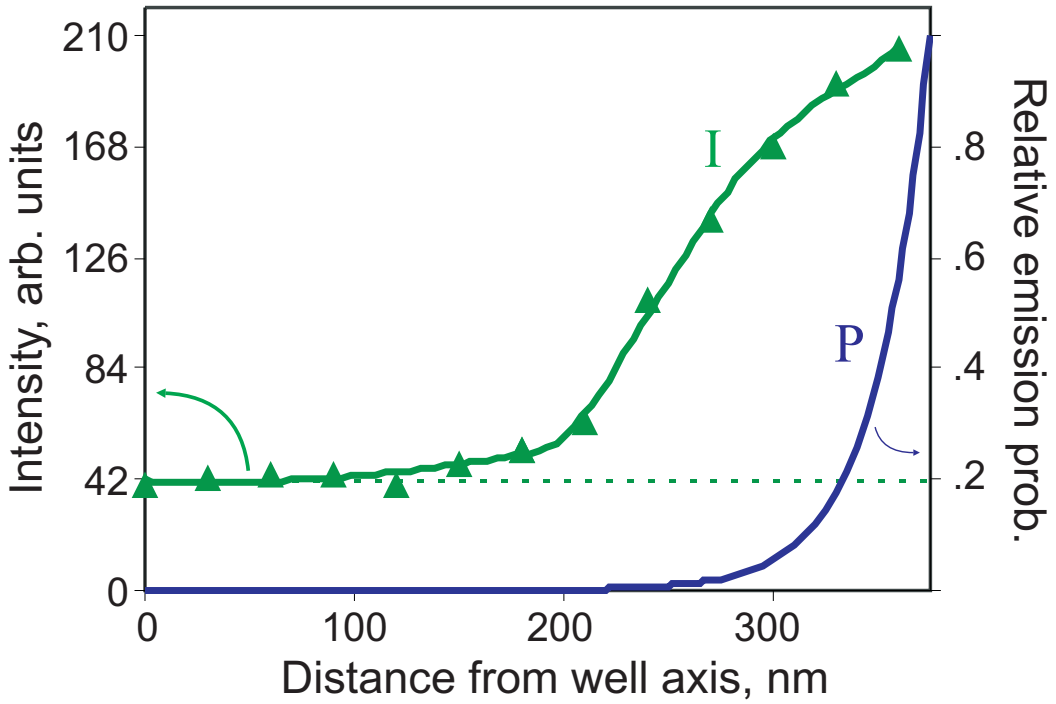

Figure 4.7: ***Intensity of emitted light as function of electron beam distance from the centre of the well.*** *Emission intensity of peak I (760 nm) at 40 kV and analytically estimated emission probability (P) as functions of beam injection position relative to the axis of a 750 nm diameter well.*

whereby a continuum of light wavelengths (varying with electron energy and the direction of emission) is generated as electrons pass over the surface of a planar metal grating. However, in the present case emission occurs via coupling to the 1D photonic bands of the periodically structured well so that discrete emission wavelengths are produced, determined by the condition that the wavevector of a guided mode is equal to ν/v. This fundamental consideration is analyzed in Fig. 4.8, which shows the dispersion diagram for the guided electromagnetic modes of a cylindrical gold cavity with a radius of 350 nm, folded over the first Brillouin zone (BZ) to account for a periodicity a of 400 nm in the direction parallel to the axis of the tube.

Modes with azimuthal numbers $m = 0$, 1 and 2 are shown alongside the free-space light line and lines associated with electron energies of 20, 30 and 40 keV. (For the same reason that periodic patterns of sub-wavelength holes in a planar metal surface do not substantially change its properties, even at high filling-factors, except very close to the BZ boundaries [117], the presence of silica inclusions in the wall of the experimentally studied cavity will not significantly alter the mode structure except around $q = 0$ and

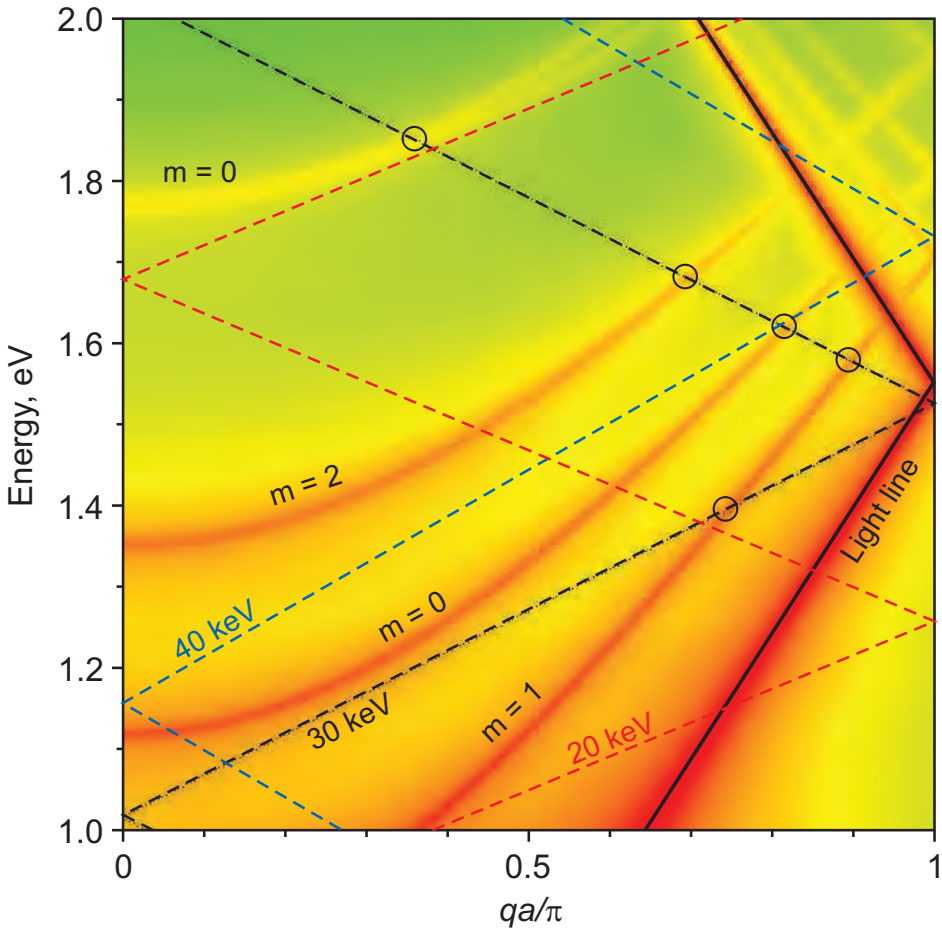

Figure 4.8: ***Dispersion diagram.*** *Dispersion diagram showing the guided modes of an infinite periodic cylindrical gold cavity with a radius of 350 nm (azimuthal numbers m = 0, 1 and 2), superimposed with the free-space light line (solid black) and lines associated with electron energies of 20, 30 and 40 keV (dashed lines). Points of intersection between the 30 keV line and the cavity modes are circled. The figure and the analysis behind it was produced by Prof. F. J. García de Abajo*

π/a where some distortion will occur.) Electrons can couple to cavity modes where their respective lines intersect. This plot illustrates that the accessible mode profile is a complex function of electron energy, but one can immediately see that an electron of a given energy can couple to a number of modes at different energies (wavelengths) and that a given intersection point will shift to higher energies (shorter wavelengths) with increasing acceleration voltage, as observed experimentally.

4.3.2 Numerical simulation

As discussed in the previous section, analytical approximations provide some insight into the light-well emission process: the inverse proportionality between electron en-

ergy and emission wavelength emerges from the basic assumption that electrons passing down the well form oscillating dipoles with their 'mirror images' in the wall; the increased emission probability for injection points closer to the wall can be expressed in terms of a modified Bessel function describing the strength of the electron-wall interaction; and the complexity of the well's guided photonic mode profile (multiple emission wavelengths for a given electron energy) is illustrated by the dispersion diagram for a periodic cylindrical cavity. However, a single analytical model cannot account for the complex interplay between material- and geometry-dependent emission mechanisms (dipole oscillation, surface plasmon excitation and scattering) and light-guiding characteristics (along the well axis and within the dielectric layers). Numerical methods provide an alternative approach to the interpretation of experimental results and to the design process for improved light-well structures.

The numerical method of choice in this case has been the Boundary Element Method (BEM), described in Section 2.5, which has been established as a powerful tool for the analysis of free-electron interactions with and the optical/plasmonic properties of nanostructures [83, 84]. In the particular case of the light-well, the layered structure incorporating optically transparent material presents a computational problem: despite the fact that the axially symmetric well can be defined by a two-dimensional cross-section, the number of points required to define these layers to a sufficient radial distance is prohibitive (to a first approximation, computational time scales as N^3, where N is the number of points). Thus, to allow for the impact of variations in individual structural and operational parameters to be studied, in what follows, a solid gold light-well with a corrugated internal profile (see Fig. 4.9a) is considered, as opposed to a smooth-walled gold-silica structure.

In the first instance, this model clearly reproduces the blue-shift in emission wavelength that is observed with increasing electron energy (Fig. 4.9b). Furthermore, in evaluating emission probability, the BEM also determines electron energy loss during propagation resulting from interaction with nearby structures. In the case of the light-well, as shown by the inset to Fig. 4.9b, such calculations reveal a clear correlation between peaks in the emission and electron energy loss spectra. The model also helps to evaluate what happens to electron induced light emission when the geometric parameters of the well are changed. For example, it is interesting to know how modifications

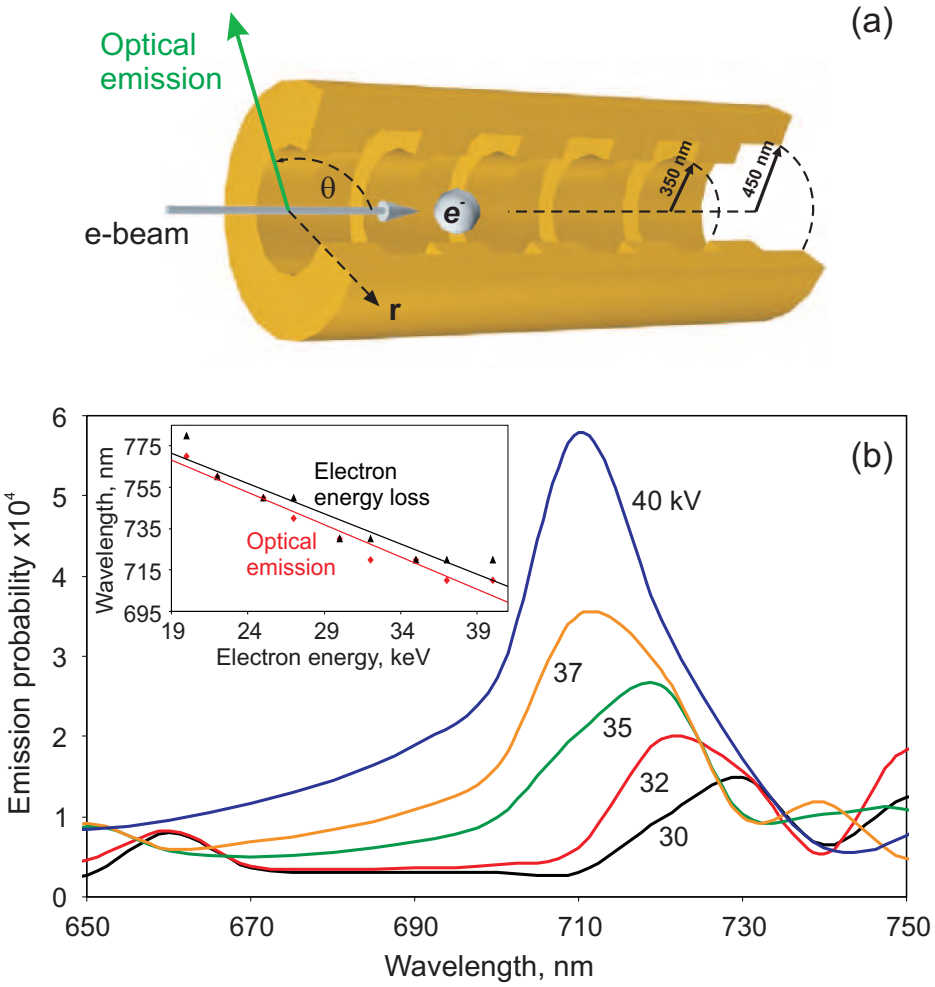

Figure 4.9: ***Emission wavelength shift in a gold corrugated nanotube.*** *(a) Light-well structure modeled using the boundary element method: a solid gold well with an internal rectangular grating profile of max./min. internal radius 450/350 nm and external radius 2350 nm; period = 400 nm; number of periods n = 6 unless otherwise stated. Emission zenith angle θ is measured relative to the direction of electron propagation: i.e. 0° = parallel, 180° = antiparallel. (b) Optical emission probability (photons per electron integrated over angles θ from 100 to 180°) as a function of emission wavelength for electrons with a range of energies (as labelled) injected at a radial distance r = 300 nm. The inset shows the spectral positions of emission probability and electron energy loss peaks as a function of incident electron energy.*

in the period or the radius of the well affects the emission features. The changes induced by a change in the period are shown in Fig. 4.10a: a clear blue shift in the emission wavelength is produced by a decrease in the period length; while this effect is expected due to the grounds the light-well emission process shares with the Smith-Purcell effect, it is certainly more surprising the damping in the emission probability. Changes in the radius of the well will also have effects on the light emission due to the modification of the modes supported by the new structures. This effect is illustrated by Fig. 4.10b: the reduction in well lateral size (diameter) induces both a blue shift in the wavelength of the emitted light and a decrease in the probability of emission. These effects seem to find confirmation in the experiments run with light-wells of either 200 nm period or radius smaller than 250 nm, for which no substantial light emission has been detected (blue shift and damping of the peaks has probably buried them in the broad cathodoluminescence peak for the glass).

A more detailed picture of the emission profile is provided by angle-resolved plots of emission probability such as those presented in Fig. 4.11. Here the peak shift with electron energy is seen once again and finer structure is revealed: for example at 20 keV, emission into the primary spectral peak at ∼775 nm is concentrated in the backward direction between θ ∼160-180°, while longer wavelengths emerge at shallower angles. It is anticipated that changes in angular emission profile, which may be measured in future experimental studies, will be associated with transitions between emission modes accessed under different pumping regimes.

Further to this, the BEM can generate maps of electromagnetic field intensity in and around the well structure, as shown in Fig. 4.12. It is interesting to note here that the field distribution corresponds to a guided cavity mode (to a first approximation it is cylindrically symmetric about the cavity axis) that is essentially independent of the radial electron injection coordinate r but strongly influenced by reflections at the two ends of the well (demonstrated by the axial intensity profile).

The uncertainty relation associated with the basic idea of emission via the creation of an oscillating dipole inside the well ($L.\Delta\nu \sim v$, where ν is emission frequency and v is electron velocity [96]) indicates that emission line-width will decrease with increasing well length L. This behavior is elegantly demonstrated by the boundary element model: Fig. 4.13 shows the evolution of the emission peak highlighted in Fig. 4.9b (where the

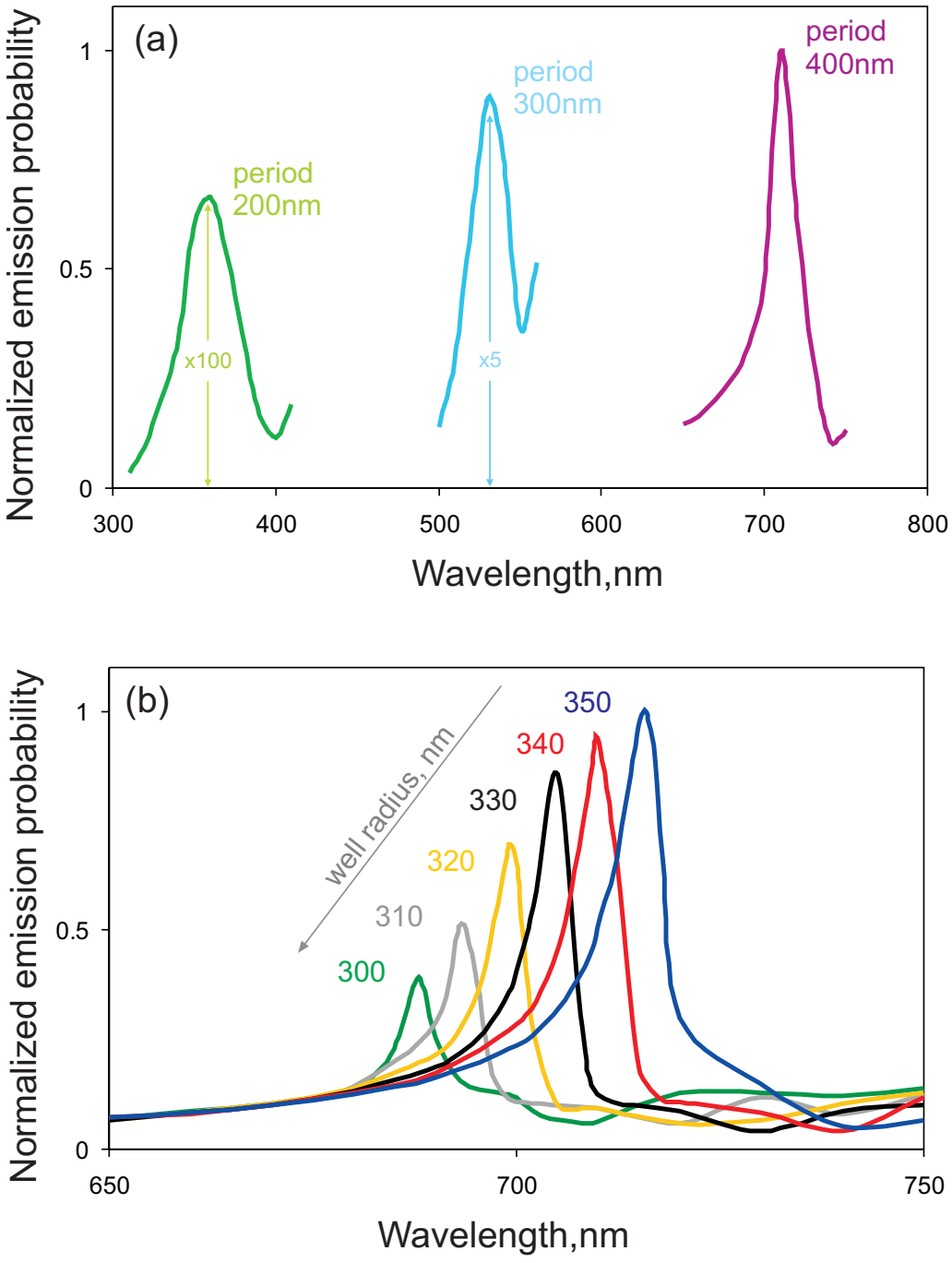

Figure 4.10: ***Effect of period and radius on light-well emission features.*** *EIRE probability and spectral position change of the main emission peak, for (a) wells with period of 400 nm, 300 nm and 200 nm [spectra are normalised to the peak for the 400 nm period well]. (b) Wells with radius ranging between 350 nm and 300 nm [spectra are normalised to the peak for the 350 nm radius well], when 40 keV electrons are injected into the well geometry defined in Fig. 4.9a at r=300 nm*

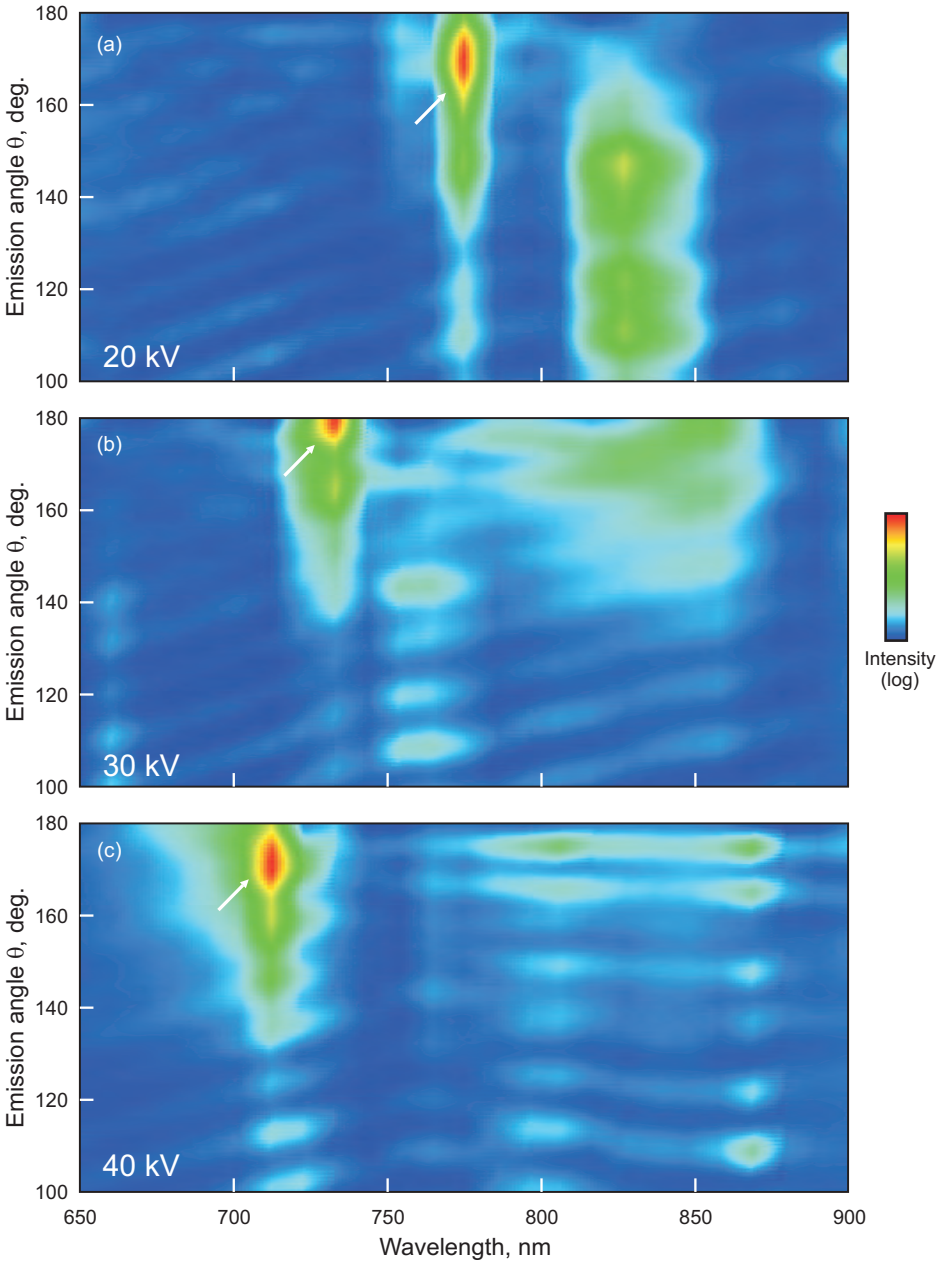

Figure 4.11: ***Angular emission in a gold corrugated nanotube.*** *Emission probability as a function of wavelength and emission angle θ (as defined in Fig. 4.9a) for 20, 30 and 40 keV electrons injected into the well geometry defined in Fig. 4.9a at $r = 300$ nm. [(a), (b) and (c) are separately normalized; the maxima in (b) and (c) being respectively 2.4 and 6.8 times the maximum in (a)].*

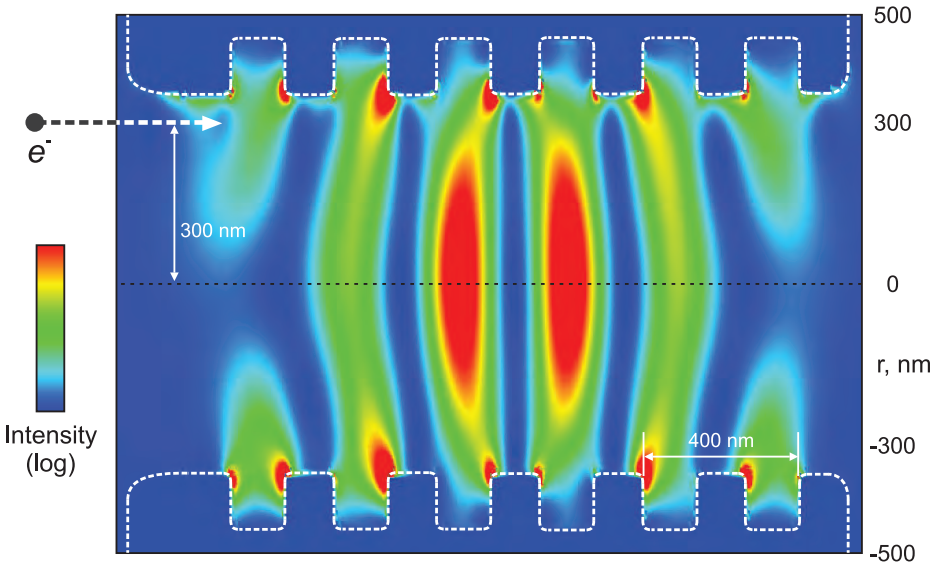

Figure 4.12: ***Field intensity inside a gold corrugated nanotube.*** *Cross-section showing the intensity $|E|^2$ of the electric field inside the light well, calculated at the peak emission wavelength of 716 nm for a 40 keV electron injected (from the left) at r = 300 nm.*

number of periods $n = 6$, i.e. $L = 2.4$ $/mu$m) with well length.

The development of a cavity mode near the centre of the structure, as suggested in Fig. 4.12 and the emission intensity increase and narrowing by well length, as suggested in Fig. 4.13, invites to look more deeply into how the length of the well actually affects light emission. Building on the basic idea, illustrated just above, of emission via the creation of oscillating dipoles along the well, the description can be extended considering the effect of the cavity imposed on the oscillating dipole, leading to a Fabry-Perot like process taking place inside the cavity of the well. If that is to be the case, then it is to be expected that different well lengths will give highest emission at different wavelengths. Indeed, BEM returns results along this line, as illustrated in Fig.4.14, in particular it can be seen that: i) for three different wavelengths, 704 nm, 710 nm and 716 nm, the maximum of light emission is obtained for wells of different lengths (expressed in number of periods in the figure) and ii) a well of a specific length has different emission strength at relatively close wavelengths. The insets show how the mode created in the centre of the light well is underdeveloped for a specific well length off-resonance (n =6, λ=710 nm) with respect to the on-resonance cases.

Fig. 4.15 shows the numerically modeled dependence of emission probability on the radial position of the electron injection point alongside the experimental dependence

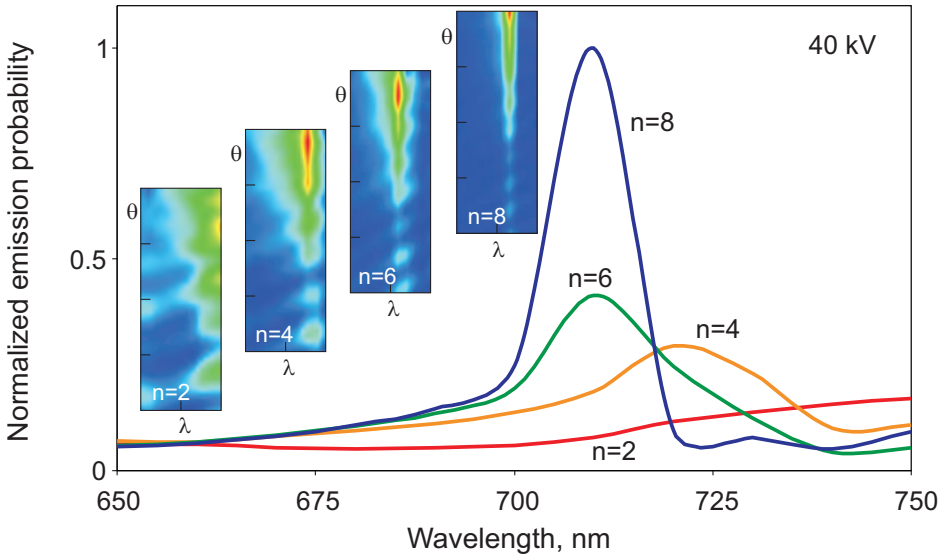

Figure 4.13: ***Emission narrowing with well length.*** *Integrated emission probability (θ = 100 - 180°) as a function of wavelength for 40 keV electrons injected at a radius of 300 nm into wells of varying length, indicated by the number of periods n (as labelled). The insets show the emission probability as function of wavelength λ from 650 to 750 nm and emission angle θ from 100 to 180° for each of the four cases.*

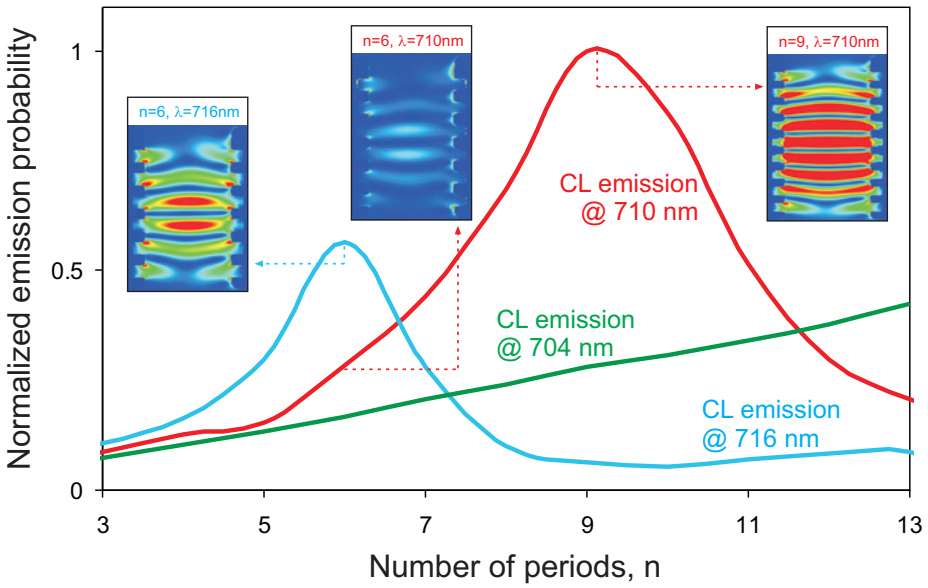

Figure 4.14: ***Effect of well length on the wavelength of the emitted light.*** *Integrated emission probability (θ = 100 - 180°) as a function of well length, indicated by the number of periods n, for 40 keV electrons injected at a radius of 300 nm into the wells for three distinct wavelengths, clearly showing peaks at different ns. Emission at 704 nm shows increase in emission and peaks outside the computationally available range. Insets: cross-sections showing the intensity $|E|^2$ of the electric field inside the light well at significant values of n, all plotted for the same emission maximum.*

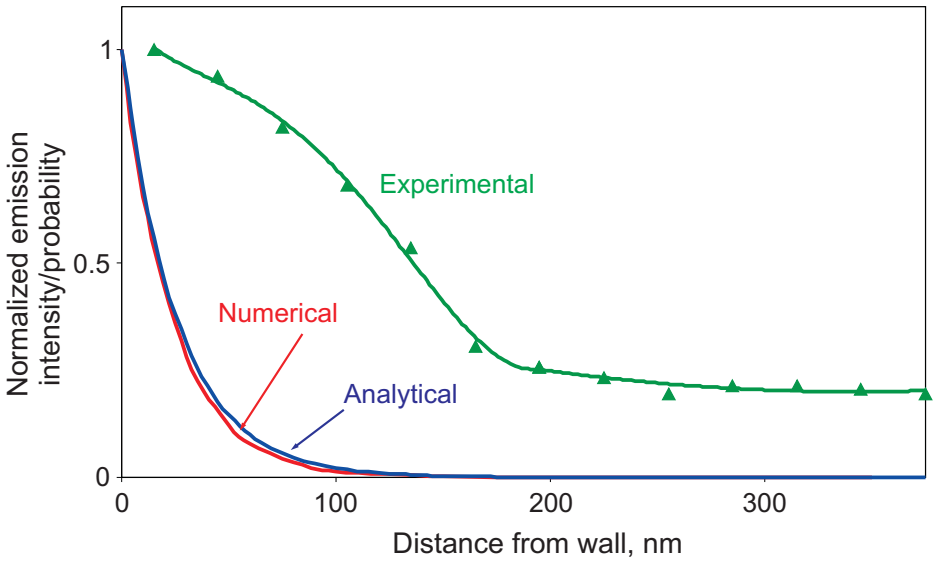

Figure 4.15: ***Emission intensity vs distance from well centre.*** *BEM integrated emission probability (n = 6, red) as a function of the distance between electron injection point and the wall of the well alongside the experimentally measured 760 nm emission intensity (Peak I in Fig. 4.3c, green) and the analytically estimated emission probability (blue) for 40 keV electrons.*

and analytical approximation presented in Ref. [96]. The BEM model matches the modified Bessel function approximation very well, with both predicting a rapid decay to zero emission for injection points more than ∼100 nm from the wall of the well. In comparing these to the experimental result, which decays less rapidly and maintains a background emission level even at large distances, it should be noted that neither model accounts for the true electron beam diameter, or the fact that in experiment the electrons must ultimately collide with the sample (producing transition radiation even for axial trajectories).

4.4 Conclusions

To summarize, it was provided the first proof-of-concept demonstration of a tuneable, electron-beam-driven, nanoscale radiation source in which light is generated as free electrons travel down a 'light-well' - a nano-hole through a stack of alternating metal and dielectric layers. Incoherent near-infrared emission is demonstrated in the present case but it is believed that the concept may readily be scaled at least from the THz range to the UV domain by varying the periodicity of the structure (the Smith-Purcell

mechanism has been experimentally demonstrated over this range [118,119]; constraints on electron beam quality approaching the Heisenberg uncertainty limit would seem to preclude extension to shorter x-ray wavelengths [120]). Moreover, a detailed numerical description of the processes involved in light generation have been modeled using the boundary element method (BEM). The examples presented here show that (BEM) modeling can not only reproduce all of the key characteristics observed experimentally in light-well emission but also provide insight for future designs. For example, it is confirmed that longer wells will produce narrower emission lines, but also made clear that scaling of the emission towards shorter wavelengths has to go through an accurate analysis of geometrical features.

Furthermore, it can be anticipated that optimization of the light-well geometry, material composition and pumping regime will substantially improve emission efficiency. Indeed, if losses can be controlled (for example, by inhibiting surface plasmon generation and transverse light-guiding) and higher (perhaps pulsed) drive currents are employed, it may be possible to achieve coherent, superradiant or even lasing emission modes [121–124].

The simplicity and nanoscale dimensions of the light-well geometry make it a potentially important device for future integrated nanophotonic circuit, optical memory and display applications where it may be driven by the kinds of microscopic electron sources already developed for ultrahigh-frequency nanoelectronics and next-generation flat-panel displays [112].

5

Electron beam driven nanoscale metamaterial light sources

Planar photonic metamaterials can act as nanoscale, free-electron-driven light sources: emission occurs at wavelengths determined by the structural geometry of the metamaterial. The free-electrons excitation of the metamaterial excites a resonant effect through metamolecular interaction, leading to coherent light emission. The collective emission mediated by inter-metamolecularinteraction and the linewidth narrowing of the emitted indicate that some of the mechanisms behind the lasing spaser action are taking place.

5.1 Introduction

The recent explosion of interest in the fields of nanophotonics, plasmonics and metamaterials has brought a pursuit of nanoscale light and plasmon sources driven by optical [15,16,27,48], current [25,125] and free electron [10,58,63,64,67,75,83,96,97,99,126] excitations. Here it is demonstrated experimentally and theoretically a fundamentally new phenomenon of conversion of the energy of free electrons into a spatially coherent light emission. It is shown that the injection of free electrons into a nanoscale structure of planar photonic metamaterial leads to a resonant effect of synchronized excitations of currents in the array of plasmonic resonators, fueling the emission of spatially coherent plane wave in the visible part of the spectrum.

In this chapter, the experimental data and the numerical characterization of the phenomenon are reported and analysed. Section 5.2 provides a description of the mechanisms responsible for the collective light emission. In Section 5.3 the fabrication process and the optical characterisation of the sample are described. In Section 5.4 the contribution to EIRE spectra from asymmetrically split rings (ASRs) are shown and their connection with optical spectra is highlighted. Section 5.5 investigates the features of the emitted light, and its dependence on the number of unit cells involved in the emission process, while Section 5.6 discusses the emission directivity of the metamaterial light source. Section 5.7 then provides the numerical simulations support to the experimental data, discussing the intensity and phase characteristics of the emitted light at ON and OFF metamaterial's resonance frequencies.

5.2 "New" light emission from metamaterials

Conceptually, the new type of spatially coherent light emitter phenomenon is explained on Fig. 5.1: in certain types of metamaterials a *localized* excitation[1] of the array leads to the formation of synchronized, in-phase response of a large number of meta-molecules. Electromagnetic and plasmonic fields mediate strong interactions between the meta-molecules, so that a metamaterial system exhibits *collective* modes of current oscillation. Driving plasmonic oscillations of a few metamolecules of the array at the resonance

[1]Here, the term localized indicates that the excitation area is smaller than or comparable to a single meta-molecule.

frequency that is formed by strong interaction between the metamolecules leads to a broad area of the array oscillating in phase.

The decomposition of the excitation into the collective eigenmodes of the finite array M_{ij} shows that most of energy is stored in the mode M_{11}, consisting of a phase-coherent uniform excitation of magnetic dipoles, with other modes being only weakly excited (details of the model may be found in [127] and [128]). Coherence is lost for excitation away from the resonance frequency, as illustrated in section 5.7. Oscillations of mode M_{11} with a uniform phase profile are of particular interest as they will create a diffraction limited plane wave propagating perpendicular to the metamaterial array.

Furthermore, the absorption and thus emission spectrum of the collective mode exhibit a spectral collapse with increasing size of the array [49, 128]. It is argued that localized injection of electrons into the metamaterial array could drive an excitation in a single meta-molecule that through interactions between the metamolecules will spread into a collective mode of excitation. This mode can be efficiently excited by the evanescent field of a free electron injected into the meta-molecule perpendicular to the array. After the initial stimulation of the entire mode structure that follows the electron injection, the collective mode M_{11} with most suppressed radiative emission rates will becomes the dominant one

It is believed that the experiments with focused electron beam exciting a planar plasmonic metamaterial show all the main features of this phenomenon.

5.3 Sample fabrication and optical characterization

The experiments were performed with planar metamaterial arrays of ASR meta-molecules carved onto a 50 nm gold films supported on a 100nm silicon nitride membrane, as presented in Fig. 5.2[2].

The ASRs were milled through the gold layer using focused ion beam milling. Five metamaterial arrays were fabricated, located on the same membrane, each of approximately $20\mu m \times 20\mu m$ in size. All metamaterial samples had the same pattern (ASRs), but progressively changing unit call size from 220nm to 280nm. After focused ion beam

[2]The samples used for the data reported in this chapter were fabricated by Mr. J. Y. Ou here at the ORC, University of Southampton, while Dr. F. De Angelis and Prof. E. Di Fabrizio, from the Italian Institute of Technology, fabricated the first samples on which the light emission was first observed and early characterization were performed

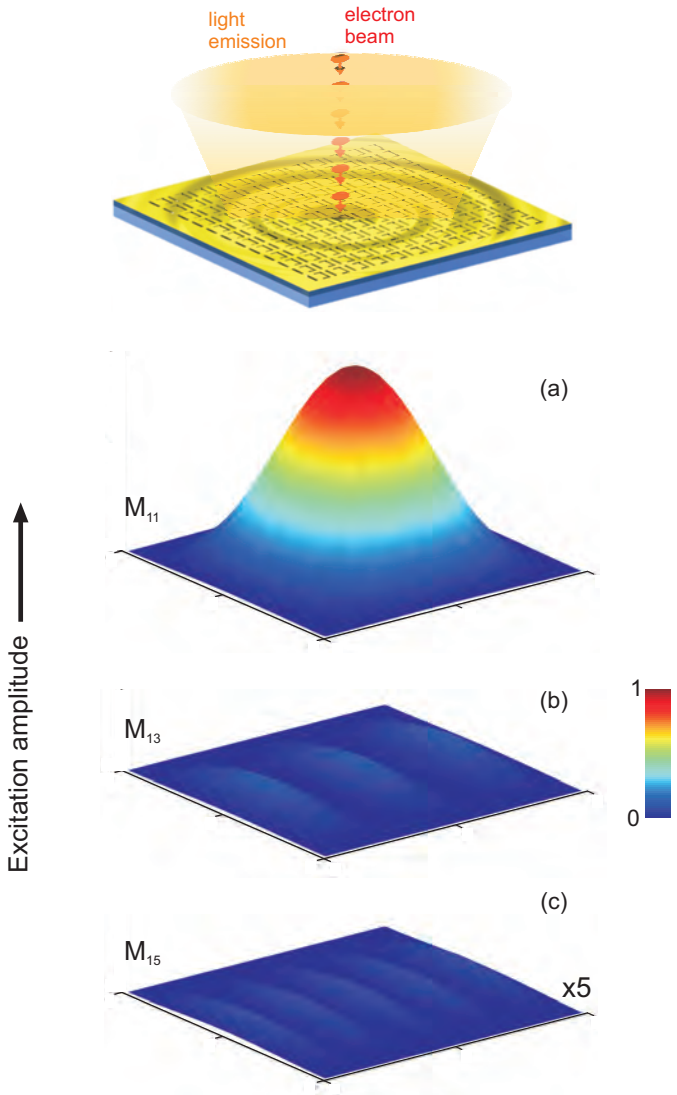

Figure 5.1: ***Modes of an ASR metamaterial*** *Response of metamaterial array to excitation at the center. Driving at the resonance frequency that is formed by strong interaction between the metamolecules leads to a broad area of the array oscillating in phase: the decomposition of the excitation into the collective eigenmodes of the finite array M_{ij} shows that 85% of energy is stored in mode M_{11}. Other modes (M_{13}, M_{31}, M_{15} etc. are weakly excited. Coherence is lost for excitation away from the resonance frequency.*

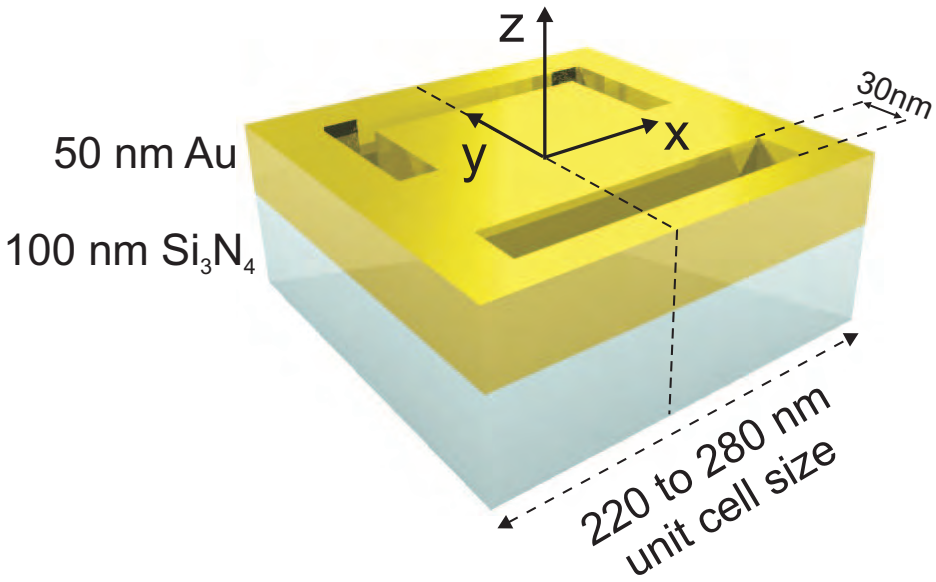

Figure 5.2: ***Metamaterial's unit cell*** *Schematic of the metamaterial's unit cell showing the materials' thickness, the ASRs linewidth and indicating the cartesian coordinate system used when referring to light polarizations.*

milling, the samples underwent a Rapid Thermal Annealing (RTA) process: they were baked for 1 minute at 350 °C. The RTA treatment resulted in a dramatic enhancement of the quality of the optical resonances shown by all the five metamaterial arrays along with a slight blue shift of the same. This effects are clearly visible in Fig 5.3, where the optical transmission spectra before and after RTA are reported. The spectra show enhancements going from about x18 for the 220 nm unit cell to about x5 for the 280 nm unit cell; at the same time a shift of ∼15 nm for the 220 nm unit cell and ∼40 nm for the 280 nm one are readily identifiable.

Transmission $T(\lambda)$ and reflection $R(\lambda)$ spectra of all the sample were measured in a microspectrometer which allowed the calculation of their absorption spectra $A(\lambda) = 1 - T(\lambda) - R(\lambda)$. The optical spectra were acquired using light with polarization either parallel (Y-polarization) or perpendicular (X-polarization) to the gap of the ASR, as shown in the inset of Fig. 5.4 . In Fig. 5.4 are shown the transmission and absorption spectra of the metamaterials (two unit cell sizes) for both polarizations[3]. Absorption peaks in particular are significant because they indicate the wavelengths at which the electromagnetic energy is "trapped" in the array due to the structuring of the metal and thus giving time to the various metamolecules to interact with each other and give

[3]Reflection spectra are omitted to allow a better visualisation of the absorption features. Similarly, only the spectra for two unit cell sizes are shown to make the figure easily readable.

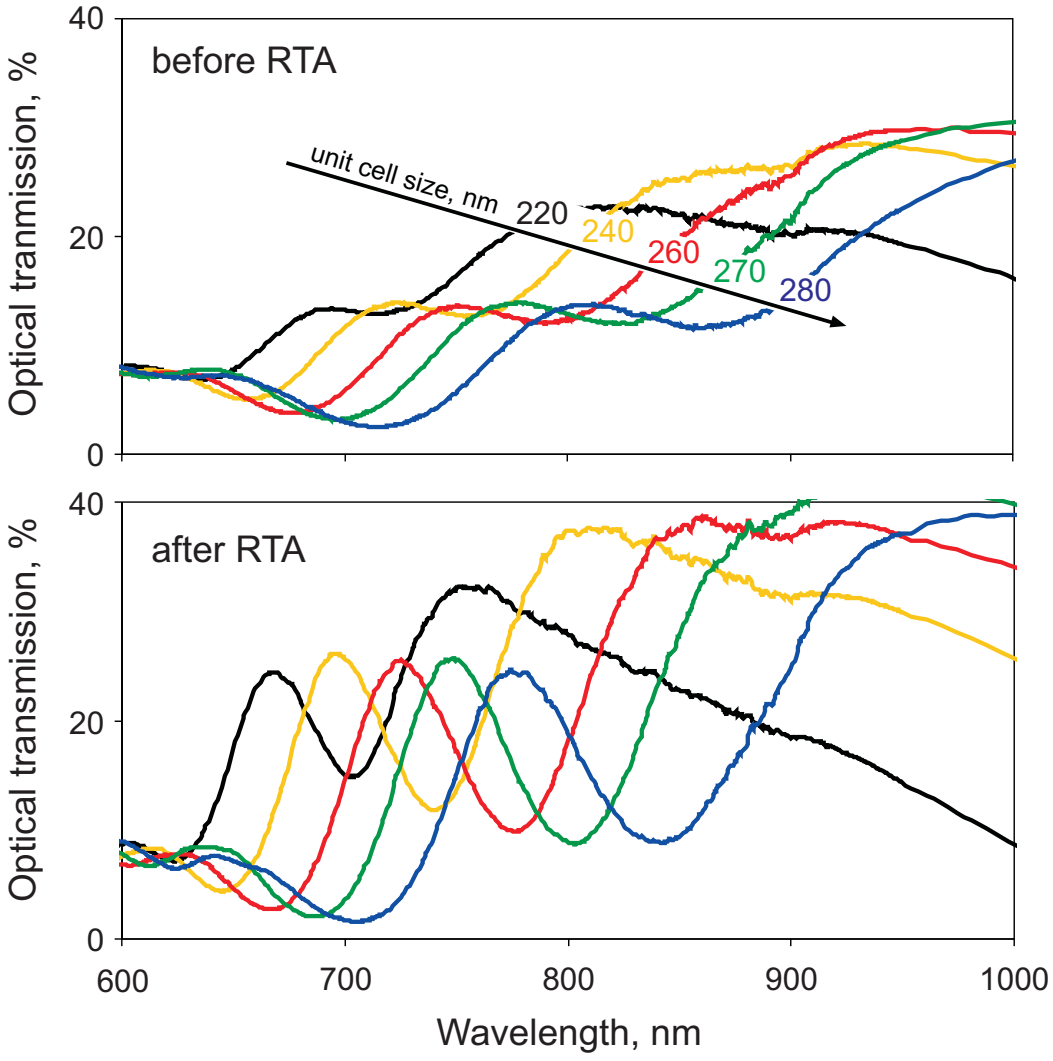

Figure 5.3: ***Effect of Rapid Thermal Annealing on resonances quality*** *Enhancement of the quality of the resonances, for all the five unit cell sizes, in the optical transmission spectra for y-polarized light, following RTA process on the sample.*

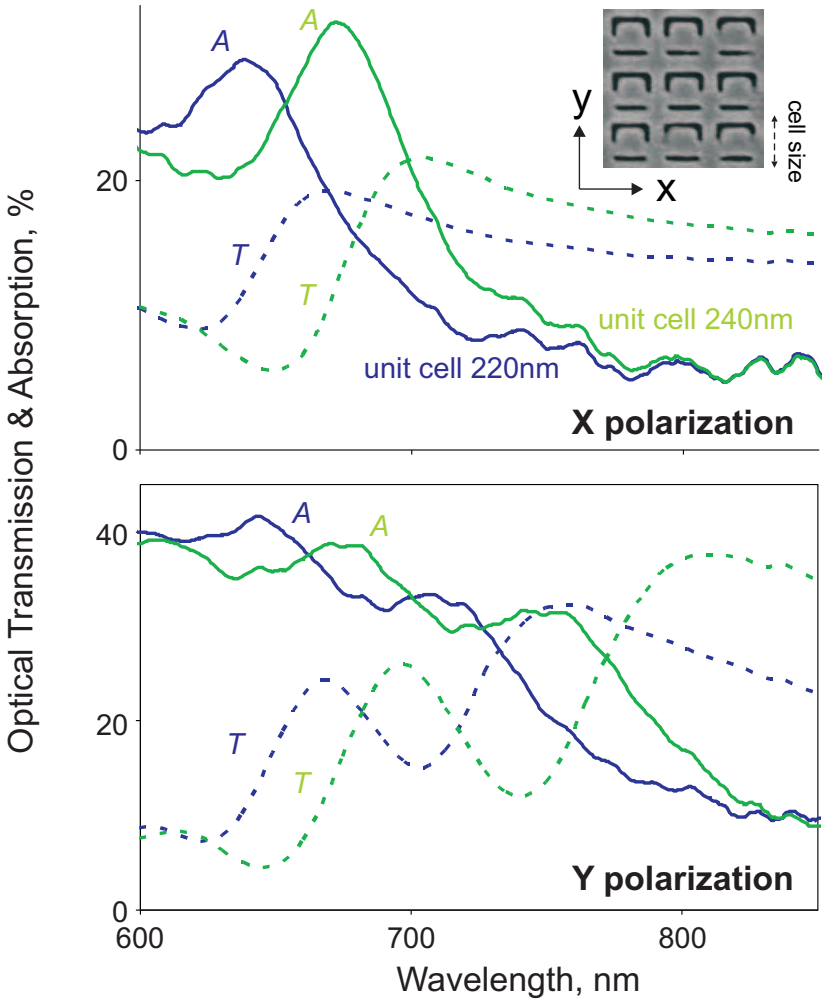

Figure 5.4: ***Optical transmission and absorption of metamaterial*** *Optical absorption and transmission spectra of two metamaterial samples for X- and Y-polarized light. The absorption peak for Y-polarization at short wavelengths coincides with the absorption peak for X-polarization.*

rise to interesting phenomena, as presented on Fig. 5.6.

5.4 EIRE emission and tuneability by geometry

The emission characteristics of electron-pumped metamaterial samples were studied within a scanning electron microscope (SEM) equipped with a collection achromatic reflective optics that directs optical emission from the vicinity of the electron injection point to a spectrometer with a liquid nitrogen-cooled CCD array detector, as described in section 2.4.1. The e-beam hotspot was set at 200 nm in diameter. Electron beam induced light emission spectra were recorded at beam current of about 50nA and were

averaged over groups of ten spectra taken with 2s intervals. In order to isolate the contribution from the metamatarial array, the spectra were compared with those originating from unstructured gold, as illustrated in Fig. 5.5.

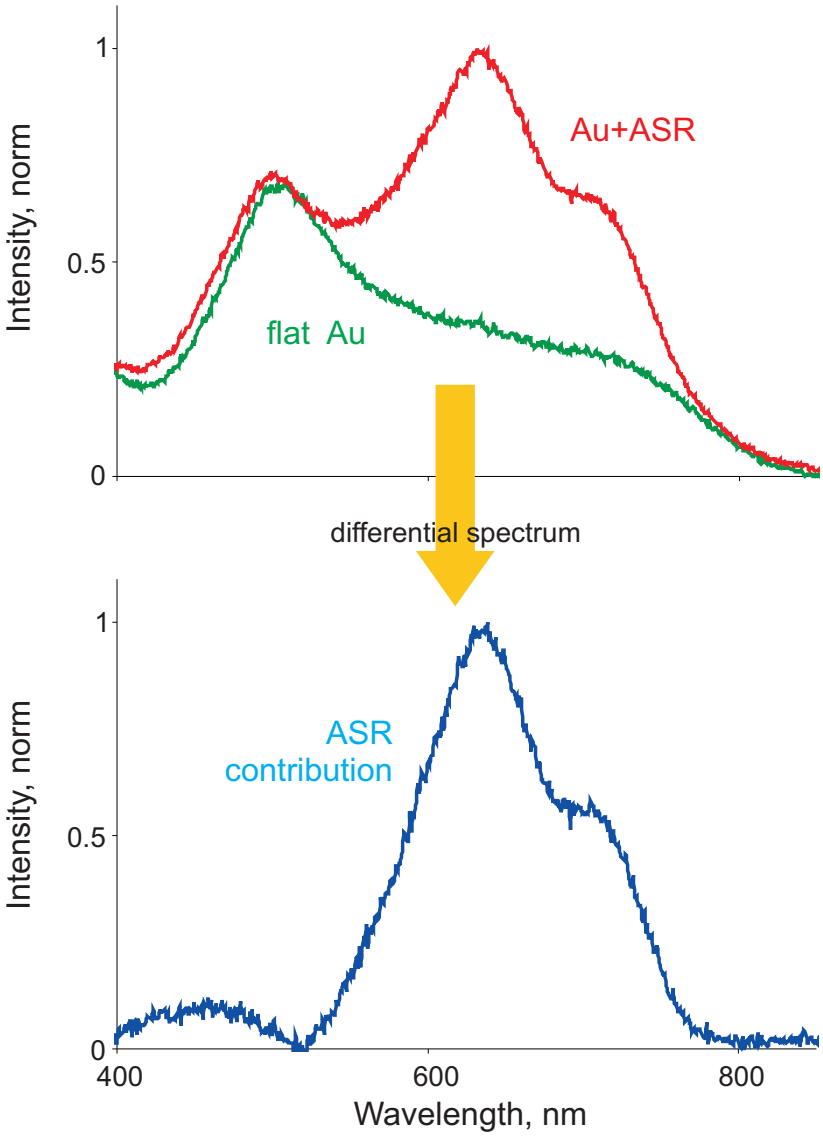

Figure 5.5: ***EIRE emission of ASR vs Au*** *Procedure to isolate the contribution of the ASRs to the EIRE. Emissions from ASR array and flat Au are recorded and then the latter is subtracted from the former. .*

All the spectra presented at Fig. 5.6a are differential spectra with background d-band fluorescence of unstructured gold film removed. Metamaterial's emission was easy to observe providing the opportunity to study the effect at different regimes. The first characteristic feature of the emission spectra was the correlation of the emission peak spectral position with the position of the metamaterial's absorbtion line, as seen in all

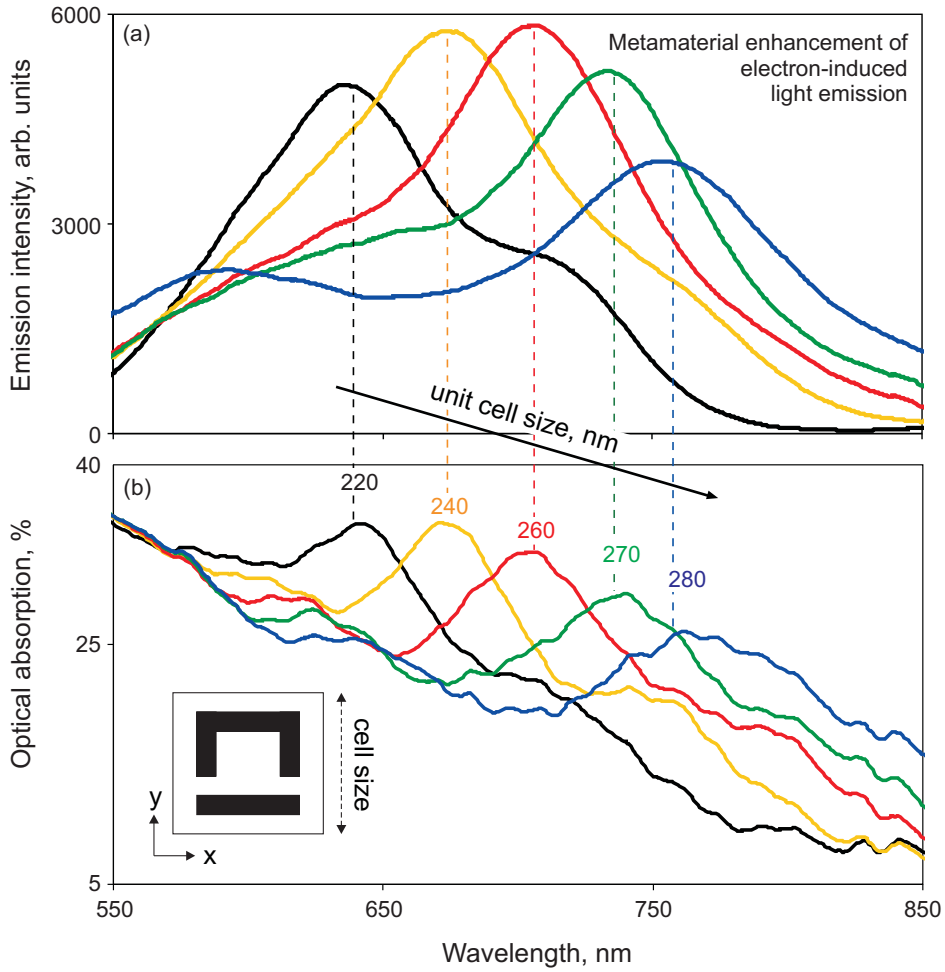

Figure 5.6: ***Tuneable emission*** *Electron-beam induced emission of light from a plasmonics metamaterial: Emission spectra in metamaterials with different unit cell size (a) and corresponding optical absorption spectra (b).*

five samples with different unit cell size (Fig. 5.6). This allows a clear association of the emission peak with the excitation of the collective plasmonic mode of the metamaterial.

5.5 Emission enhancement and linewidth narrowing by size effects

To study the dependence of the emission spectra on the number of excited molecules, the experiment was performed by changing position of the electron injection point, starting from the injection point outside of the array and moving it towards the center of the array. Results of this experiment for the metamaterial sample with unit cell of 220nm are presented on Fig. 5.7. At large distances from the array there is no

detectable influence of the metamaterial structure on the light emission (spectrum A in Fig. 5.7). Metamaterial's influence is seen from about $\sim$1.8 μm from the array. With further progression towards the center of the array overall intensity of the emission increases and its spectrum changes. If the injection point if firmly within the ray, at distance more than 8 unit cells from the edge of the array, no noticeable dependence of the spectrum and emission intensity is seen on repositioning the injection point.

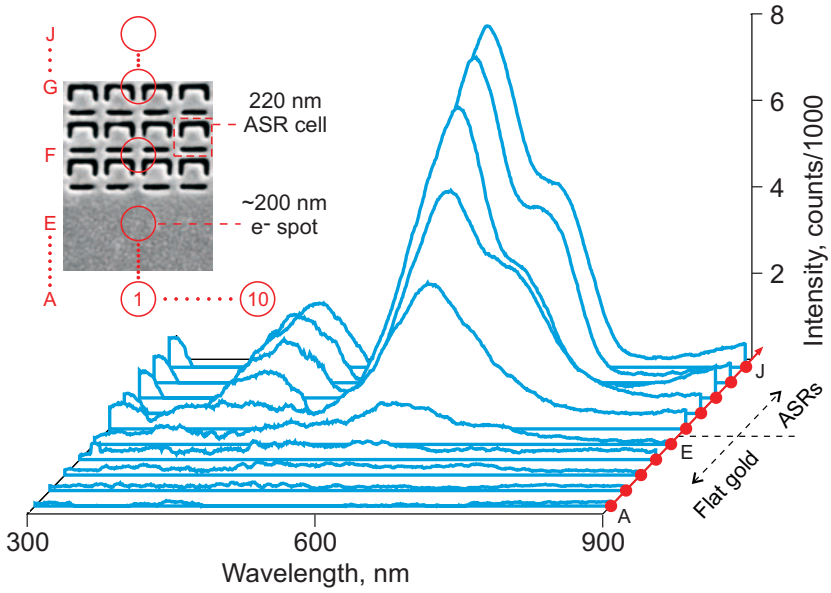

Figure 5.7: ***Position dependent emission*** *Electron-induced metamaterial light emission spectra as a function of beam injection point position relative to the boundary of the ASR array.*

It is instructive to plot the variation of spectra of emission as a function of position of the injection point. Furthermore, the electron injection point position is also converted into the number N of the meta-molecules of the array located within a radius of r $\sim$1.8 μm from the excitation point. The correspondence between the electron injection position and the number of metamolecules is illustrated in Fig. 5.8: the area of the overlapping region between a circle of radius r $\sim$1.8 μm centred around the electron injection position and the metamaterial array can be readily calculated; the ratio between the overlap area and the unit cell area gives the approximate number of excited metamolecules.

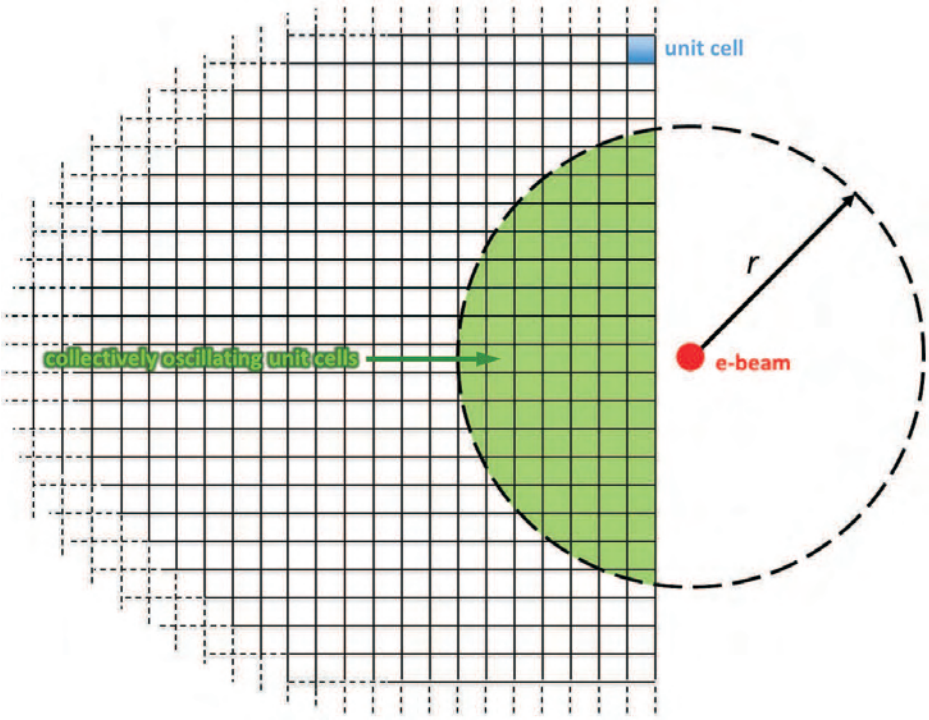

Figure 5.8: ***Evaluation of the number of excited metamolecules*** *The number of metamolecules that collectively oscillate is calculated by overlapping a circle of radius $r \sim 1.8\ \mu m$ and centre in the electron injection position with the metamaterial array. The metamolecules falling within the green shaded section of the circle are excited.*

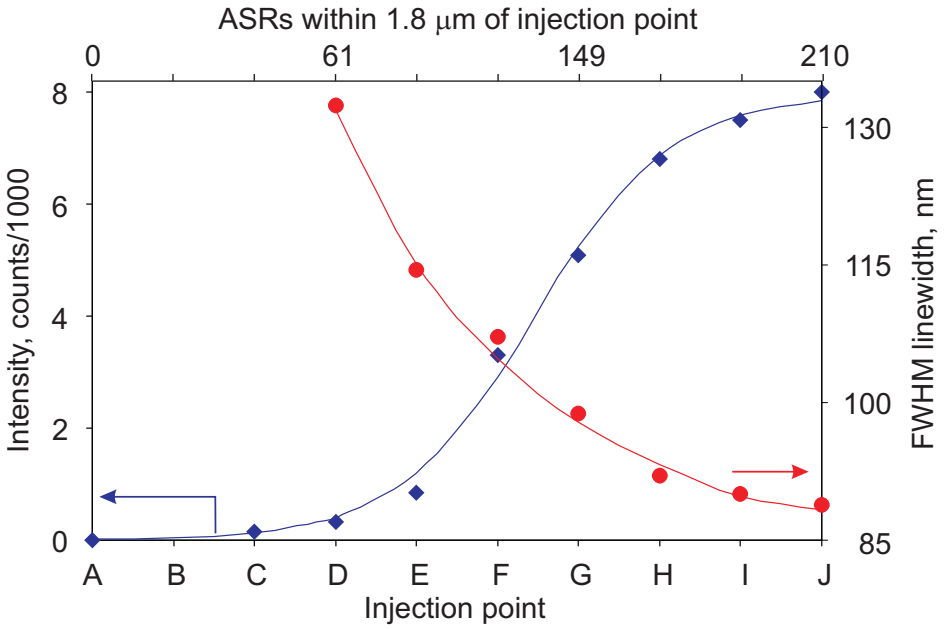

Figure 5.9: ***Intensity and linewidth dependence*** *Emission intensity and peak linewidth at 640 nm as function of the injection point position (bottom horizontal axis) and number of ASRs within a radius r ∼1.8 μm from the excitation point (top horizontal axis).*

The behaviour of emission spectra as function of both injection position and number of metamolecules involved is plotted in Fig. 5.9.

To facilitate the analysis the observed spectra are decomposed into two different Gaussian peaks, as illustrated on Fig. 5.10: as the injection point moves towards the center of the array and the number of meta-molecules within the ring of radius r increases a marked increase of intensity and decrease in the linewidth of the main emission peak at 640 nm can be observed (Fig. 5.9).

These results illustrate the collective and coherent nature of the light emission, which is directly analogous to the absorption resonance linewidth collapse, observed with an increasing number of resonators in microwave, terahertz and optical frequency coherent ASR metamaterials [49] and theoretically analyzed in [128]. Indeed, the dependence of the resonance quality factor Q on the number of unit cells N, found in [49], can in the present case be translated directly to the dependence of the linewidth of the emitted light on the number of unit cells, which shows a remarkable agreement with the experimental data (red curve in Fig. 5.9), thus confirming further the analogy suggested above. The collective excitation of an ensemble of meta-molecules is mediated by strong electromagnetic interactions between the meta-molecules and the surface

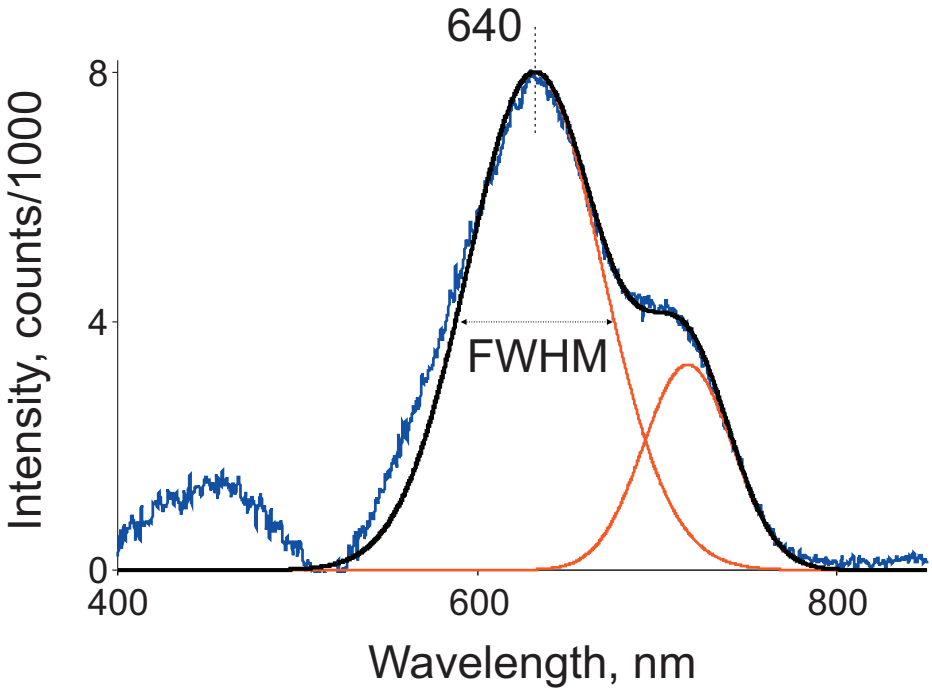

Figure 5.10: ***Gaussian fit of the emitted light*** *The main emission peak is fitted using two gaussian spectra. The main peak (640 nm) is selected for the analysis of intensity and linewidth of the emitted light.*

plasmons, generated by the free electrons impinging on the sample.

5.6 Directivity of the emitted light

If the light emission process described so far is to be coherent, confirmation should come from the analysis of its emission pattern. An experimental setup, allowing to check the spatial intensity distribution of the emitted light was thus built and its schematic is shown in Fig. 5.11a[4]. A liquid nitrogen cooled spectrometer's CCD was placed in the optical path just following the parabolic mirror and a 40 nm spectral filter. The beam stemming out from the parabolic mirror could then be directly imaged onto the CCD array. Due to the nature of the parabolic mirror, if the light source is placed exactly at the focus, it is possible to map each single pixel of the image recorded onto the CCD to a specific point of the mirror and, by trigonometric relations, to an azimuthal-polar coordinates pair, (ϕ, θ) with respect to the mirror focus. Details, along with angular maps, are presented in Appendix B.

[4]Dr. J.K. So helped setting up the directivity experiment

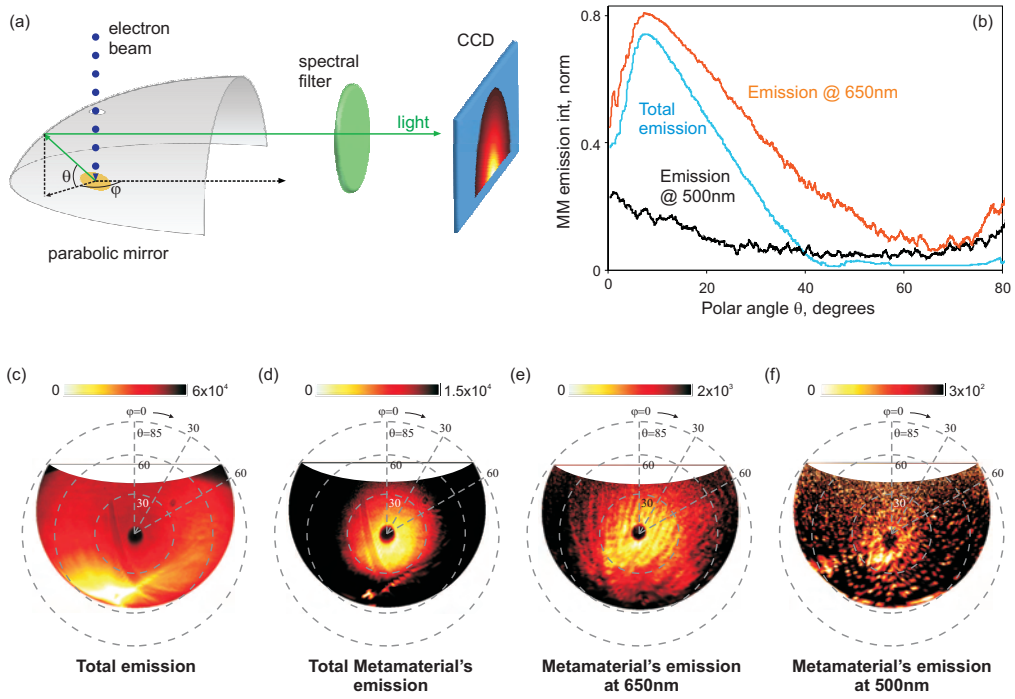

Figure 5.11: ***Directivity of the emitted light*** *(a) Experimental setup used for the evaluation of emission pattern: light emitted from the excited metamaterial is collected by the parabolic mirror, spectrally filtered and recorded onto a CCD array so that each single pixel is mapped into a unique position of the parabolic mirror and assigned to an azimuthal-polar (ϕ, θ) coordinates pair; (b) light emission intensity from metamaterial with resonance at 640 nm, once the emission from flat Au is removed, as function of polar angle ϕ, at 500 nm (black line), 650 nm (blue) and over the full spectral range [400-1100] nm (orange): emission concentrated within $\sim 30°$ around the normal ($\phi = 0$) is obtained at metamaterial resonance; (c-f) polar maps of the emission intensity from: (c) Au+metamaterial over the full spectral range and metamaterial only over the full spectral range (d), at 650 nm (e) and 500 nm (f): emission concentrated around the normal direction is clearly visible in (d) and (e) while is absent in (f).*

The light emitted from the metamaterial (220 nm unit cell) was characterised at three different spectral position: i) 650 nm, where the metamaterial emission was previously detected (see Fig. 5.5); ii) 500 nm, where the light emitted by flat gold and metamaterial were almost undistinguishable (see Fig. 5.5); iii) over the spectrometer's full spectral range (from 400 to 1100 nm). The intensity distribution of the light emitted by the metamaterial, as function of the polar angle θ, integrated over azimuthal angle ϕ, is shown in Fig. 5.11b for all the three cases (the curves are normalised to the total emission in each case). It can be readily seen that, at 550 nm, the emission directivity for metamaterial and gold is about the same (black curve) while, when the spectral window is opened (blue curve) or limited to the metamaterial resonance position (orange curve), a clear signature of the metamaterial appears. Moreover it can be appreciated how the emission from the metamaterial is concentrated around the direction normal to the metamaterial plane ($\phi = 0$) with a divergence of about 30°, hence suggesting a 'collimated' beam. The emission goes to zero at the normal as expected, due to the presence of the hole in the mirror to allow the passage of the free-electrons.

A visually more convincing picture is provided by the full angular maps showing both the azimuthal and polar angles. The maps are shown in Fig. 5.11c to f. Figures c to f show respectively, the total unfiltered emission (c) where the light appears evenly distributed across the whole map[5], the metamaterial's contribution to light emission in the unfiltered case (d) where a circular shape peaking at the centre is clearly distinguishable, the metamaterial's contribution to light emission ON-resonance, 650 nm, (e) where again the emission is concentrated around the centre, and finally the metamaterial's contribution to light emission OFF-resonance, 500 nm, (f) where a low and quite homogeneous distribution of light is detected.

The above discussion leads to the conclusion that the light generated by the matamaterial excited by free-electrons behaves more as a 'collimated' beam rather than an isotropic or dipolar emitter as in the case of respectively a point source or a dipole (as expected for example from flat gold irradiated by free-electrons). A more detailed discussion of the emission patterns detected for flat gold and metamaterial is given in Appendix B; here it is worth anticipating that the emission from the flat gold has a

[5]The bright spot at bottom of the map is present in all the 'as-recorded' maps and is believed to be due to small misalignments of the mirror, together with the fact that the back part of the mirror is the one that suffers of the highest aberration

toroidal shape, as expected from a dipole.

5.7 Numerical evaluation of induced fields distribution

In order to illustrate the experimentally observed phenomena, the system is modeled by discrete array of 32×32 ASR meta-molecules each consisting of two closely-spaced asymmetric resonators which interact via free electromagnetic field (see Fig. 5.1). The numerical model was developed by Dr. S. D. Jenkins and Dr. J. Ruostekoski, from the School of Mathematics of the University of Southampton. It is assumed that each resonator supports a single mode of current oscillation, with a specific resonance frequency, generating oscillating electric and magnetic multipole moments. A system of $2N$ single-mode resonators then possesses $2N$ collective modes of current oscillation. It is assumed that the dominant contribution of interactions is due to the dipole fields and ignore the higher order multipoles. The low-energy collective modes can then be separated to those with dominantly magnetic or electric dipole excitation, and here M_{ij} refers to modes with dominantly magnetic excitation that exhibit suppressed radiative emission rates. This model demonstrated the dramatic narrowing of the transmission resonance linewidth due to the collective effects as a function of the number of resonators [128], representing the experimental observations [49].

The collective modes are numerically calculated and their contribution to the steady-state response to the electron beam. As a results of strong interactions, the initial localized excitation propagates in the metamaterial. One can think of this propagating wave as a superposition of the collective modes. At later times the modes M_{ij} with most suppressed radiative emission rates become dominant and, provided that the driving is near-resonant on the phase-coherent uniform mode M_{11}, the system quickly settles down to a steady-state with a considerable proportion of the excitation in M_{11}.

It is found that, due to strong collective interactions between the resonators, localized electron beam injection excites a notably larger spatial area of the metamaterial in the steady-state response. As the illumination area increases, the number of excited resonators increases and the excitation approaches the phase-coherent collective magnetic mode M_{11} of the lattice. For driving a single ASR at the resonance frequency of M_{11}, the dominance of the M_{11} mode, which extends over the entire metamaterial

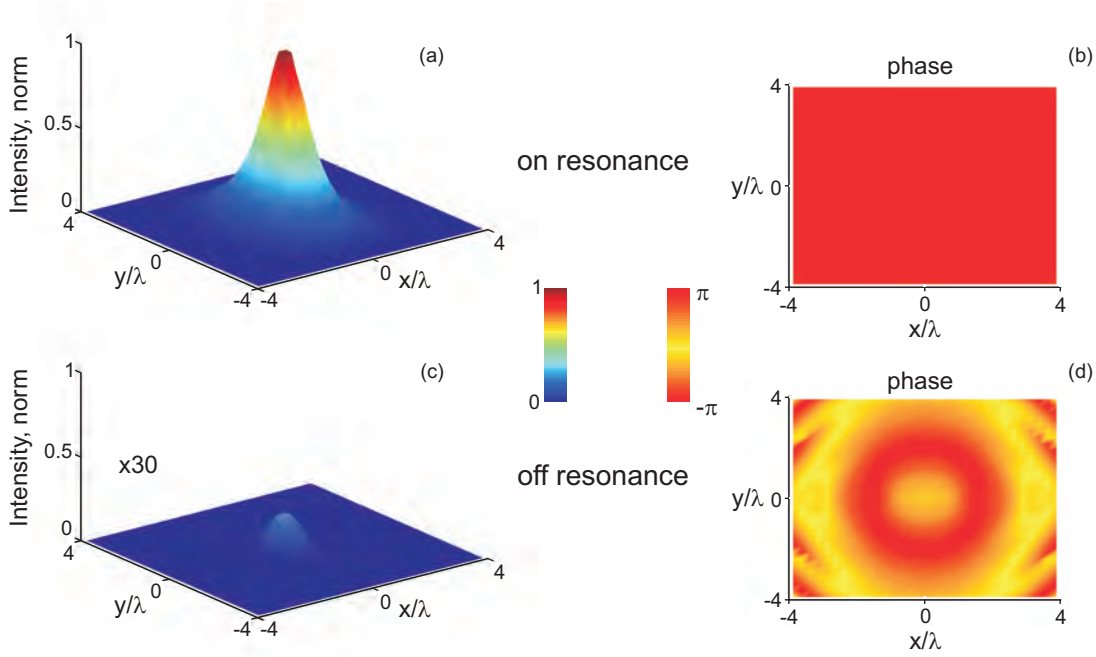

Figure 5.12: ***On and Off resonance response*** *Excitation intensity (a) and phase (b) of the response to a driving resonant on the uniform collective magnetic mode of current oscillation illustrates that such a driving can excite a broad area of the metamaterial array with high phase coherence. The off-resonant excitation intensity (c) and phase (d) of the response to a driving detuned by 8 line widths of the uniform mode from its resonance show a significantly weaker excitation and lower phase coherence, representing poor coupling to a plane wave propagating perpendicular to the array.*

array, is already remarkably high with about 70% of the total excitation. For the resonant illumination of four ASRs (Fig. 5.12(a,b)), the excited area is further increased and the contribution of M_{11} is about 85%, as shown in Fig. 5.1. The phase-coherence of the steady-state excitation can be described by calculating the intensity-weighted variance of the phase, $(\Delta\phi)^2$, for the excited resonators. The highly phase-coherent excitation of Fig. 5.12(a,b) exhibits a phase variation of only $\Delta\phi = 2.20°$. The conversion of the electron beam illumination to the phase-coherent M_{11} mode is sensitive to the excitation frequency.

For the field off-resonant by eight linewidths of M_{11} exhibits a significantly weaker excitation and lower phase coherence ((Fig. 5.12(c,d)); the contribution of M_{11} is already reduced to 41% and the phase variation is increased tenfold to $\Delta\phi = 25.4°$. Moreover, the collective effects, that are responsible for the coherent metamaterial excitation, are due to cooperative response of the strongly interacting, closely-spaced

resonators [128]: recurrent scattering events in which a photon/surface plasmon is repeatedly scattered from the same meta-molecule result in collective modes with strongly suppressed decay rates, representing waves being trapped due to scattering. The response is sensitive to the spatial separation between the meta-molecules with an increase in the array spacing rapidly leading to suppressed interactions.

5.8 Conclusions

In summary, it has been observed a fundamentally new phenomenon of conversion of the energy of free electrons injected into a small spot in the metamaterial array into a spatially coherent light emission of the array. This effect is confirmed both experimentally, through intensity increase and linewidth narrowing of the emitted light with the number of metamolecules involved in the process together with collimated emission, and numerically, through simulations showing how a metamaterial array can collective emit when locally excited. The effect described in this chapter is clearly limited by the losses in the metal at the frequency used in the experiment; it would be very important to try increasing the interaction area (number of meta-molecules) by reducing the losses and two possible routes are worth investigating: move more towards the infrared or hybridizing the metamaterial with gain material. The latter approach could also lead to the experimental demonstration of a free-electron pumped lasing spaser.

6 Conclusions

6.1 Summary

This thesis is a study about the feasibility of nanoscale light sources driven by electron beams. Three kind of light sources have been experimentally and numerically investigated: optical nano-antennas, a well milled in a stack of alternating materials and planar plasmonic metamaterials.

Prior to the work reported here, free-electrons based radiation sources were demonstrated in the GHz and THz frequency range. Experiments reporting light emitted by single nanoscale object illuminated by electron beams were conducted since ten years, however all of them were using the emitted light to investigate of the plasmonic properties of single nanoparticles, while this has been the first consistent set of works that aimed at employing free-electrons to 'drive' nanoscale structures with the view of creating nanoscale light sources.

In this thesis a number of experimental advances have been made, first time demonstrations have been achieved and new phenomena have been discovered.

- It was shown that free-electrons can indeed drive various kinds of light source of nanoscale dimensions.
- It was shown that, thanks to the broadband nature of free-electrons excitation, it is possible to 'pump' nanoscale light sources operating across a wide spectral range (vis-IR).
- The first **optical nano-antenna fed by free-electrons** has been experimentally

demonstrated. It was shown that, in optical antennas based on coupled elements, an enhanced light emission is achieved when feeding appropriately.

- An 'undulator' cavity, based on permittivity contrast between just 200 nm thick layers, with a lateral dimension of only 700 nm and a length of 2.2 μm has been manufactured.
- It has been demonstrated the first **nanoscale tunable light source** "on a chip" driven by free electrons.
- It was demonstrated light emission from planar plasmonic metamaterials excited by free electron, with wavelength of emission linked to meta-molecule size and geometry,
- It was discovered a new phenomenon in 'coherent' plasmonic metamaterials: **conversion of the energy of free electrons into a spatially coherent light emission**, due to inter-metamolecular interaction.

6.2 Outlook

The experiments reported in thesis are mainly "proof of concept" demonstrations. Each of them though shows that there is room for further studies for each of the three type of nanoscale optical sources investigated. Here it is given a very brief outlook on what it is still left to do for each of the three directions.

Optical nanoantennas

In this thesis it was demonstrated the possibility to feed a dipole nano-antennas with free electrons. It could be very interesting to extend this work to other antenna geometries to validate this approach for any kind of optical antennas. It would be interesting to integrate the nano-antenna with a source of electrons, in order to build fully functional, integrated devices.

Nanoscale FELs-like sources

The most straightforward extension of the work reported in this thesis would be to bring the same approach to other spectral ranges and to investigate other mate-

rial compositions, in order to assess the capabilities and efficiency of the approach. It would be of paramount importance to attempt extending this approach to bring the light emission into lasing regime. This would require accurate evaluation of the conditions to achieve it and consistent experimental efforts and challenges as, for example, pre-bunch the electrons, have a very well collimated beam aling the path, etc. The payback however, a truly tunable nanoscale laser capable of accessing a wide spectral range, would be very high.

Metamaterials light sources

The experimental investigation carried out so far on this front is just at the first steps. The newly discovered phenomenon needs to be investigated further (e.g. study the coherence and the time dinamics); moreover it would be beneficial to depart from material luminescence (for example using other kind of metals or moving to IR). A very important step, since the effect studied here has to battle with losses, would be to combine the metamaterials with quantum dots, dye molecules or rare-earth-doped glasses. This might be a route to potentially demonstrate an electron-beam-pumped lasing spaser.

An engineering challenge ahead for all the type of sources discussed in this thesis will, obviously, be the integration with chip-scale free-electron sources. Substantial work has been done in this direction and practical devices have been already realised: microscopic electron sources have been developed for ultrahigh-frequency nanoelectronics and next-generation flat-panel displays [112].

It is finally pointed out that all the further studies would greatly benefit from insights into directionality of emission and emission patterns of the specific light source under investigation[1].

[1] A setup with such capabilities was indeed built to investigate the emission directivity of the metamaterial light source

A

Coherence of an electromagnetic wave

In Section 2.6 it was pointed out that coherence was one of the parameters through which characterise a light source and, to a first approximation, say whether or not it is a laser. In particular, the concepts of spatial and temporal coherence were introduced. In this section a more detailed description of these two concepts is provided and it is shown how they provide only a first-order description of the coherence properties of a source of electromagnetic waves. The analysis carried out in the pages that follow is based on classical laser physics textbooks, such as [89].

A.1 Degree of spatial and temporal coherence

In the case of a quasi-monochromatic source (spectral bandwidth $\Delta\omega$ much smaller than the mean frequency $< \omega >$), the electric field of the wave, at position $\mathbf{r}$ and time t can be be expressed as

$$E(\mathbf{r}, t) = A(\mathbf{r}, t)e^{(j[<\omega>t - \phi(\mathbf{r},t)])},$$

where $A(\mathbf{r}, t)$ and $\phi(\mathbf{r}, t)$ vary slowly within an optical cycle.

If measurements of the field are performed at a point $\mathbf{r}_1$ in space and times t_1 and t_2 within the time interval $[0, T]$, it is possible to calculate the product $E(\mathbf{r}_1, t_1)E^2(\mathbf{r}_2, t_2)$. When the same procedure is repeated over a large number of times, this allows to calculate the average of the product over all the measurements, which takes the name

of ensemble average

$$\Gamma^{(1)}(\mathbf{r}_1, \mathbf{r}_1, t_1, t_2) = \langle E(\mathbf{r}_1, t_1) E^*(\mathbf{r}_1, t_2) \rangle \,. \tag{A.1}$$

In the case of a stationary beam[1] (as e.g. is the case of a single mode c.w. laser, or a thermal light source), the ensemble average only depends on the time difference $\tau = t_1 - t_2$ rather than on the specific times t_1 and t_2

$$\Gamma^{(1)}(\mathbf{r}_1, \mathbf{r}_1, t_1, t_2) = \Gamma^{(1)}(\mathbf{r}_1, \mathbf{r}_1, \tau) = \langle E(\mathbf{r}_1, t+\tau) E^*(\mathbf{r}_1, t) \rangle \,. \tag{A.2}$$

From the definition of $\Gamma^{(1)}$ given above, the normalised function $\gamma^{(1)}(\mathbf{r}_1, \mathbf{r}_1, \tau)$ can be defined as follows

$$\gamma^{(1)} = \frac{\langle E(\mathbf{r}_1, t+\tau) E^*(\mathbf{r}_1, t) \rangle}{\langle E(\mathbf{r}_1, t) E^*(\mathbf{r}_1, t) \rangle^{1/2} \langle E(\mathbf{r}_1, t+\tau) E^*(\mathbf{r}_1, t+\tau) \rangle^{1/2}}. \tag{A.3}$$

The function $\gamma^{(1)}$ as defined in Eq. A.3 is called *complex degree of temporal coherence*, while its magnitude, $|\gamma^{(1)}|$, is referred to as *degree of temporal coherence*, and indeed it expresses the degree of correlation of the electric field of a wave at a point $\mathbf{r}_1$ in space at any two instants in time separated by a time interval τ. Furthermore it has the following properties: i) $\gamma^{(1)} \leq 1$ with the equal sign for $\tau = 0$; ii) it is symmetric with respect to τ.

From the properties stated above it follows that a beam has perfect temporal coherence when $\gamma^{(1)} = 1$ for any τ. For a c.w. beam this requires the signal to be a sinusoidal wave. The opposite case, total absence of coherence, occurs when $\gamma^{(1)} = 0$ for $\tau > 0$, and this would be the case of a light source of very wide bandwidth. For real sources, $|\gamma^{(1)}|$ generally peaks at $\tau = 0$ and decreases with increasing $|\tau|$; it is hence possible to define a *coherence time* τ_{co}, the time for which $|\gamma^{(1)}| = 1/2$. Obviously $\tau_{co} = \inf$ for a perfectly coherent course while $\tau_{co} = 0$ for a completely incoherent one. Finally, also a

[1] A process is said to be stationary when the ensemble average of any variable that describes it is independent of time [89]

coherence lenght of a beam can be defined as $L_{co} = c\tau_{co}$.

As in the case of temporal coherence, the same mathematical procedure can be followed for the spatial coherence properties of a beam; thus, a first-order correlation function between two points in space, $\mathbf{r}_1$ and $\mathbf{r}_2$ and the corresponding *complex degree of spatial coherence* can be defined, with the latter being expressed as

$$\gamma^{(1)} = \frac{\langle E(\mathbf{r}_1, t)E^*(\mathbf{r}_2, t)\rangle}{\langle E(\mathbf{r}_1, t)E^*(\mathbf{r}_1, t)\rangle^{1/2} \langle E(\mathbf{r}_2, t)E^*(\mathbf{r}_2, t)\rangle^{1/2}}. \tag{A.4}$$

Similarly to the temporal coherence case, now $|\gamma^{(1)}|$ takes the name of *degree of spatial coherence*, Indeed $\gamma^{(1)}$ expresses the degree of correlation of the field at two points in space $\mathbf{r}_1$ and $\mathbf{r}_2$ at any time t. Also in this case $|\gamma^{(1)}| \leq 1$. An electromagnetic wave will have perfect spatial coherence if $|\gamma^{(1)}| = 1$ for any two points $\mathbf{r}_1$ and $\mathbf{r}_2$ laying on the same wavefront (or on wave fronts whose separation is much smaller than the coherence length L_c). In general, for any practical case, a beam will show only partial spatial coherence.

A.2 Temporal coherence and linewidth

It was stated in Section 2.6 that, for a stationary beam, the temporal coherence is connected to the bandwidth of the signal through an inverse dependence. Here it is given a quick justification of the statement without however going into a rigorous demonstration, since this is beyond the scope of this thesis.

The first step is to notice that the spectrum of an electromagnetic wave is proportional to the power spectrum $W(\mathbf{r}, t)$ of the field. $E(\mathbf{r}, t)$. The power spectrum W in turn is related to the autocorrelation function $\Gamma^{(1)}$ through the Fourier transform, thus making possible to obtain either of this quantities once the other is known.

It is possible to define the coherence time τ_{co} as the variance σ_τ of the function $|\Gamma^{(1)}\tau|^2$ and similarly the bandwidth $\Delta\nu_L$ of the signal as the variance σ_ν of $W^2(\nu)$.

Since W and $\Gamma^{(1)}$, as said before, are related by Fourier transform,it can be shown that σ_τ and σ_ν satisfy the condition

$$\sigma_\tau \sigma_\nu \geq (1/4\pi)$$

where the equal sign applies when the $\Gamma^{(1)}$ and W are Gaussian function, thus giving the inverse dependence as stated above.

A.3 Statistical properties of laser light and thermal light

In most cases, the degrees of spatial and temporal coherence, as defined above, are sufficient to distinguish a laser source from a thermal one, nevertheless they are the properties that define a fundamental difference between the two. Indeed it is possible to device and experiment in which the outputs of a laser and a thermal source both show a high order of temporal and spatial coherence (see [88, 89]).

Despite this fact, they still remain fundamentally different and this can be shown either looking at the statistical properties of both beams or comparing higher order of coherence.

The first case finds its explanation in the fact that, in a laser the output intensity and hence the field amplitude is fixed, for a given pumping rate, by the condition that upward transitions, due to pumping, must be balanced by downward transitions due to both stimulated and spontaneous emission while, in a thermal source, the field is the superposition of the uncorrelated light emitted, by spontaneous emission, from the individual atoms of the light source [89]. This makes the statistical distributions very different from each other.

If higher order of coherence are instead taken into account, one finds that, even in the case of similar first order coherence, a monomodal laser source has a much larger high-order coherence than any other source [89].

B

Angle resolved EIRE

In Section 5.6 the angular distribution of the light emitted by a planar photonic metamaterial excited by free-electrons was investigated. In particular, it was shown that it has been possible to map the information recorded by the CCD array onto emission angles with respect to the focus position. In this section the procedure to retrieve angular information is described and the full characterization of the metamaterial sample is presented.

B.1 Parabolic mirror angles mapping onto CCD

As already anticipated in Section 5.6, if the sample is well positioned at the focus of the mirror, each pixel of the CCD can be associated to a specific point of the paraboloid and, in turn, to an angular coordinates pair (ϕ, θ), where θ is the polar (or zenith) angle spanning from 0 to 90 degrees ($\phi = 0$ being the normal to the sample surface) and ϕ is the azimuthal angle running from 0 to 360 degrees. Fig. B.1a shows a schematic of the geometrical features just described. Along with the angles ϕ and θ, the solid angle Ω covered by each pixel's area must be taken into account to correct the data. Figures B.1b,c and d show how each pixel in the CCD image is mapped onto respectively the angles θ, ϕ and Ω.

B.2 CCD image recording

In order to image the emission spatial pattern, a CCD array is positioned in the optical path following the parabolic mirror (see Fig. B.2a). The images 'as-recorded' on

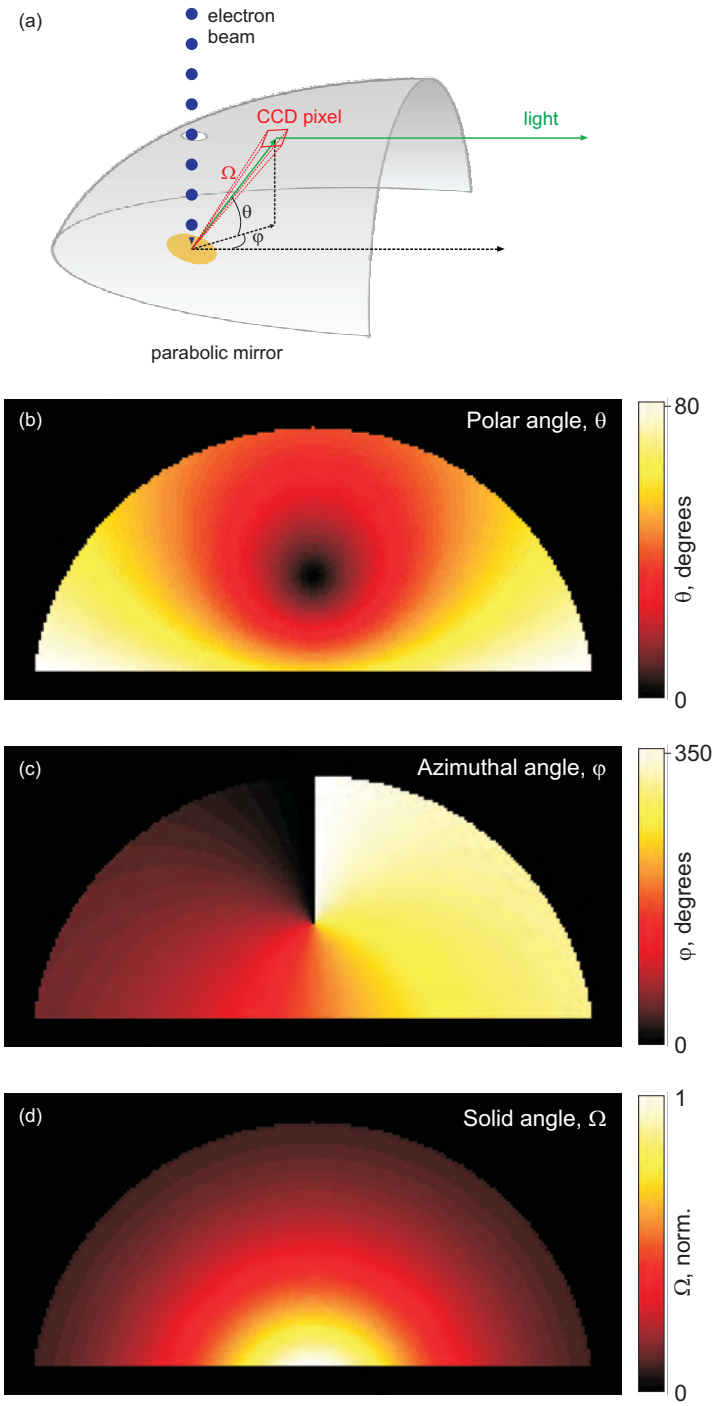

Figure B.1: ***Parabolic mirror angles mapping onto CCD*** *(a) Schematic of the experimental setup, and maps relating pixel position to (b) polar angle θ (c) azimuthal angle ϕ and (d) solid angle Ω*

C Publications

C.1 Journal Publications

- A. I. Denisyuk, G. Adamo, K. F. Macdonald, J. Edgar, M. D. Arnold, V. Myroshnychenko, M. J. Ford, F. J. García de Abajo, and N. I. Zheludev. "Transmitting Hertzian Optical Nanoantenna with Free-Electron Feed.". *Nano Lett.*, 10:3250–3252, 2010

- V. K. Tikhomirov, G. Adamo, A. E. Nikolaenko, V. D. Rodriguez, P. Gredin, M. Mortier, N. I. Zheludev and V. V. Moshchalkov. "Cathodo- and photoluminescence in Yb3+-Er3+ co-doped PbF2 nanoparticles". *Opt. Exp.*, 18:8836, 2010

- G Adamo, K F MacDonald, Y H Fu, D P Tsai, F J García de Abajo, and N I Zheludev. "Tuneable electron-beam-driven nanoscale light source". *Journal of Optics*, 12:024012, 2010

- G. Adamo, K. F. MacDonald, Y. H. Fu, C-M. Wang, D. P. Tsai, F. J. García de Abajo, and N. I. Zheludev. "Light well: A tunable free-electron light source on a chip". *Phys. Rev. Lett.*, 103:113901, 2009. Also selected for *Virtual Journal of Nanoscale Science & Technology*, 20(12), 2009.

C.2 In preparation

- G. Adamo, J. -Y. Ou, J.K. So, K. MacDonald, F. De Angelis, E. Di Fabrizio, S. D. Jenkins, J. Ruostekoski and N. I. Zheludev. "Spatially coherent light emission

the CCD appear like the ones in Fig. B.2b and c[1]. It is easy to identify the semi-circular shape of the mirror transversal section and the position of the hole (for the free-electrons to reach the sample). Fig. B.2b corresponds to the emission of light from a flat gold surface over the full spectral range of the spectrometer, [400-1100] nm, while Fig. B.2c shows the emission produced by free-electrons hitting the patterned metamaterial surface; Fig. B.2d finally shows the emission from metamaterial only, obtained removing emission in (b) by emission in (c). The patterns can be analysed referring to the angular maps of in Fig. B.1: the CCD area around the mirror's hole corresponds to angles very close to the normal, while other parts to more grazing angles. This allows to infer that the emission pattern for the flat gold (Fig. B.2b) suggests a toroidal shape, as expected for a dipole (low emission at normal angles and higher at grazing angles) while, when the electron beam is positioned onto the metamaterial array (Fig. B.2c), a bright area around the hole is added to the pattern of Fig. B.2b. This is very clear when the emission for the metamaterial alone is considered (Fig. B.2d): the emission of light is higher at the normal angle (except for the hole) and degrades with increasing angles.

B.3 Emission directivity

The hints discussed above represent just a qualitatively analysis of the emission. The angles-pixel position correspondence allows to convert the emission intensities 'as-recorded' into proper angular maps as the ones shown in Fig. B.3, where over the radius it is reported the elevation of the emitted light, θ while on the angles the azimuthal information ϕ can be read.

Left to right column of Fig. B.3 show emission maps for, respectively, Au, Au + metamaterial, and metamaterial alone in the case of: emission over the full spectral range, 400-1100 nm (Fig. B.3a to c); emission OFF-resonance at 500 nm (Fig. B.3d to f) and ON-resonance at 650 nm (Fig. B.3g to i).

The light emitted from flat gold when illuminated with the electrons is distributed on a quite clear toroidal shape in all three cases (Fig. B.3a, d, g); the metamaterial contribution can be clearly identified when the emission is either sampled ON-resonance

[1]The sample analysed in this Appendix is the same used for the experiment reported in Section 5: 50 nm of Au above a 100 nm Si_3N_4 membrane

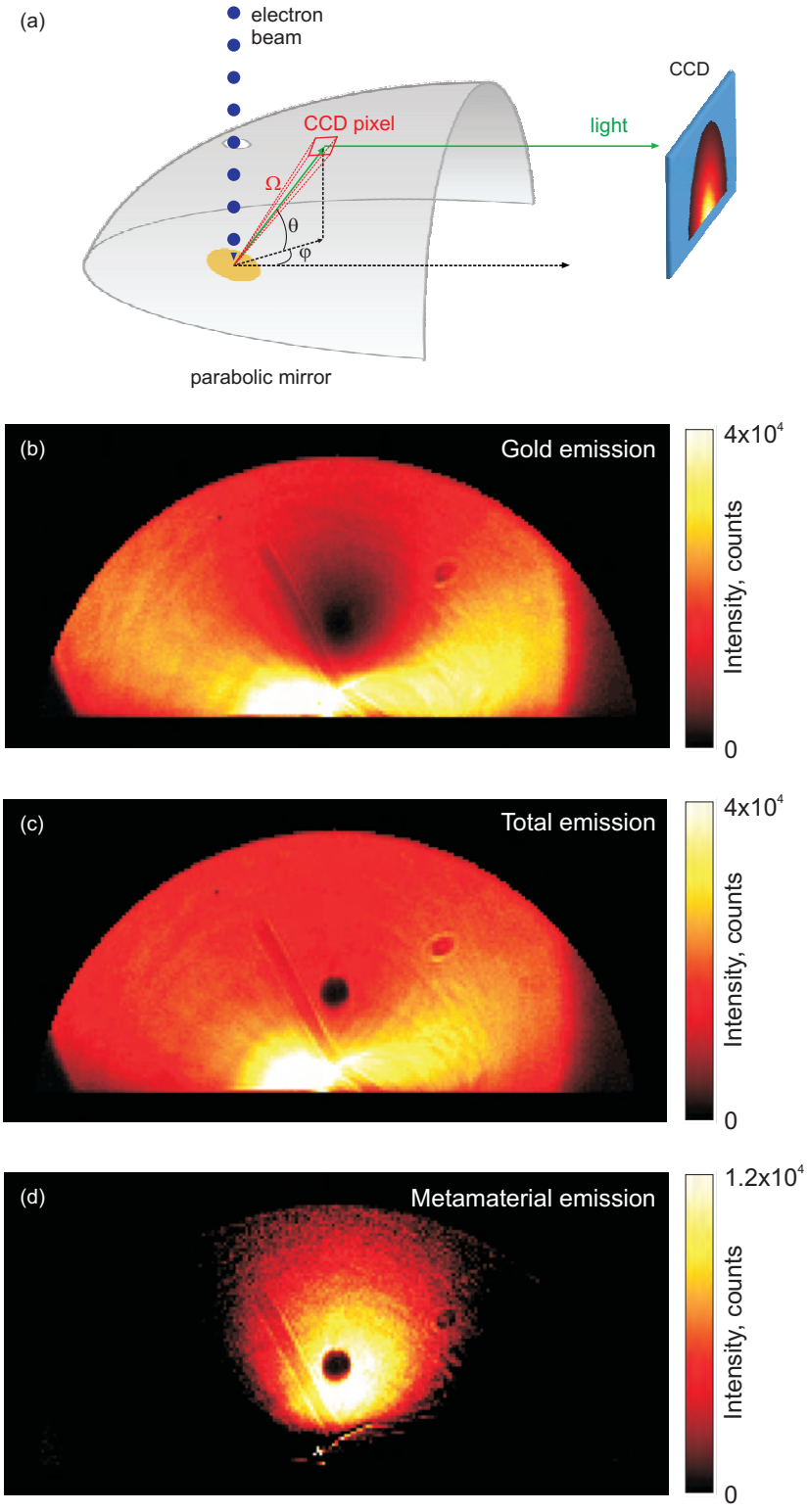

Figure B.2: ***Emission from Au and metamaterial as measured on CCD*** *(a) Schematic of the experimental setup, and CCD images showing the measured emission for (b) flat Au, (c) Au + metamaterial and (d) metamaterial alone, obtained subtracting the Au background (b) from metamaterial signal (c)*

(Fig. B.3i) or collected over the full spectrum (Fig. B.3c), while disappears almost completely OFF-resonance (Fig. B.3f).

If the signal intensity is integrated over the the azimuthal angle ϕ, the vertical direction of light emission can be easily visualised, as in Fig. B.4, where the curves correspond exactly to the maps of Fig. B.3. It is easy to see that light emission from gold (see Fig. B.4a, d, g) happens at an angle ϕ of about 55 degrees from the normal to the sample, while the free-electron driven metamaterial emits long the normal direction with a divergence of about 30 degrees.

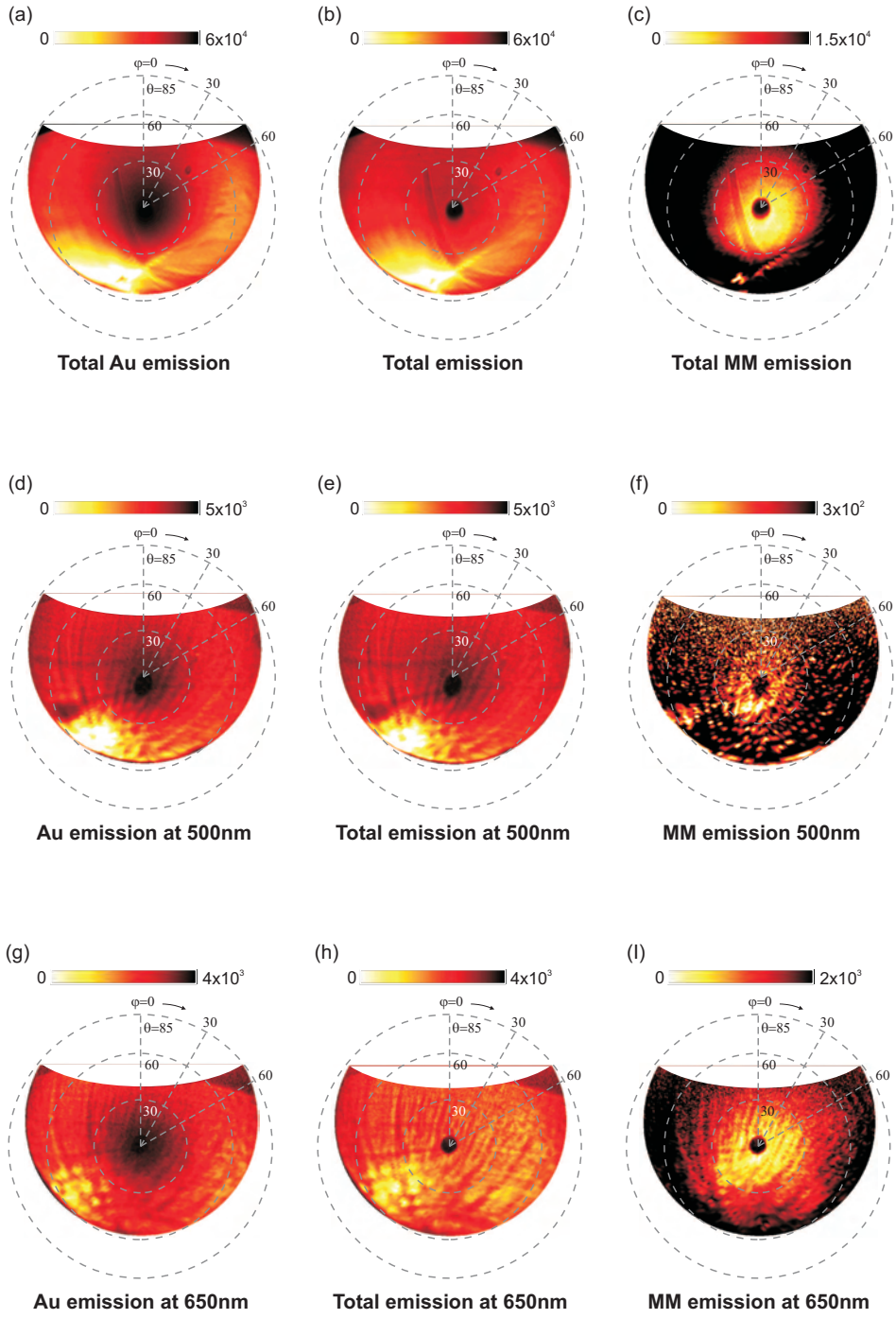

Figure B.3: ***Polar maps of emission intensities*** *Intensity maps of light emission from (respectively from left to right on columns) Au, Au + metamaterial and metamaterial alone in the case of (a-c) light collected over the full spectral range 400-1000nm, (d-f) signal filtered at 500nm and (g-i) light filtered at 650nm.*

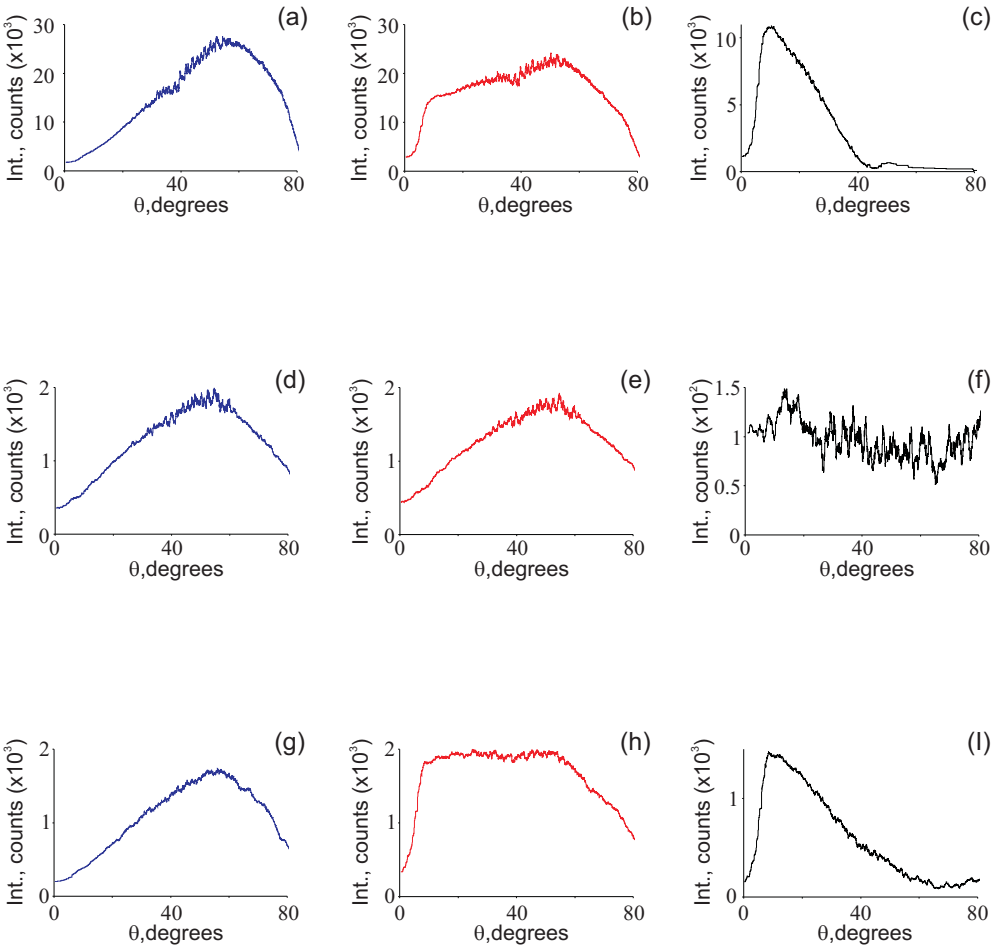

Figure B.4: ***Average intensity over polar angle*** *Intensity of light emission from (respectively from left to right on columns) Au, Au + metamaterial and metamaterial alone in the case of (a-c) light collected over the full spectral range 400-1000nm, (d-f) signal filtered at 500nm and (g-i) light filtered at 650nm.*

from a metamaterial source driven by electron beam". to be submitted

- V. Myroshnychenko, J. F. García de Abajo, N. Geuquet, L. Henrard, E. Carbó-Argibay, J. Rodríguez-Fernandez, I. Pastoriza-Santos, J.Pérez-Juste, L. M. Liz-Marzán, G. Adamo, K. F. MacDonald, N. I. Zheludev, J. Nelayah, O. Stéphan, M. Kociak and C. Colliex. "Spectroscopy and imaging of gold nanodecahedra". to be submitted to Nano Letters

C.3 Conference Contributions

- (oral) G. Adamo, J. -Y. Ou, K. MacDonald, F. De Angelis, E. Di Fabrizio and N. I. Zheludev. "Electron-beam-driven nanoscale metamaterial light sources". *CLEO/Europe-EQEC*, Munich, Germany, 22 - 26 May 2011

- (poster) G. Adamo, K. MacDonald, F. De Angelis, E. Di Fabrizio and N. I. Zheludev. "Metamaterial Light Sources Driven by Electron Beams". *NANOMETA 2011*, Seefeld, Austria, 3 - 6 Jan 2011

- (oral) G. Adamo, K. MacDonald, F. De Angelis, E. Di Fabrizio and N. I. Zheludev. "Nanoscale electron-beam-driven metamaterial light sources". *IEEE Photonics Society 23rd Annual Meeting*, Denver, USA, 07 - 11 Nov 2010

- (oral) Z. L. Sámson, J. Zhang, G. Adamo, T. Uchino, B. Gholipour, K. Knight, C-C. Huang, F. De Angelis, K. F. MacDonald, P. Ashburn, E. Di Fabrizio, D. W. Hewak, and N. I. Zheludev. "Chalcogenide plasmonic metamaterial switches". *SPIE Optics & Photonics*, San Diego, USA, 01 - 05 Aug 2010

- (oral) V. Myroshnychenko, J. Nelayah, O. Stéphan, M. Kociak, C. Colliex, G. Adamo, K. F. MacDonald, N. I. Zheludev, E. Carbó-Argibay, J. Rodríguez-Fernandez, L. M. Liz-Marzán, and J. F. García de Abajo. "Electron energy loss spectroscopy and cathodoluminescence as powerful tools for studying surface-plasmon modes in metal nanostructures". *SPIE Photonics Europe 2010*, Brussels, Belgium, 12 - 16 Apr 2010

- (oral) Z. L. Sámson, G. Adamo, K. F. MacDonald, K. Knight, F. De Angelis, A. Nikolaenko, C. C. Huang, E. Di Fabrizio, D. W. Hewak, and N. I. Zheludev.

"Switching metamaterials with electronic signals and electron-beam excitations". *SPIE Photonics Europe 2010*, Brussels, Belgium, 12 - 16 Apr 2010

- (keynote) N. I. Zheludev, A. Nikolaenko, K. F. MacDonald, V. A. Fedotov, D. Hewak, G. Adamo, Z. Sámson, E. Plum, D. P. Tsai, E. Difabrizio, and F. De Angelis. "Nonlinear and switchable plasmonic metamaterials". *PIERS 2010*, Xi'an, China, 22 - 26 Mar 2010

- (oral) V. Myroshnychenko, J. Nelayah, M. Kociak, O. Stéphan, C. Colliex, G. Adamo, K. F. MacDonald, N. I. Zheludev, J. Rodríguez-Fernandez, E. Carbó-Argibay, I.Pastoriza-Santos, J.Pérez-Juste, L. M. Liz-Marzán, and J. F. García de Abajo. "Probing surface-plasmon modes in noble metal nanoparticles using an electron beam". *META '10*, Cairo, Egypt, 22 - 25 Feb 2010

- (Postdeadline) Z. L. Sámson, K. F. MacDonald, F. De Angelis, G. Adamo, K. Knight, C. C. Huang, D. W. Hewak, E. Di Fabrizio, and N. I. Zheludev. "Chalcogenide glass metamaterial optical switch". *FiO 2009*, San Jose, USA, 11 - 15 Oct 2009

- (invited) N. I. Zheludev, G. Adamo, Y. H. Fu, K. F. MacDonald, C. -M. Wang, D. P. Tsai and J. F. García de Abajo. "Nanoscale tuneable light source". *SPIE Optics & Photonics 2009*, San Diego, USA, 2 - 6 Aug 2009

- (invited) V. Myroshnychenko, J. Nelayah, M. Kociak, O. Stéphan, C. Colliex, G. Adamo, K. F. MacDonald, N. I. Zheludev, J. Rodríguez-Fernandez, E. Carbó-Argibay, L. M. Liz-Marzán, and J. F. García de Abajo. "Plasmon modes in individual noble metal nanoparticles". *SPIE Optics & Photonics 2009*, San Diego, USA, 2 - 6 Aug 2009

- (oral) G. Adamo, Y. H. Fu, K. F. MacDonald, C. -M. Wang, D. P. Tsai, J. F. García de Abajo, and N. I. Zheludev. "Free-electron pumped tunable nanoscale light-source: the 'light-well'". *SPP4*, Amsterdam, The Netherlands, 21 - 26 Jun 2009

- (poster) V. Myroshnychenko, J. Nelayah, M. Kociak, O. Stéphan, C. Colliex, G. Adamo, K. F. MacDonald, N. I. Zheludev, J. Rodríguez-Fernandez, E. Carbó-

Argibay, L. M. Liz-Marzán, and J. F. García de Abajo. "Plasmon modes in individual noble metal nanoparticles". *ETOPIM 8*, Crete, Greece, 7 - 12 Jun 2009

- (oral) G. Adamo, K. F. MacDonald, Y. H. Fu, C. -M. Wang, D. P. Tsai, J. F. García de Abajo, and N. I. Zheludev. "Tunable nanoscale free-electron source of photons and plasmons"'. *CLEO/IQEC 2009*, Baltimore, USA, 31 May - 5 Jun 2009

- (invited) G. Adamo, K. F. MacDonald, N. I. Zheludev, Y. H. Fu, C. -M. Wang, D. P. Tsai, and J. F. García de Abajo. "The 'Light-well': A tuneable nanoscale free-electron light source on-a-chip"'. *MRS Spring Meeting*, San Francisco, USA, 13 - 17 Apr 2009

- (poster) A. I. Denisyuk, G. Adamo, K. F. MacDonald, B. Rodríguez-González, I. Pastoriza-Santos, M. Spuch-Calvar, L. M. Liz-Marzán, M. D. Arnold, M. J. Ford, J. F. García de Abajo, and N. I. Zheludev. "Emission hotspots in complex metal nanostructures"'. *NANOMETA 2009*, Seefeld, Austria, 5 - 8 Jan 2009

- (oral) G. Adamo, K. F. MacDonald, N. I. Zheludev, Y. H. Fu, C. -M. Wang, D. P. Tsai, and J. F. García de Abajo. "The 'Light-Well': A tuneable free-electron light source on-a-chip"'. *NANOMETA 2009*, Seefeld, Austria, 5 - 8 Jan 2009

- (oral) K. F. MacDonald, G. Adamo, N. I. Zheludev, J. F. García de Abajo, Y. H. Fu, C. -M. Wang, and D. P. Tsai. "Nano 'Light Well': a free-electron light source on-a-chip"'. *OSA Plasmonics and Metamaterials (META) Topical Meeting*, Rochester, USA, 21 - 24 Oct 2008

References

[1] L. Novotny and N. F. van Hulst. "Antennas for light". *Nat. Photon.*, 5:83–90, 2011.

[2] J. Wessel. "Surface-enhanced optical microscopy". *J. Opt. Soc. Am. B*, 2:1538–1540, 1985.

[3] U. C. Fischer and D. W. Pohl. "Observation on single-particle plasmon by near-field optical micriscopy". *Phys. Rev. Lett.*, 62:458–461, 1989.

[4] L. Tang, S. E. Kocabas, S. Latif, A. K. Okyay, D.-S. Ly-Gagnon, K. C. Saraswat, and D. A. B. Miller. "Nanometre-scale germanium photodetector enhanced by a near-infrared dipole antenna". *Nat. Photon.*, 2:226–229, 2008.

[5] H. A. Atwater and A. Polman. "Plasmonics for improved photovoltaic devices". *Nat. Mater.*, 9:205–213, 2010.

[6] T. H. Taminiau, F. D. Stefani, F. B. Segerink, and N. F. Van Hulst. "Optical antennas direct single-molecule emission". *Nat. Photon.*, 2(4):234–237, 2008.

[7] M. Lippitz, M. A. van Dijk, and M. Orrit. "Third-Harmonic Generation from Single Gold Nanoparticles". *Nano Lett.*, 5:799–802, 2005.

[8] A. G. Curto, G. Volpe, T. H. Taminiau, M. P. Kreuzer, R. Quidant, and N. F. van Hulst. "Unidirectional Emission of a Quantum Dot Coupled to a Nanoantenna". *Science*, 329:930–933, 2010.

[9] M. W. Knight, H. Sobhani, P. Nordlander, and N. J. Halas. "Photodetection with Active Optical Antennas". *Science*, 332:702–704, 2011.

[10] A. I. Denisyuk, G. Adamo, K. F. Macdonald, J. Edgar, M. D. Arnold, V. Myroshnychenko, M. J. Ford, F. J. García de Abajo, and N. I. Zheludev. "Transmitting Hertzian Optical Nanoantenna with Free-Electron Feed.". *Nano Lett.*, 10:3250–3252, 2010.

[11] J. C. Johnson, H.-J. Choi, K. P. Knutsen, R. D. Schaller, P. Yang, and R. J. Saykally. "Single gallium nitride nanowire lasers". *Nat. Mater.*, 1:106–110, 2002.

[12] M. T. Hill, Y.-S. Oei, B. Smalbrugge, Y. Zhu, T. de Vries, P. J. van Veldhoven, F. W. M. van Otten, T. J. Eijkemans, J. P. Turkiewicz, H. de Waardt, E. J. Geluk, S.-H. Kwon, Y.-H. Lee, R. Nötzel, and M. K. Smit. "Lasing in metallic-coated nanocavities". *Nat. Photon.*, 1:589–594, 2007.

[13] M. P. Nezhad, A. Simic, O. Bondarenko, B. Slutsky, A. Mizrahi, L. Feng, V. Lomakin, and Y. Fainman. "Room-temperature subwavelength metallo-dielectric lasers". *Nat. Photon.*, 4:395–399, 2010.

[14] H. Altug, D. Englund, and J. Vucković. "Ultrafast photonic crystal nanocavity laser". *Nat. Phys.*, 2:484–488, 2006.

[15] Rupert F Oulton, Volker J Sorger, Thomas Zentgraf, Ren-min Ma, Christopher Gladden, Lun Dai, Guy Bartal, and Xiang Zhang. "Plasmon lasers at deep subwavelength scale". *Nature*, 461:629–632, 2009.

[16] M A Noginov, G Zhu, A M Belgrave, R Bakker, V M Shalaev, E E Narimanov, S Stout, E Herz, T Suteewong, and U Wiesner. "Demonstration of a spaser-based nanolaser". *Nature*, 460:1110–1112, 2009.

[17] R.-M. Ma, R. F. Oulton, V. J. Sorger, G. Bartal, and X. Zhang. "Room-temperature sub-diffraction-limited plasmon laser by total internal reflection". *Nat. Mater.*, 10:110–113, 2010.

[18] S. Lal, S. Link, and N. J. Halas. "Nano-optics from sensing to waveguiding". *Nat. Photon.*, 1:641–648, 2007.

[19] Dmitri K Gramotnev and Sergey I Bozhevolnyi. "Plasmonics beyond the diffraction limit". *Nat. Photon.*, 4:83–91, 2010.

[20] J. A. Schuller, E. S. Barnard, W. Cai, Y. C. Jun, J. S. White, and M. L. Brongersma. "Plasmonics for extreme light concentration Plasmonics for extreme light concentration and manipulation". *Nat. Mater.*, 9:193–204, 2010.

[21] K. F. MacDonald, Z. L. Samsón, M. I. Stockman, and N. I. Zheludev. "Ultrafast active plasmonics". *Nat. Photon.*, 3:55–58, 2009.

[22] All-Plasmonic Modulation via Stimulated Emission of Copropagating Surface Plasmon Polaritons on a Substrate with Gain. "Krasavin, A. V. and Vo, T. P. and Dickson, W. and Bolger, P. M. and Zayats, A. V.". *Nano Lett.*, 11:2231–2235, 2011.

[23] V. J. Sorger, Z. Ye, R. F. Oulton, Y. Wang, G. Bartal, X. Yin, and X. Zhang. "Experimental demonstration of low-loss optical waveguiding at deep sub-wavelength scales". *Nat. Commun.*, 2(331), 2011.

[24] A. Tsiatmas, V. A. Fedotov, and N. I. Zheludev. "Plasmonics without losses? (the case for terahertz superconducting plasmonics)". *arXiv.org*, 1105.3045, 2011.

[25] D. M. Koller, A. Hohenau, H. Ditlbacher, N. Galler, F. Reil, F. R. Aussenegg, A. Leitner, E. J. W. List, and J. R. Krenn. "Organic plasmon-emitting diode". *Nat. Photon.*, 2:684–687, 2008.

[26] R. J. Walters, R. V. A. van Loon, I. Brunets, J. Schmitz, and A. Polman. "A silicon-based electrical source of surface plasmon polaritons". *Nat. Mater.*, 9:21–25, 2009.

[27] D. J. Bergman and M. I. Stockman. "Surface plasmon amplification by stimulated emission of radiation: quantum generation of coherent surface plasmons in nanosystems". *Phys. Rev. Lett.*, 90:027402, 2003.

[28] J. Brown. "Artificial dielectrics having refractive indices less than unity". *Proc. IEE*, 100:51, 1953.

[29] W. Rotman. “Plasma simulation by artificial dielectric and parallel-plate media”. *IRE Transactions on Antennas and Propagation*, 10:82, 1962.

[30] W. N. Hardy and L. A. Whitehead. “Split-ring resonator for use in magnetic resonance from 200-2000 MHz”. *Rev. Sci. Instrum.*, 52:213, 1981.

[31] J. B. Pendry, A. J. Holden, D. J. Robbins, and W. J. Stewart. “Magnetism from conductors and enhanced nonlinear phenomena”. *IEEE Trans. Microwave Theory Tech.*, 47:2075, 1999.

[32] D. R. Smith, W. J. Padilla, D. C. Vier, S. C. Nemat-Nasser, and S. Schultz. “Composite Medium with Simultaneously Negative Permeability and Permittivity”. *Phys. Rev. Lett.*, 84:4184, 2000.

[33] V. G. Veselago. “The Electrodynamics of Substances with Simultaneously Negative Values of ε and μ”. *Sov. Phys. Uspekhi*, 10:509, 1968.

[34] R. A. Shelby, D. R. Smith, and S. Schultz. “Experimental Verification of a Negative Index of Refraction”. *Science*, 292:77–79, 2001.

[35] J. B. Pendry. “Negative Refraction Makes a Perfect Lens”. *Phys. Rev. Lett.*, 85:3966, 2000.

[36] N. Fang, H. Lee, C. Sun, and X. Zhang. “Sub-Diffraction-Limited Optical Imaging with a Silver Superlens”. *Science*, 308:534–537, 2005.

[37] J. B. Pendry, D. Schurig, and D. R. Smith. “Controlling electromagnetic fields”. *Science*, 312:1780, 2006.

[38] U. Leonhardt. “Optical conformal mapping”. *Science*, 312:1777, 2006.

[39] D. Schurig, J. J. Mock, B. J. Justice, S. A. Cummer, J. B. Pendry, A. F. Starr, and D. R. Smith. “Metamaterial electromagnetic cloak at microwave frequencies”. *Science*, 314:977, 2006.

[40] W. Cai, U. K. Chettiar, A. V. Kildishev, and V. M. Shalaev. “Optical cloaking with metamaterials”. *Nature Photonics*, 1:224, 2007.

[41] A. E. Nikolaenko, F. De Angelis, S. A. Boden, N. Papasimakis, P. Ashburn, E. Di Fabrizio, and N. I. Zheludev. "Carbon Nanotubes in a Photonic Metamaterial". *Phys. Rev. Lett.*, 104:153902, 2010.

[42] T. Driscoll, H.-T Kim, B.-G. Chae, B.-J. Kim, Y.-W. Lee, N. M. Jokerst, S. Palit, D. R. Smith, M. Di Ventra, and D. N. Basov. "Memory Metamaterials". *Science*, 325:1518–1521, 2009.

[43] Z. L. Samsón, K. F. Macdonald, F. De Angelis, B. Gholipour, K. Knight, C.-C. Huang, E. Di Fabrizio, D. W. Hewak, and N. I. Zheludev. "Metamaterial electro-optic switch of nanoscale thickness". *Appl. Phys. Lett.*, 96:143105, 2010.

[44] S. Xiao, V. P. Drachev, A. V. Kildishev, X. Ni, U. K. Chettiar, H.-K. Yuan, and V. M. Shalaev. "Loss-free and active optical negative-index metamaterials". *Nature*, 466:735–738, 2010.

[45] N. Meinzer, M. Ruther, S. Linden, C. M. Soukoulis, G. Khitrova, J. Hendrickson, H. M. Olitzky, J. D. Gibbs, and M. Wegener. "Arrays of Ag split-ring resonators coupled to InGaAs single-quantum-well gain". *Opt. Exp.*, 18:24140–24151, 2010.

[46] K. Tanaka, E. Plum, J.-Y. Ou, T. Uchino, and N. I. Zheludev. "Multifold Enhancement of Quantum Dor Luminescence in Plasmonic Metamaterials". *Phys. Rev. Lett.*, 105:227403, 2010.

[47] V. A. Fedotov, M. Rose, S. L. Prosvirnin, N. Papasimakis, and N. I. Zheludev. "Sharp Trapped-Mode Resonances in Planar Metamaterials with a Broken Structural Symmetry". *Phys. Rev. Lett.*, 99:147401, 2007.

[48] N. I. Zheludev, S. L. Prosvirnin, N. Papasimakis, and V. A. Fedotov. "Lasing spaser". *Nat. Photon.*, 2:351–354, 2008.

[49] V. A. Fedotov, N. Papasimakis, E. Plum, A. Bitzer, M. Walther, P. Kuo, D. P. Tsai, and N. I. Zheludev. "Spectral Collapse in Ensembles of Metamolecules". *Physical Review Letters*, 104:223901, 2010.

[50] B. W. J. McNeil and N. R. Thompson. "X-ray free-electron lasers". *Nat. Photon.*, 4:814–821, 2010.

[51] J. Walsh, B. Johnson, G. Dattoli, and A. Renieri. "Undulator and Cerenkov Free-Electron Lasers: A Preliminary Comparison". *Phys. Rev. Lett.*, 53:779–782, 1984.

[52] *A mm-wave, table-top Cerenkov free-electron laser*, 2004.

[53] *Development of a compact Cherenkov free-electron laser in Therahertz spectral range*, 2006.

[54] A. Gover and Z. Livni. "Operation regimes of Cerenkov-Smith-Purcell free electron lasers and t. w. amplifiers". *Opt. Comm.*, 26:375–380, 1978.

[55] J. Chen, Z. Liang, Y. Zhang, and Z. Yang. "A novel Smith-Purcell FEL". *Int. J. Inf. Mill. Waves*, 21:1563–1567, 2000.

[56] M. Wang, P. Liu, G. Ge, and R. Dong. "Free electron laser based on the Smith-Purcell radiation". *Opt. Las. Tech.*, 39:1254–1257, 2007.

[57] N. Yamamoto, K. Araya, and F. J. García de Abajo. "Photon emission from silver particles induced by a high-energy electron beam". *Phys. Rev. B*, 64(20):205419, 2001.

[58] E. J. R. Vesseur, R. de Waele, M. Kuttge, and A. Polman. "Direct observation of plasmonic modes in Au nanowires using high-resolution cathodoluminescence spectroscopy". *Nano Lett.*, 7:2843–2846, 2007.

[59] F. J. García de Abajo and M. Kociak. "Electron energy-gain spectroscopy". *New J. Phys.*, 10:073035, 2008.

[60] R. H. Ritchie. "Plasma losses by fast electrons in thin films.". *Phys. Rev.*, 106:874, 1957.

[61] C. J. Powell and J. B. Swan. "Origin f the characteristic electron energy losses in aluminum". *Phys. Rev.*, 115:869–875, 1959.

[62] Y.-Y Teng and E. A. Stern. "Plasma radiation from metal grating surfaces". *Phys. Rev. Lett.*, 19:511–514, 1967.

[63] M. V. Bashevoy, F. Jonsson, A. V. Krasavin, N. I. Zheludev, Y. Chen, and M. I. Stockman. "Generation of traveling surface plasmon waves by free-electron impact". *Nano Lett.*, 6(6):1113–1115, 2006.

[64] J. T. van Wijngaarden, E. Verhagen, A. Polman, C. E. Ross, H. J. Lezec, and H. A. Atwater. "Direct imaging of propagation and damping of near-resonance surface plasmon polaritons using cathodoluminescence spectroscopy". *Appl. Phys. Lett.*, 88:221111, 2006.

[65] N. Yamamoto, K. Araya, A. Toda, and H. Sugiyama. "Light emission from surfaces, thin films and particles induced by high-energy electron beam". *Surf. Interface Anal.*, 31(2):79 – 86, 2001.

[66] J. D. Jackson. *Classical Electrodynamics*. John Wiley & Sons, 1999.

[67] F. J. García de Abajo. "Optical excitations in electron microscopy". *Reviews of Modern Physics*, 82:209–275, 2010.

[68] M. Kuttge. *Cathodoluminescence plasmon microscopy*. PhD thesis, Utrecht University, 2009.

[69] V. L. Ginzburg and I. M. Frank. "Radiation of a uniformly moving electron due to its transition from one medium to another". *Zh. Eksp. Teor. Fiz*, 16:1528 [J. Phys (USSR), 9, 353 (1945)], 1946.

[70] P. Goldsmith and J. V. Jelley. "Optical transition radia- tion from protons entering metal surfaces". *Philos. Mag.*, 4:836–844, 1959.

[71] G. W. Ford and W. H. Weber. "Electromagnetic interactions of molecules with metal surfaces". *Phys. Rep.*, 113:195–287, 1984.

[72] P. A. Cherenkov. "The visible glow of pure liquids under the action of γ-rays". *Dokl. Akad. Nauk. SSSR*, 2:451–454, 1934.

[73] I. M. Frank and I. Tamm. "Coherent visible radiation of fast electrons passing through matter". *Dokl. Akad. Nauk. SSSR*, 14:109–114, 1937.

[74] I. Tamm. "Radiation emitted by uniformly moving electrons". *J. Phys. (Moscow)*, 1:439–454, 1939.

[75] S. J. Smith and E. M. Purcell. "Visible light from localized surface charges moving across a grating". *Phys. Rev.*, 92(4):1069, 1953.

[76] T. di Francia. "On the theory of some Cherenkovian effects". *Nuovo Cimento*, 16:61–77, 1960.

[77] P. M. van den Berg. "Smith-Purcell radiation from a point charge moving parallel to a reflection grating". *J. Opt. Soc. Am.*, 63:1588–1597, 1973.

[78] J. H. Brownell, J. Walsh, and G. Doucas. "Spontaneous Smith-Purcell radiation described through induced surface currents". *Phys. Rev. E*, 57:1075–1080, 1998.

[79] M. V. Bashevoy, F. Jonsson, K. F. MacDonald, Y. Chen, and N. I. Zheludev. "Hyperspectral imaging of plasmonic nanostructures with nanoscale resolution". *Opt. Exp.*, 15(18):11313–11320, 2007.

[80] A. Sánchez-Iglesias, I. Pastoriza-Santos, J. Pérez-Juste, B. Rodrigez-González, F. J. García de Abajo, and L. M. Liz-Marzán. "Synthesis and optical properties of gold nanodecahedra with size control". *Adv. Mater.*, 18:2529–2534, 2006.

[81] L. Rodrígez-Lorenzo, R. A. Alvarez-Puebla, I. Pastoriza-Santos, S. Mazzucco, O. Stéphan, M. Kociak, L. M. Liz-Marzán, and F. J. García de Abajo. "Zeptomol Detection Through Controlled Ultrasensitive Surface-Enhanced Raman Scattering". *J. Am. Chem. Soc.*, 131:4616–4618, 2009.

[82] R. A. Alvarez-Puebla, L. M. Liz-Marzán, and F. J. García de Abajo. "Light Concentration at the Nanometer Scale". *J. Phys. Chem. Lett.*, 1:2428–2434, 2010.

[83] J. Nelayah, M. Kociak, O. Stéphan, F. J. García de Abajo, M. Tencé, L. Henrard, D. Taverna, I. Pastoriza-Santos, L. M. Liz-Marzán, and C. Colliex. "Mapping surface plasmons on a single metallic nanoparticle". *Nat. Phys.*, 3(5):348 – 353, 2007.

[84] V. Myroshnychenko, E. Carbó-Argibay, I. Pastoriza-Santos, J. Pérez-Juste, L. M. Liz-Marzán, and F. J. García de Abajo. "Modeling the Optical Response of Highly Faceted Metal Nanoparticles with a Fully 3D Boundary Element Method". *Adv. Mater.*, 20:4288–4293, 2008.

[85] V. Myroshnychenko, J. Rodrigez-Fernández, I. Pastoriza-Santos, A. M. Funston, C. Novo, P. Mulvaney, L. M. Liz-Marzán, and F. J. García de Abajo. "Modellin the optical response of gold nanoparticles". *Chem. Soc. Rev.*, 37:1792–1805, 2008.

[86] F. J. García de Abajo and A. Howie. "Relativistic Electron Energy Loss and Electron-Induced Photon Emission in Inhomogeneous Dielectrics". *Phys. Rev. Lett.*, 80:5180–5183, 1998.

[87] F. J. García de Abajo and A. Howie. "Retarded field calculation of electron energy loss in inhomogeneous dielectrics". *Phys. Rev. B*, 65:115418, 2002.

[88] A. E. Siegman. *Lasers*. University Science Books, 1986.

[89] O. Svelto. *Principles of Lasers* 5th ed. Springer, 2010.

[90] K.L. Kelly, E. Coronado, L.L. Zhao, and G.C. Schatz. "The Optical Properties of Metal Nanoparticles: The Influence of Size, Shape, and Dielectric Environment". *Journal of Physical Chemistry B*, 107(3):668–677, 2003.

[91] J-J. Greffet. "Nanoantennas for Light Emission". *Science*, 308:1561–1563, 2005.

[92] M. L. Brongersma. "Engineering optical nanoantennas". *Nat. Photon.*, 2:270, 2008.

[93] J. Aizpurua, G. W. Bryant, L. J. Richter, F. J. García de Abajo, B. K. Kelley, and T. Mallouk. "Optical properties of coupled metallic nanorods for field-enhanced spectroscopy". *Phys. Rev. B*, 71:235420, 2005.

[94] O. L. Muskens, V. Giannini, J. A. Sánchez-Gil, and J. Gómez Rivas. "Optical scattering resonances of single and coupled dimer plasmonic nanoantennas". *Opt. Exp.*, 15(26):17736–17746, 2007.

[95] N. Yu, E. Cubukcu, L. Diehl, M. A. Belkin, K. B. Crozier, F. Capasso, D. Bour, S. Corzine, and G. Hòfler. "Plasmonic quantum cascade laser antenna". *Appl. Phys. Lett.*, 91:173113, 2007.

[96] G. Adamo, K. F. MacDonald, Y. H. Fu, C-M. Wang, D. P. Tsai, F. J. García de Abajo, and N. I. Zheludev. "Light well: A tunable free-electron light source on a chip". *Phys. Rev. Lett.*, 103:113901, 2009.

[97] M. Bosman, V. J. Keast, M. Watanabe, A. I. Maaroof, and M. B. Cortie. "Mapping surface plasmons at the nanometre scale with an electron beam". *Nanotech.*, 18:165505, 2007.

[98] N. Yamamoto, M. Nakano, and T. Suzuki. "Light emission by surface plasmons on nanostructures of metal surfaces induced by high-energy electron beams". *Surf. Interf. Anal.*, 38:1725–1730, 2006.

[99] R. Gómez-Medina, N. Yamamoto, M. Nakano, and F. J. García de Abajo. "Mapping plasmons in nanoantennas via cathodoluminescence". *New J. Phys.*, 10:105009, 2008.

[100] M. N'Gom, S. Li, G. Schatz, R. Emi, A. Agarwal, N. Kotov, and T. Norris. "Electron-beam mapping of plasmon resonances in electromagnetically interacting gold nanorods". *Phys. Rev. B*, 80:113411, 2009.

[101] M.-W. Chu, V. Myroshnychenko, C. H. Chen, J.-P. Deng, C.-Y. Mou, and F. J. García de Abajo. "Probing bright and dark surface-plasmon modes in individual and coupled noble metal nanoparticles using an electron beam". *Nano Lett.*, 9:399, 2009.

[102] B. Nikoobakht and M. A. El-Sayed. "Preparation and growth mechanism of gold nanorods (NRs) using seed-mediated growth method". *Chem. Mater.*, 15:1957, 2003.

[103] T. K. Sau and C. J. Murphy. "Seeded high yield synthesis of short au nanorods in aqueous solution". *Langmuir*, 20:6414, 2004.

[104] A. Dereux, C. Girard, and J.-C. Weeber. "Theoretical principles of near-field optical microscopies and spectroscopies". *J. Chem. Phys.*, 112(18):7775–7789, 2000.

[105] I. I. Smolyaninov, A. V. Zayats, A. Gungor, and C. C. Davis. "Single-photon tunneling via localized surface plasmons". *Phys. Rev. Lett.*, 88:187402, 2002.

[106] F. J. García de Abajo and M. Kociak. "Probing the photonic local density of states with electron energy loss spectroscopy". *Phys. Rev. Lett.*, 100:106804, 2008.

[107] M. Kuttge, E. J. R. Vesseur, A. F. Koenderink, H. J. Lezec, H. A. Atwater, F. J. García de Abajo, and A. Polman. "Local density of states, spectrum, and far-field interference of surface plasmon polaritons probed by cathodoluminescence". *Phys. Rev. B*, 79:113405, 2009.

[108] U. Hohenester, H. Ditlbacher, and J. R. Krenn. "Electron-energy-loss spectra of plasmonic nanoparticles". *Phys. Rev. Lett.*, 103:106801, 2009.

[109] "http://nano.gov".

[110] N. I. Zheludev, S. L. Prosvirnin, N. Papasimakis, and V. A. Fedotov. "Lasing spaser". *Nat. Photon.*, 2:351–354, 2008.

[111] H.-G. Park, C. J. Barrelet, Y. Wu, B. Tian, F. Qian, and C. M. Lieber. "A wavelength-selective photonic-crystal waveguide coupled to a nanowire light source". *Nat. Photon.*, 2:622–626, 2008.

[112] M. Nakamoto. "Current trends in field emission displays". In *IEEE Industry Applications Society Annual Meeting*, pages 447–451, Edmonton, Alberta, Canada, 2008. IEEE.

[113] A. I. Denisyuk, K. F. MacDonald, F. J. García de Abajo, and N. I. Zheludev. "Towards femtojoule nanoparticle phase-change memory". *Jpn. J. Appl. Phys.*, 48:03A065, 2009.

[114] H. P. O'Shea, P. G. andFreund. "Free-Electron Lasers: Status and Applications". *Science*, 292:1853–1858, 2001.

[115] H. Koyama. "Cathodoluminescence study of SiO2". *J. Appl. Phys.*, 51(4):2228–2235, 1980.

[116] A. Mooradian. "Photoluminescence of metals". *Phys. Rev. Lett.*, 22(5):185–187, 1969.

[117] F. J. García de Abajo. "Colloquium: Light scattering by particle and hole arrays". *Reviews of Modern Physics*, 79:1267–1290, 2007.

[118] J. Urata, M. Goldstein, M. F. Kimmitt, A. Naumov, C. Platt, and J. E. Walsh. "Superradiant Smith-Purcell emission". *Phys. Rev. Lett.*, 80(3):516, 1998.

[119] Y. Neo, H. Shimawaki, T. Matsumoto, and H. Mimura. "Smith-Purcell Radiation from Ultraviolet to Infrared Using a Si-field Emitter". In *Eighth IEEE International Vacuum Electronics Conference*, pages 351–352, Kitakyushu, Japan, 2007. IEEE.

[120] M. J. Moran. "X-ray generation by the Smith-Purcell effect". *Physical Review Letters*, 69(17):2523–2526, 1992.

[121] E. J. Reed, M. Soljačić, R. Gee, and J. D. Joannopoulos. "Coherent optical photons from shockwaves in crystals". *Physical Review Letters*, 96:013904, 2006.

[122] A. Gover. "Superradiant and stimulated-superradiant emission in prebunched electron-beam radiators. I. Formulation". *Phys. Rev. ST Accel. Beams*, 8:030701, 2005.

[123] H. L. Andrews and C. A. Brau. "Gain of a Smith-Purcell free-electron laser". *Phys. Rev. ST Accel. Beams*, 7:070701, 2004.

[124] A. Bakhtyari, J. E. Walsh, and J. H. Brownell. "Amplified-spontaneous-emission power oscillation in a beam-wave interaction". *Phys. Rev. E*, 65:066503, 2002.

[125] R. J. Walters, R. V. A. van Loon, I. Brunets, J. Schmitz, and A. Polman. "A silicon-based electrical source of surface plasmon polaritons". *Nat. Mater.*, 9:21–25, 2010.

[126] G Adamo, K F MacDonald, Y H Fu, D P Tsai, F J García de Abajo, and N I Zheludev. "Tuneable electron-beam-driven nanoscale light source". *Journal of Optics*, 12:024012, 2010.

[127] T. S. Kao, S. D. Jenkins, J. Ruostekoski, and N. I. Zheludev. "Coherent Control of Nanoscale Light Localization in Metamaterial: Creating and Positioning Isolated Subwavelength Energy Hot Spots". *Phys. Rev. Lett.*, 106:085501, 2011.

[128] S. D. Jenkins and J. Ruostekoski. "Collective electromagnetic response of discrete metamaterial systems". *arXiv*, :1012.3928, 2010.